Title

Remote Sensing of Evapotranspiration in California Cropland: Improvement and Hydrological Applications

Author

Wong, Andy

Publication Date

2021

Peer reviewed|Thesis/dissertation

Remote Sensing of Evapotranspiration in California Cropland:
Improvement and Hydrological Applications

By

ANDY, JIA YING, WONG
DISSERTATION

Submitted in partial satisfaction of the requirements for the degree of

DOCTOR OF PHILOSOPHY

in

Hydrologic Science

in the

OFFICE OF GRADUATE STUDIES

of the

UNIVERSITY OF CALIFORNIA

DAVIS

Approved:

_____

Yufang Jin, Chair

_____

Kyaw Tha Paw U

_____

Graham E. Fogg

Committee in Charge

2021

Table of Contents

Abstract

Due to population growth and progress made in sustainable water management, water resources availability to California's croplands is becoming more scarce. Besides, due to climate change, year-to-year water supplies are becoming increasingly unpredictable. As 80% of all human use of water is diverted for farmland irrigation, spatial estimates of crop evapotranspiration with high accuracy, from the field to watershed scale, have become increasingly important for water resources management. The present work aims to improve and evaluate an algorithm for estimating spatial crop evapotranspiration and explore its application to water resource management. The generated knowledge and tools from this study can provide data-driven guidance for water resources planning at the watershed level, contributing to a more sustainable use of water in California's agricultural regions.

The first chapter focused on improving and evaluating a semi-empirical model to map crop evapotranspiration at a 30m resolution using Landsat satellite images and concurrent spatial meteorological data. The algorithm was optimized and cross-validated with available field measurements from over 22 sites in California's Central Valley for major crops, including alfalfa, almond, citrus, corn, pasture, and rice. The evapotranspiration estimates explained more than 70% variance in daily measurements with an RMSE of 0.88 mm day^{-1}. The site-level evaluation was repeated with the estimates from another remote sensing algorithm, PT-JPL, which is developed by scientists at the NASA Jet Propulsion Laboratory. The two algorithms share a similar theoretical basis and design, and an improvement over a PT-JPL was observed when the proposed approach is crop-specifically calibrated. This chapter demonstrated that land use information and field measurements are useful for reducing the uncertainty of spatial crop evapotranspiration estimates. The model presented in the first chapter can be applied for

continuous monitoring of the dynamics and spatial heterogeneity of crop consumptive water use in California at a field scale.

Chapter 2 scaled up the proposed algorithm to estimate annual evapotranspiration at 30m resolution across the entire Central Valley for water years 2014 and 2016. It examined the spatial pattern of crop water consumptive use at a regional level and a local scale of Groundwater Sustainability Agencies (GSAs). We estimated a mean ($\bar{x}$) evapotranspiration of 820 mm yr^{-1} with a standard deviation (σ) of 290 mm yr^{-1}in 2014. Compared to 2014, the total estimated evapotranspiration in 2016 increased by 9.6%, mostly because of land-use conversion from fallow/idle land to cropland. Large variation of agricultural water use was found across different and within the same crop types, with a coefficient of variation ranging from 8% for Rice ($\bar{x}$ = 1110, σ = 85 mm yr^{-1}) to 59% for Pistachio ($\bar{x}$ = 592, σ = 352 mm yr^{-1}). Besides, tree crops, such as Almonds, were found to have a large variation of evapotranspiration among and within GSAs. To further understand the spatial variability of almond's evapotranspiration at the GSAs scale, an empirical model using normalized difference vegetation index (NDVI) and orchard age was optimized and evaluated. Orchard age was shown to be an important factor contributing to the variability of evapotranspiration across GSAs. However, spatial variation of other physical factors that could affect NDVI, such as salinity at the root zone, will likely have stronger control over almond's evapotranspiration, explaining its spatial variation within and among GSAs. Overall, this chapter demonstrates how spatial estimates of evapotranspiration can be used to provide data-driven guidance for more effective land use and water planning across regional and local GSA scales.

In chapter 3, the proposed algorithm was implemented to estimate daily crop evapotranspiration at 30m resolution in the Pajaro Valley, CA for 2009 and 2011. The objective of the study was to

develop and evaluate methods to estimate agricultural applied water from field to local agency scales. To estimate applied water at the field scale, the daily spatial evapotranspiration was coupled with soil water balance for simulation of daily fluxes in a water balance at 30m resolution. This coupled model requires a crop-specific optimization on application efficiency, using a limited number of field-scale applied water records. When the model estimates are spatially aggregated by fields and temporally aggregated to the annual total, the evaluation showed that our applied water estimates agreed well with the pumping records at the field scale, explaining 86% of variability with an RMSE of 39.6 million liters. When aggregated over the Pajaro Valley, we estimated a total of agricultural groundwater pumping ranging from 53.9 in 2009 to 42.6 billion liters in 2011, which deviated from the sum of all agricultural pumping and surface water delivery by less than 4.6%. Over 16 subregions in the valley, our estimates explained more than 89% variance in pumping records with an RMSE of 1.2 billion liters. Our estimates of water balance fluxes were also compared with that by USGS, to evaluate the model's ability in representing the hydrological process of the Valley. Results from chapter 3 demonstrated that remote sensing evapotranspiration estimates can be used to estimate regional agricultural applied water with reasonable accuracy yet in a cost-efficient way, over areas where only a limited number of field-scale applied water data is available for calibrating a soil water balance model.

Acknowledgments

Throughout my Ph.D. study, I considered giving up multiple times. I was frustrated that the research community undervalues the semi-empirical approach of modeling evapotranspiration, that a third of my work does not fit into the three dissertation chapters, and that the relevance between my work and my desired career is under an exponential decay due to rapid advances in large scale data processing, deep neural networks, and computer visions. I would not be able to complete my study without the support and encouragement of my mentors, family, and friends.

I would like to thank my advisor, Yufang Jin, for giving me support and freedom in exploring technology, approaches, and applications of remote sensing. She fostered my creativity by giving me opportunities to build and use drones back in the days when 3DR was mainstream, paying for conferences and workshops, and providing feedback on my ideas. Despite her busy schedule, she always makes herself available to me, thoroughly editing my writings and sharing suggestions on improving the research. I also want to thank my dissertation committee members, Kyaw Tha Paw U and Graham Fogg, for their mentorship and encouragement. Professor Paw U taught me the theoretical basis of evapotranspiration. He shared many of his research ideas with me, encouraging me to investigate and improve the theoretical foundations of the semi-empirical approach of estimating evapotranspiration. Professor Fogg has been supportive of my research ever since I first shared my research idea with him. Without his guidance and encouragement, I might not dare to try using and evaluating groundwater models with remote sensing evapotranspiration. Thank you to the other UC faculty who have helped and encouraged me throughout my journey, especially Samuel Sandoval Solis, Thomas Harter, and Josue Medellin-Azuara.

Thank you to the colleagues at the University of California, especially to Sean Hogan, Scott Devine, Alex Mandel, Stephen Maples, Rongkui Han, Ruyan He, Jenae Clay, Bin Chen, Zhehan Tang, and Yuhan Huang, for all their help and suggestions. I am also grateful for the companionship of my labmates, including Ana Wegman, Sara Winsemius, and Erica Scaduto. And, thank you Shila Ruiz for answering all my administrative-related questions and making sure I am on track toward graduation.

To Mo and Erica, I am fortunate to have met you; May our friendship last a lifetime and our kids will be best friends forever. To my parents, Peter and Jade, and my sister, Amy, thank you for all your love, care, and sacrifices; I am forever in your debt. My family, Leo, and Adaline thank you for your presence in my life. And finally, thank you to my wife, Grace, for your unconditional love and support. You bring out the best in me, and I cannot wait to start the next chapter of our lives together.

The dissertation presented here is primarily prepared by Andy, including idea origination, method design, programming, data analysis, and writing. Professor Yufang Jin contributed significantly to improving the methods and polishing the writings. Professor Kyaw Tha Paw U, Graham Fogg, and other co-authors, as listed under each chapter, also provided feedbacks and suggestions on methods and writings. The research in Chapters 1 and 3 would not be possible without the data provided by the coauthors and the hard work by the members of the field crews.

Chapter 1: An Optimized Crop Evapotranspiration Estimation using Landsat Satellite and Spatial Meteorological Observations

Andy. J.Y. Wong[1], Y. Jin[1], J. Medellín-Azuara[2], K. T. Paw U[1], E. R. Kent[1], J. M. Clay[1], F. Gao[3], J. B. Fisher[4], G. Rivera[4], C. M. Lee[4], K. S. Hemes[5], E. Eichelmann[6], D. D. Baldocchi[7], S. J. Hook[4]

[1] Department of Land, Air and Water Resources, University of California, Davis, CA, USA.

[2] Department of Civil and Environmental Engineering, University of California, Merced, CA, USA.

[3] USDA, Agricultural Research Service, Hydrology and Remote Sensing Laboratory, Beltsville, MD, USA.

[4] Jet Propulsion Laboratory, California Institute of Technology, Pasadena, CA, USA.

[5] Stanford Woods Institute for the Environment, Stanford University, Stanford, CA, USA.

[6] School of Biology and Environmental Science, University College Dublin, Ireland.

[7] Dept. of Environmental Sciences, Policy, & Management, University of California, Berkeley, CA, USA.

This chapter is under review by the Journal of Water Resources Research. The manuscript, titled *Multi-scale Assessment of Agricultural Consumptive Water Use in California's Central Valley*, is prepared by the same co-authors as listed in this chapter.

Abstract

A cost-effective and timely method to estimate crop evapotranspiration with known uncertainty from the field to watershed scale has become increasingly important for water management, particularly for irrigated agriculture in semi-arid regions. To enable growers to tailor irrigation management based on in-field and within-season variation of water use and to better inform regional water managers on crop consumptive use, we improved a semi-empirical Priestley-Taylor evapotranspiration approach, specifically for croplands, to estimate daily evapotranspiration with 30m Landsat satellite data. The approach was optimized and cross-validated with available field measurements from over 22 sites for major crops, including alfalfa, almond, citrus, corn, pasture, and rice. The evapotranspiration estimates explained more than 70% variance in daily measurements with an RMSE of 0.88 mm day^{-1}. An improvement over a prominent Priestley-Taylor-based remote sensing model is achieved through crop-specific calibration. The model presented here can be applied for continuous monitoring of the dynamics and spatial heterogeneity of crop consumptive water use in California at a field scale. It is expected to improve irrigation practices at the farm level and provide data-driven guidance for water planning at the watershed level, contributing to more sustainable water use in California's agricultural regions.

1. Introduction

Evapotranspiration, also known as crop consumptive water use in agricultural lands, is often the largest yet most uncertain component of the agricultural water balance in semi-arid regions (Burt et al., 2002; Fisher et al., 2017; Oki et al., 2006). Field-based evapotranspiration measurements, e.g., from eddy covariance sensors, are reliable and accurate if set up and

processed carefully (Chávez et al., 2009). It requires expensive and calibrated instruments, in addition to care in field set-up and complex data post-processing data methodology for quality assurance. The measurement footprint is generally limited to less than a few hundred meters, so an excessive number of stations would be required for regional-scale evapotranspiration measurements. In contrast, modeling evapotranspiration with publicly accessible satellite data offers a potentially cost-effective monitoring alternative, due to its large spatial coverage and consistent imagery acquisition. However, remote sensing estimates have many limitations, including the frequency of overpasses, vast amounts of data processing, and the necessity for clear skies and scientifically defensible and accurate models.

A few algorithms of varying complexity have been developed to map crop evapotranspiration using remote sensing data, due to the large spatial coverage and consistent imagery acquisition by satellite instruments (Akbar et al., 2019; Allen et al., 2007; Anderson et al., 2012; Bastiaanssen et al., 1998; Ganguly et al., 2012; Nagler et al., 2005; John M. Norman & Becker, 1995). For example, the crop coefficient-based evapotranspiration approach has been used by California's growers for irrigation management (California Department of Water Resources, 2005; Melton et al., 2012). This method is relatively easy to implement but does not account for other factors, such as water stress and thus likely overestimates actual evapotranspiration (Anderson et al., 2012; Cuenca et al., 2013). Energy balance-based approaches, on the other hand, estimate evapotranspiration as a residual between available energy and sensible heat flux (Allen et al., 2007; Bastiaanssen et al., 1998; John M. Norman & Becker, 1995; Su, 2002), e.g., as adopted by the Surface Energy Balance Algorithm for Land (SEBAL) (Bastiaanssen et al., 1998) and Mapping EvapoTranspiration at high Resolution with Internalized Calibration (METRIC) (Allen et al., 2007). In METRIC, the sensible heat is often

estimated using clusters of hot and cold pixels observed within each Landsat scene (Allen et al., 2007). The pixel selection can be fully automated (Allen et al., 2013) for large-scale applications or manually selected by professional users for more accurate regional estimates.

More sophisticated methods involve solving the soil and canopy latent heat components within a process model, constrained by satellite data (Anderson et al., 1997, 2018; Ryu et al., 2011). The Atmosphere-Land EXchange Inverse (ALEXI) model, for example, implements the Two-Source Energy Balance in a time differential mode, based on two snapshots of high temporal frequency geostationary satellite thermal observations, to reduce the sensitivity to the errors in absolute land surface temperatures (Anderson et al., 1997, 2004, 2018). DisALEXI has been further developed to estimate evapotranspiration at 30 m resolution, by bringing in additional higher spatial resolution thermal data from Landsat (Anderson et al., 2004, 2012, 2018; J. M. Norman et al., 2003). A recent comparative study of crop evapotranspiration estimates over the Sacramento San Joaquin Delta showed that DisALEXI estimates had an RMSE of 1.43 mm day^{-1} and mean bias of 0.13 mm day^{-1} while the calibrated METRIC prepared by the Irrigation Training & Research Center had an RMSE and mean bias of 2.55 and 2.06 mm day^{-1}, respectively (Medellín-Azuara, J. et al., 2018). Another biophysical model, Breathing Earth System Simulator (BESS) (Baldocchi et al., 2019; Jiang & Ryu, 2016, p. 201; Ryu et al., 2011), couples surface energy balance, photosynthesis, and stomatal conductance processes to estimate evapotranspiration, forced by biophysical parameters from MODIS 8-day 1km observations.

One compromise between the simple crop-coefficient-based approaches and more complex energy balance models described above is the Priestley Taylor approach. It is an alternative to Penman-Monteith for estimating potential evapotranspiration (Debruin H. A. R.,

1983; Eichinger et al., 1996; Priestley & Taylor, 1972). It is primarily driven by available energy and a Priestley Taylor coefficient that partitions available energy to latent and sensible heat. This coefficient was found to be constant for estimating potential evapotranspiration. For actual evapotranspiration, biophysical controls such as water stress can downregulate it and thus reduce the fraction of available energy used for latent heat. Fisher et al., (2008), for example, parameterized the Priestley Taylor coefficient separately for soil evaporation, canopy transpiration, and interception using remotely sensed vegetation index and meteorological data. It has been applied to estimate monthly evapotranspiration globally at 5 km and 1° resolution using Advanced Very High Resolution Radiometer data (Fisher et al., 2008; Vinukollu et al., 2011), regionally at 1km using Moderate Resolution Imaging Spectroradiometer (MODIS) data (Yao et al., 2015) and most recently at 70 m using ECOsystem Spaceborne Thermal Radiometer Experiment on Space Station data (Fisher et al., 2020). Jin et al., (2011) optimized Priestley Taylor coefficient, α, as a function of Leaf Area Index (LAI) and soil moisture for each plant function type, using the eddy covariance tower measurements from AmeriFlux sites, and estimated monthly evapotranspiration at 1km for the entire continental US, from primarily MODIS data.

Our study here builds upon the original semi-empirical Priestley Taylor model (Jin et al., 2011). We first modified the 1km, monthly ecological evapotranspiration model to estimate 30m, daily crop evapotranspiration in the Sacramento San Joaquin Delta (Medellín-Azuara, J. et al., 2018). Here, we further calibrated and evaluated the refined semi-empirical Priestley Taylor method (Jin et al., 2011) over major California crops, using the Landsat Analysis Ready Data (Dwyer et al., 2018). To better understand the uncertainties and limitations of our evapotranspiration estimates in the context for water use study within California, multiple cross-

validations were conducted. We expected this improved remote sensing evapotranspiration model, tailored for estimating crop water consumptive use over irrigated land in semi-arid regions, could provide valuable information for field-scale and regional water resources management.

2. Data and Methods

We adapted the semi-empirical Priestley Taylor method (Jin et al., 2011), as shown in Equation (1), for agricultural sites in California. The method is driven by Landsat remote sensing data and was calibrated and evaluated using recently available in-situ evapotranspiration measurements, from 2003 to 2019, over a variety of irrigated crop types.

$$LE = PT_a * \frac{\Delta}{\Delta+\gamma} * (R_n - G) \quad (1)$$

Δ represents the slope of the vapor pressure-temperature curve and γ psychrometric constant. Net radiation (Rn) and ground heat flux (G) was estimated from Landsat observations. $PT_{a,}$ hereafter referred to as the actual Priestley Taylor coefficient, approximates the fraction of available energy used for actual evapotranspiration. For potential evapotranspiration without any water limitation, the potential Priestley Taylor coefficient was found to be a constant near 1.26 (Paw U & Gao, 1988). For actual evapotranspiration, we here estimated PT_a as a function of plant growth and water stress, as shown in section 2.4.

2.1 Study Area

Our study area is the evapotranspiration measurement sites over the 26 agricultural fields across the major agricultural production area in the Central Valley of California (Figure 1). Most of the sites were located in the Sacramento San Joaquin Delta, as part of the Delta comparative

study supported by the California State Water Resources Control Board Office of the Delta Watermaster and other agencies. The Sacramento San Joaquin Delta is the major hub of California's statewide water supply system, where the two largest and most important basins in the state join and provide some portion of water supply to more than 27 million people and approximately twelve-thousands square kilometers of irrigated farmland (Delta Stewardship Council, 2018), including more than 1400 km^2 of agricultural land within the Delta.

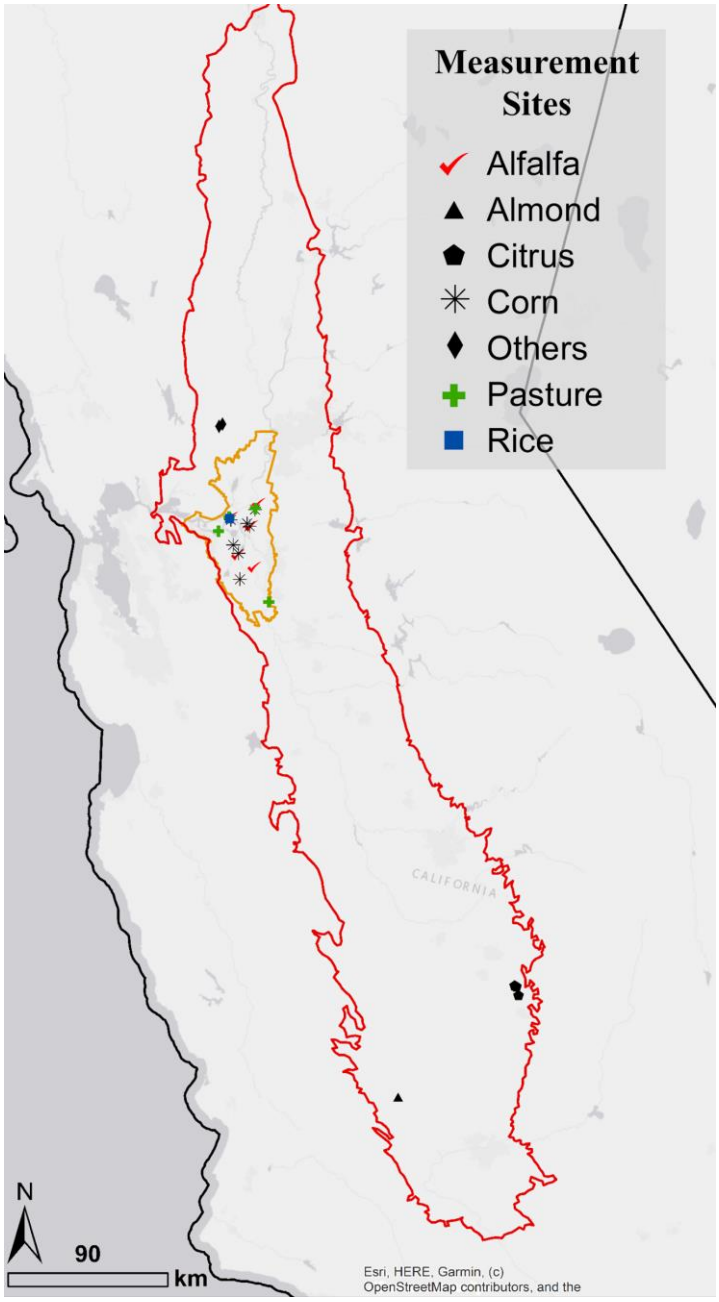

Figure 1. Locations of measurement sites overlaid with boundaries of regions of interest: California (black line), Central Valley (red line), and the Legal Sacramento San Joaquin Delta (orange lines).

2.2 Input Data

2.2.1 Field measurements

A total of 26 evapotranspiration measurement sites were available in the Central Valley, including five agricultural sites from the AmeriFlux network and two from cropland sites established for the shorter-term study of California's specialty crops (Table 1). The measurement sites represented 8 crop types, namely, alfalfa, almond, citrus, corn, pasture, rice, tomato, and beardless winter wheat (Table 1). Evapotranspiration was measured either with an eddy covariance system (Baldocchi et al., 1988; Paw U et al., 2000; Swinbank, 1951) or with a surface renewal system (Paw U et al., 1995). The eddy covariance system uses a sonic anemometer and infrared gas analyzer to measure three-dimensional wind velocities and high-frequency fluctuations of water vapor concentrations (Baldocchi et al., 2001). It measures evapotranspiration by monitoring the vertical flux of water vapor. High-frequency eddy covariance measurements in 2 alfalfa, 2 corn, and one rice AmeriFlux sites were collected and preprocessed into half-hourly evapotranspiration data as outlined in Eichelmann et al., (2018); Hemes et al., (2019). Of the five AmeriFlux sites, net radiation for alfalfa and corn was measured with four-channel net radiometers.

Most sites located in the Sacramento San Joaquin Delta region were also employed in the Delta Consumptive Use Comparative Study (Medellín-Azuara, J. et al., 2018) supported by the California State Water Resources Control Board Office of the Delta Watermaster and other agencies. Less expensive surface renewal systems were deployed over 14 sites for corn, alfalfa, and pasture. They use thermocouples to measure sensible heat flux, an NRLITE2 Net Radiometer for net radiation, and either measure ground heat flux (G) with a combination of

ground heat flux plates and soil thermocouples or assume it is zero for daily estimates. Evapotranspiration is then estimated as the residual of the energy balance. For each crop type, an eddy covariance tower was deployed to calibrate the sensible heat flux relationship between eddy covariance and surface renewal measurements (Castellví et al., 2006; Shapland et al., 2012).

Evapotranspiration measurements were compiled from two specialty crop research projects in Tulare and Kern county of the southern Central Valley, including surface renewal measurements in citrus orchards from 2001 to 2004 (Consoli et al., 2006; Snyder & O'Connell, 2007) and eddy covariance measurements in an almond orchard from 2009 to 2012 (Falk et al., 2013, p. 20; He et al., 2017). We used only data collected after February 2003 in this study, considering the data availability of California Irrigation Management Information System Spatial product (Spatial-CIMIS) data. The most recently available eddy covariance tower measurements by NASA JPL were also added. The JPL sites are located at the Russell Ranch research field, near Davis, including one over tomato from February to October 2017, and the other over winter wheat from December 2016 to October 2017. These towers have advanced thermal infrared radiometers to measure land surface temperature, and two sets of four channels net radiometers to reduce measurement uncertainty. High-frequency evapotranspiration data were automatically processed using Campbell Scientific Inc.'s standard Eddy-Covariance Datalogger Program software and various quality control procedures. All half-hourly measurements were preprocessed and aggregated into daily evapotranspiration if less than 20% of the half-hourly measurements were missing within a day.

Table 1. List of in situ measurement stations and evapotranspiration data availability.

Crop type (site days)	ID	Site	Time Period	Citation
Alfalfa (3870)	1*	US-Tw3: Twitchell Island	May 2013 – Dec. 2015	Eichelmann et al., 2018; Hemes et al., 2018
	2*I	US-Bi1: Bouldin Island	Aug. 2016 – Sep. 2019	
	3‡	D02: Staten Island	Mar 2016 – Apr. 2017	Medellín-Azuara, J. et al., 2018
	4‡	D07: Bouldin Island	Jul. – Nov. 2016	
	5‡	D10: Bacon Island	Jul 2016 – Arp. 2017	
	6†	D13: Roberts Island	Jul. 2016 – May 2017	
	7‡	D14: Twitchell Island	Aug 2016 – Dec. 2016	
Almond (1405)	8*	A1: Lost Hill	Jan. 2009 – Dec. 2011	Couvreur et al., 2016
Citrus (486)	9†	E1: 2 years old	Jul. – Aug. 2004	Consoli et al., 2006
	10†	E2: 4 years old		
	11†	E3: 15 years old		
	12†	E4: 34+ years old	Feb. 2003 – Aug. 2004	
Corn (1657)	13*	US-Tw2: Twitchell Island	May 2012 – May 2013	Hemes et al., 2018
	14*I	US-Bi2: Bouldin Island	April 2017 – May 2018	
	15‡	D01: Union Island	April 2016 – Sep. 2016	Medellín-Azuara, J. et al., 2018
	16‡	D06: Holland Island	Jul. – Oct. 2016	
	17‡	D08: Bouldin Island	Jul. – Sep. 2016	
	18‡	D09: Bacon Island	Jul. – Oct. 2016	
	19†	D11: Staten Island	Apr. – Sep. 2016	
Pasture (697)	20‡	D03: Staten Island	May 2016 – May 2017	Medellín-Azuara, J. et al., 2018
	21‡	D04: Jersey Island	Jun. – Nov. 2016	
	22‡	D05: Ripon Island	Jun. 2016 – Jan. 2017	
	23†	D12: Twitchell Island	Jun. 2016 – Dec. 2016	
Rice (2909)	24*	US-Twt: Twitchell Island	Apr. 2009 – Apr. 2017	Baldocchi et al., 2016
Tomato (112)	25*I	RR2: Russell Ranch	Jan. 2017 – Nov. 2017	Cawse-Nicholson et al., 2017
Winter wheat (102)	26*I	RR1: Russell Ranch	Jan. 2017 – Oct. 2017	

*Eddy covariance. †Full surface renewal system. ‡Lite surface renewal system estimates daily evapotranspiration by assuming the daily mean G is zero. [I] Reserved for independent validation.

2.2.2 Meteorological data

We obtained the daily gridded meteorological data, including minimum and maximum air temperature at 1.5 m, and daily dew point, from Spatial-CIMIS at a 2 km resolution (Hart et al., 2009). The California Department of Water Resources (DWR) manages a network of over 145 automated weather stations over well-maintained and well-watered grass sites across California providing reference evapotranspiration for pasture. The station data were spatially interpolated to produce the 2-km gridded dataset since 2003. We also used the Spatial-CIMIS cloud cover and incoming solar radiation for both clear-sky and all-sky conditions, derived from Geostationary Operational Environmental Satellite visible channel imager data, for our radiation component calculation.

2.2.3 Remote Sensing data

All available surface reflectance and surface temperature products, and the corresponding quality assessment layers at 30 m were downloaded from USGS Landsat Analysis Ready Dataset (Dwyer et al., 2018). The land surface temperature retrieval from the Landsat thermal data is based on a radiative transfer model with an improved surface emissivity estimate (Cook, 2014). Each Landsat took snapshots between 9:53 to 10:55 am Pacific Standard Time every 16 days. Invalid or high uncertainty pixel values were filtered based on the quality assessment rasters, including SLC gaps (U.S. Geological Survey, 2016), snow, cloud/cloud shadow, e.g., a high value for cloud or cirrus confidence, or with a surface temperature uncertainty greater or equal to 6 Kelvin. For model calibration and validation purposes, a single-pixel near each measurement site was extracted.

2.3 Estimating daily net radiation and ground heat flux from Landsat observations

We estimated surface net radiation (R_n) at a daily time scale as shown in Equation 2,

$$R_n = (1 - Albedo) * S_{\downarrow} + [\varepsilon_s \varepsilon \sigma T_a^4 - (m * (\varepsilon_s \sigma T_s^4) + b)] \quad (2)$$

, where $S_{\downarrow}$ and T_a are daily mean all-sky incoming solar radiation and daily mean air temperature (T_a), from CIMIS-spatial (Hart et al., 2009), ε represents all-sky emissivity for the atmosphere, ε_s surface emissivity, Ts for instantaneous land surface temperature in Kelvin from Landsat surface temperature product (Figure 2). Two parameters (m and b) to be optimized were included here to convert the estimated instantaneous outgoing longwave radiation to daily mean values. Shortwave surface albedo was derived at 30m from the Landsat surface reflectance using the narrowband to broadband conversion coefficients (Liang, 2001).

To calculate the incoming longwave radiation, we first estimated clear sky emissivity (ε_{clr}) using dew point temperature (T_{dew}) from Spatial-CIMIS, by following the approach of Jin et al., (2011) with the following equations, where $\varepsilon_{clr} = (1 - (1 + \xi)\exp\{-(1.2 + 3 * \xi)^{0.5}\})$, $\xi = 46.5(\frac{10 * e_a}{T_a + 273.15})$, and actual vapor pressure $e_a = 0.6108. * e^{\frac{17.27 * T_{dew}}{T_{dew} + 237.3}}$. To correct clear-sky emissivity to all-sky emissivity, we used the emipircally calibrated fuction of cloud fraction (F) and clear sky emissivity (ε_{clr}), where all-sky emissivity is $\varepsilon = (1 + \mu * F^{v}) * \varepsilon_{clr}$. The parameters were $\mu = 0.242$ and $V = 0.583$ (Duarte et al., 2006), and cloud fraction is computed by subtracting 1 by the ratio of Spatial-CIMIS's all-sky and clear-sky incoming solar radiation.

We developed a different approach from Jin et al., (2011) to estimate the daily mean outgoing longwave radiation from the land surface, considering there is only one Landsat overpassing time around 10:30 am as compared to four from MODIS Terra and Aqua. The

instantaneous outgoing longwave radiation was first estimated with Landsat land surface temperature and surface emissivity (ε_s) product (Cook, 2014), and then transformed to daily mean values through a linear relationship, as shown by two parameters (m and b) in Equation 2. We optimized this linear function, with the field measurements of half-hourly longwave radiation, only available from sites 1 and 13 from the training dataset during clear-sky overpassing days. A piecewise linear regression was used from the Shape Language Modeling toolbox (D'Errico, 2020), based on the site measurements of half-hourly longwave radiation, available from sites 1 and 13 from the training dataset during clear-sky overpassing days (Appendix I, Figure S1, Table S6).

Ground heat flux (G) was estimated from an empirical relationship of R_n and fractions of vegetation and soil ($f_{veg},\ f_{soil}$) as described in Jin et al., (2011), where $f_{soil} = e^{-0.4LAI}$, $f_{veg} = 1 - f_{soil}$, and $G = -4.6144 + \left(0.0496 f_{veg} + 0.1048 f_{soil}\right) R_n$. We adopted Fisher et al., (2008)'s approach in estimating LAI using normalized difference vegetation index (NDVI), where $LAI = -log\left(1 - (NDVI - 0.05)\right)/0.3$ (Fisher et al., 2008). NDVI, calculated based on the Landsat reflectance at red and near-infrared, has been widely used as an indicator of green vegetation cover and biomass (Tucker, 1979).

2.4 Actual Priestley Taylor coefficient optimization

The actual Priestley Taylor coefficient PT_a in Equation (1) was parameterized as an empirical function of LAI, moisture condition, and air temperature, as shown in Eq. 3,

$$PT_a = (A - C * e^{-B*LAI}) * (D * (NDMI + 1) + E) * f(T_a) \quad (3)$$

where A, B, C, D, E are parameters to be optimized, and f(T_a) was a relatively weak temperature control, due to the warm weather in the valley, i.e., lowered to 0.05 only if Ta is lower than -5 C, otherwise having the value of 1 (Jin et al., 2011). The soil moisture constraint was replaced with a remote sensing-based normalized difference moisture index (NDMI) (Gao, 1996; Ji et al., 2011), due to the lack of volumetric soil moisture data and the practical consideration in implementing a water balance model as used in Jin et al., (2011) study. NDMI is calculated from Landsat reflectance at two bands, the near-infrared centered at 0.86um and the shortwave infrared band centered at 1.61um. It has been used as an indicator of plant water conditions due to strong absorption by liquid water in the shortwave infrared region (Gao, 1996; Ji et al., 2011),.

The five parameters (A, B, C, D, E) in Eq. 3 were optimized with daily data from field observations. For each crop type that had field measurements, we used the nonlinear least-squares optimization procedure in MatLab Optimization Toolbox (MATLAB, 2018), to minimize the difference between the predicted actual Priestley Taylor coefficients and those derived from the daily means of field measurements. We randomly split the measurement data during all days when Landsat overpassing days were not obscured by cloud, into training (70%) and testing subsets (30%) for each site. The calibration was optimized for each crop type with the training subset data compiled from different fields of the same crop type. In this calibration procedure, data from sites 2, 14, 25, 26 were exclusively used for testing. To test the robustness of the algorithm, we repeated this random selection procedure 1000 times. For crop types that had seven stations, i.e., alfalfa and corn, modified k-fold cross-validation was further performed, with a “leave-two-out” approach, where all data from two stations was reserved for independent testing at a time, while the rest used for calibration.

To estimate evapotranspiration for crop types where field measurements were not available, a generalized optimization was also developed by pooling the data from all crops together for one universal set of optimization. This was done by randomly selecting a maximum of 50 points for each crop from the training dataset mentioned above, due to the unevenly available sample size among crop types. Similar to the crop-specific optimization, we also conducted two types of cross-validations to test the robustness of the generalized method.

2.5 Daily evapotranspiration estimation

During cloud-free days with Landsat overpassing, Landsat-derived LAI and NDMI were fed into Eq. 3 to estimate the actual Priestley Taylor coefficient for each pixel, which was then combined with available energy (Rn -G) to estimate daily evapotranspiration (Figure 2). For days between Landsat overpassing days or days (or pixels) without valid or high-quality values such as cloudy days or over scan-line corrector data gaps (Storey et al., 2005), a temporal interpolation approach was adopted (Allen et al., 2007; He et al., 2017). First, daily evapotranspiration estimates, during the adjacent clear sky Landsat days and within ± 2 months search window, were divided by the concurrent Spatial-CIMIS daily reference evapotranspiration to derive the fraction of reference evapotranspiration (EToF). A shape-preserving piecewise cubic interpolation was then applied to this discrete time series of EToF to obtain a continuous time series of daily EToF. We set a requirement of a minimum of 2 valid observations within the search window for a robust interpolation. This temporal interpolation was needed mostly during the rainy season in winter and early spring in California, an off-season for the majority of the crops. Finally, daily evapotranspiration for missing days was estimated as a product of the interpolated EToF and Spatial-CIMIS reference evapotranspiration.

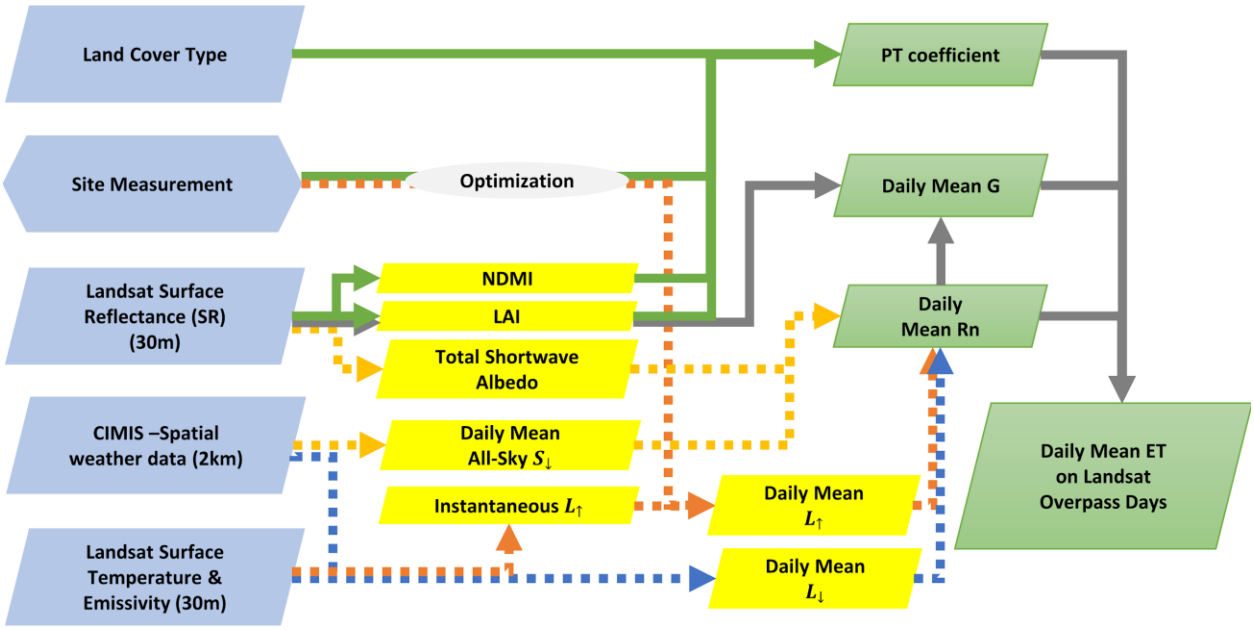

Figure 2. The flowchart of estimating daily evapotranspiration at 30 m during clear sky Landsat overpassing day.

2.6 *Validation and uncertainty analysis*

The uncertainty of Rn, actual Priestley Taylor coefficient, and daily evapotranspiration, directly estimated by our approach during clear-sky Landsat overpass days, was evaluated by comparison with the field measurements in the training, testing, and the full datasets, respectively. Four metrics were used to evaluate the method performance, including R^2, $1-\frac{\sum_{i=1}^{n}((P_i-M_i)^2)}{\sum_{i=1}^{n}\left((M_i-\underline{M})^2\right)}$, also known as Nash-Sutcliffe model efficiency coefficient; root mean squared error (RMSE), bias, where $Bias = \frac{\sum_{i=1}^{n}(P_i-M_i)}{n}$, and relative mean absolute difference (RMAD), $RMAD(\%) = \frac{\sum_{i=1}^{n}(|P_i-M_i|)}{\sum_{i=1}^{n}(M_i)} * 100\%$, where P and M are remote sensing estimates and field measurements respectively. We also summarized the statistics of the results from the cross-

validations, including the variance of the optimized parameters in Eq. 3, and the corresponding estimates of Priestley Taylor coefficient and evapotranspiration values.

Values of daily evapotranspiration that involved temporal interpolation were further evaluated during non-Landsat overpassing or cloudy days. An evaluation was also done for continuous daily, weekly, and monthly evapotranspiration estimates. The uncertainty introduced by the generalized optimization was also analyzed.

To compare our refined approach, hereafter referred to as PT-UCD, with previous Priestley Taylor approaches, we calculated the actual Priestley Taylor coefficients and evapotranspiration for all sites during clear-sky Landsat overpass days, following Jin et al., (2011)'s and Fisher et al., (2008)'s methods, hereafter referred as PT-0 and PT-JPL, respectively. All methods were driven by the same forcing data here, e.g., Rn, CIMIS-Spatial meteorological data, to evaluate the difference caused by the methods themselves. PT-0 did not apply the soil-moisture constraint for irrigated crops, and therefore its actual Priestley Taylor coefficients equation can be simplified as $\alpha = 1.22(1 - e^{-3.48LAI}) * f(T_a)$. To estimate PT-JPL evapotranspiration using Landsat time-series data, we modified PT-JPL's publicly accessible code (Fisher, 2008), which was written to estimates spatial evapotranspiration using monthly Advanced Very High Resolution Radiometer and The International Satellite Land Surface Climatology Project, Initiative II data (See Appendix I Text S1 for details).

3. Results

3.1 Net Radiation and Available Energy

The R_n estimated from our approach captured similar seasonal dynamics as observed by field measurements (Figure 3). For example, estimated Rn was close to 20 Wm^{-2} in January, increased continuously to 200 Wm^{-2} in June over an example alfalfa site (#2) and corn site (#14), and then started to decrease in July, reaching around 75 Wm^{-2} in October. An overestimation of Rn was found over Rice, mostly when the fields were flooded, e.g., during the growing season from April to October (Knox et al., 2016) and in winter. There is also a recurring underestimation of corn's Rn in between April and July for both sites 13 and 14, but not site 15 and 19.

Overall, the remote sensing-derived Rn agreed well with Rn measurements across all sites and overpassing days, with an overall R^2 of 0.74, an RMSE of 25.8 $Wm^{-2,}$ and an RMAD of 14.3% for the testing subset (Figure 4b). Only a small bias of 1.70 Wm^{-2} was found. The agreement was similar to the training subset, with an R^2 of 0.70 and an RMSE of 27.4 Wm^{-2} (Figure 4a). The uncertainties of Rn estimate varied by crop type, with the highest accuracy found for alfalfa, citrus, and pasture while relatively larger uncertainty for rice. Note that both evaluations using training and testing datasets were informative about the model's uncertainty because there was only one calibration for our Rn estimate, converting the instantaneous to daily outgoing longwave radiation on clear-sky Landsat overpassing days, which used only two sites (n = 94) in the training dataset.

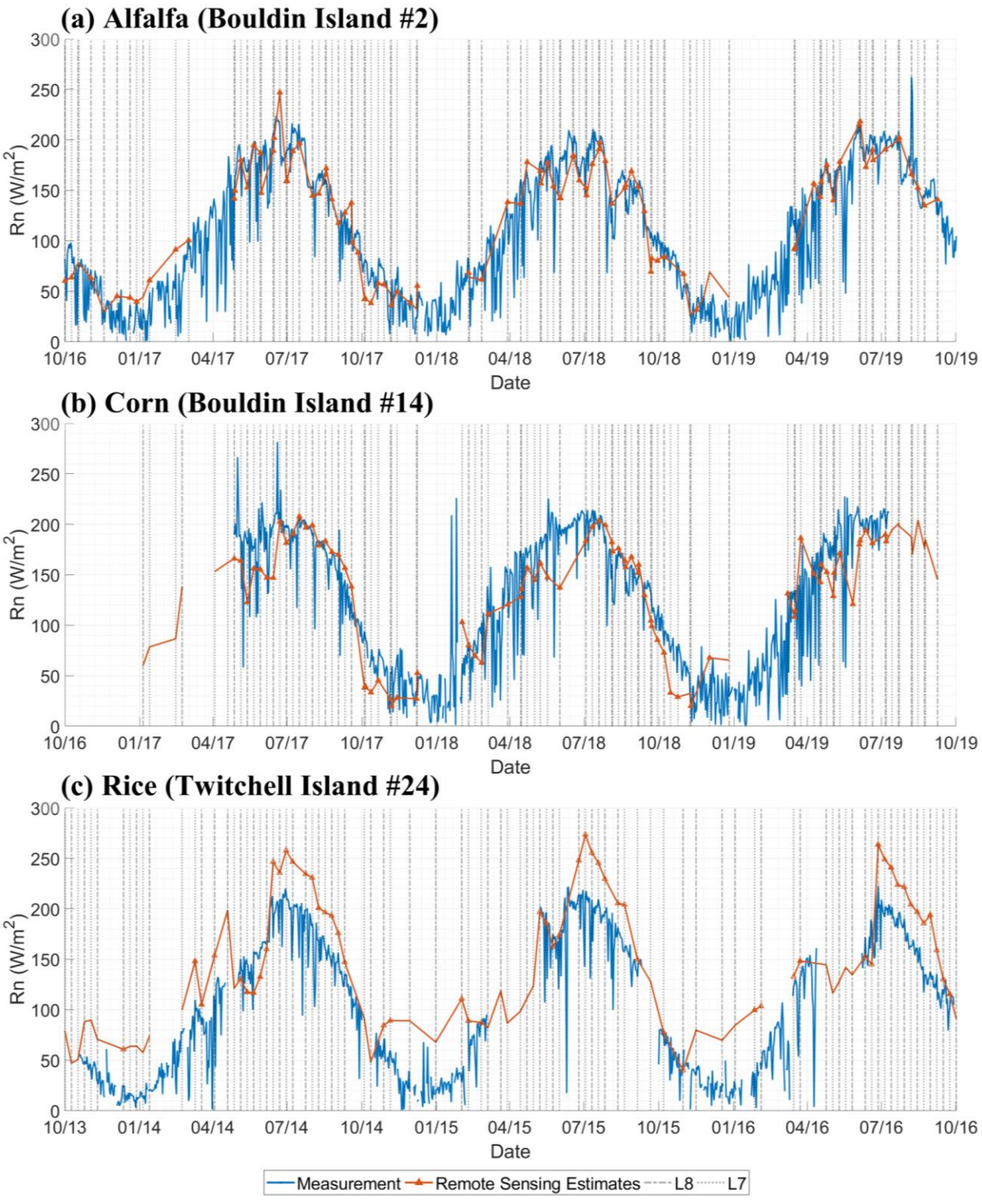

Figure 3. Time Series of Rn from daily measurements (blue) and estimates on clear-sky overpassing days (red) over (a) an alfalfa site at Bouldin island (#2); (b) a corn site at

Bouldin island (#14) and (c) a rice site at Twitchell Island (#24). The overpassing days of Landsat 7 and 8 are indicated by the vertical dash lines in grey.

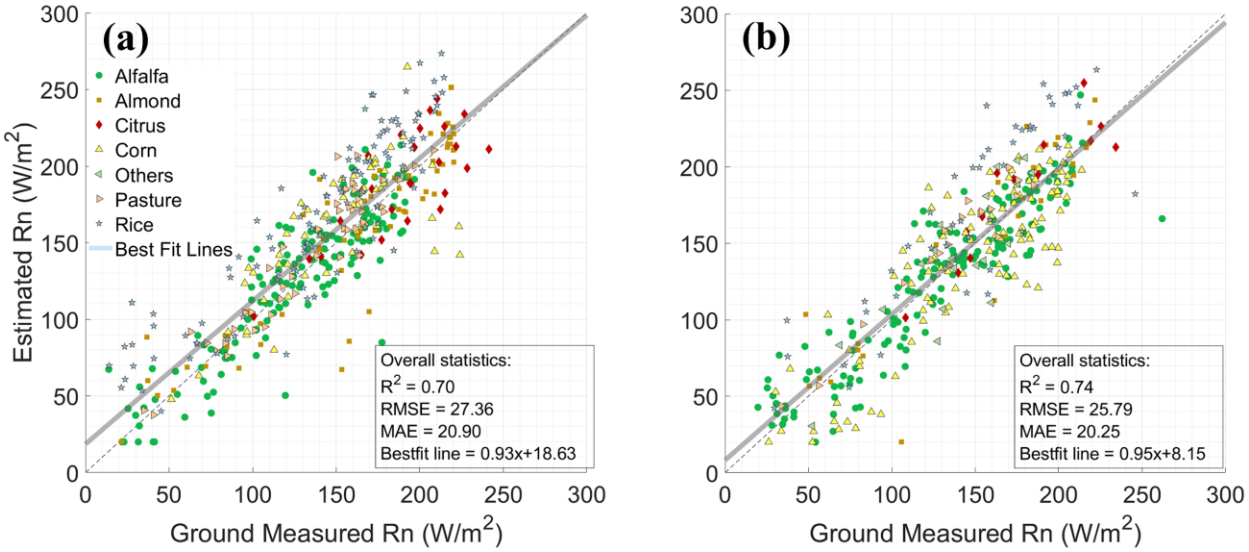

Figure 4. Comparison of remote sensing derived Rn vs. field measurements over all sites, from (a) training data (N=447) and (b) testing dataset (N=389).

3.2 Actual Priestley Taylor coefficients

The seasonal dynamics of the actual Priestley Taylor coefficient typically followed the plant growth curve, as shown by the values derived from both the field measurements and satellite observations (Figure 5). For example, the actual Priestley Taylor coefficients of alfalfa frequently fluctuated from 0.5 to 1.5, likely due to the multiple cuttings throughout the growing season, as shown by the similar variations in LAI (Figure 5a). Field measurements showed a substantial seasonal variation in the actual Priestley Taylor coefficient for the corn and rice sites, e.g., with towering peaks in summer growing season, a relatively small peak in spring, and much lower values in between fall and winter (Figures 5b, c).

In general, the remote sensing-derived actual Priestley Taylor coefficients, from the crop-specific optimization, could explain 56% of the variance observed across sites and periods, with an RMSE and RMAD of 0.23 and 17.7%, when compared with the field-based estimates over the testing dataset (Figure 6). For the generalized optimization, the uncertainties of actual Priestley Taylor coefficient estimates increased slightly (e.g., R^2= 0.50, RMSE = 0.26, and RMAD = 21.64%). Among crop types, both crop-specific and generalized actual Priestley Taylor coefficient estimation performs best for almond (RMAD = 8.2% and 9.4%). The performance of the crop-specific actual Priestley Taylor coefficient is significantly better than the generalized actual Priestley Taylor coefficients for corn and citrus.

The actual Priestley Taylor coefficient estimates showed significant improvement when compared to those derived from PT-0, which only captured small seasonal variation (25%) and had a higher bias of 0.24 and a larger RMAD of 34.7% over the irrigated cropland in the valley (Figure 5). In contrast, PT-JPL estimates showed a reasonable seasonal pattern for alfalfa and corn (Figures 5a, b), although it was not calibrated for any land cover type (RMSE = 0.32, and RMAD = 27.3%). Across all sites, the crop-specific PT-UCD showed an overall improvement over PT-JPL, as shown by the empirical cumulative distribution function of the absolute errors when compared to both testing and independent testing data (Figure 7a). For example, 88% of testing samples had an absolute error of below 0.30 from crop-specific PT-UCD estimates, compared to 62% and 59% from PT-JPL and PT-0 estimates, respectively. The generalized PT-UCD performed only slightly better than PT-JPL (Figure 7a).

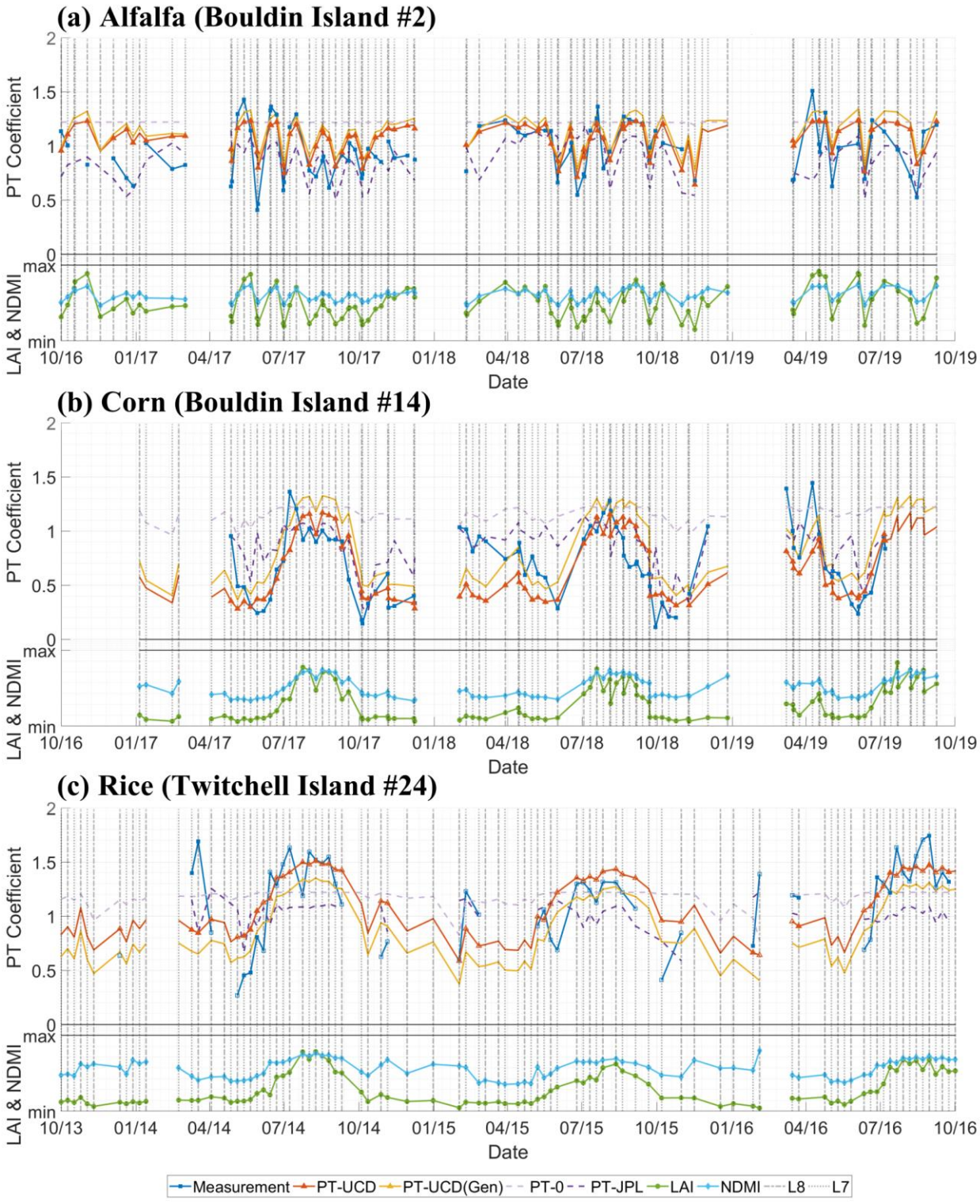

Figure 5. Time series of crop-specific (red) and generalized (yellow) PT coefficients derived from tower observations and crop-specific remote sensing estimates, over the

same three sites as shown in Figure 3. The un-filled symbols on overpassing dates indicate that the data points were previously partitioned into the training dataset. The estimates from the other two PT approaches, namely PT-0 and PT-JPL, were also shown for comparison. The lower panel shows the corresponding LAI and NDMI in green and cyan (lower panel), ranging from 0 to 7 and -1 to 1, respectively. All three Priestley Taylor methods shown here were driven with the same forcing data.

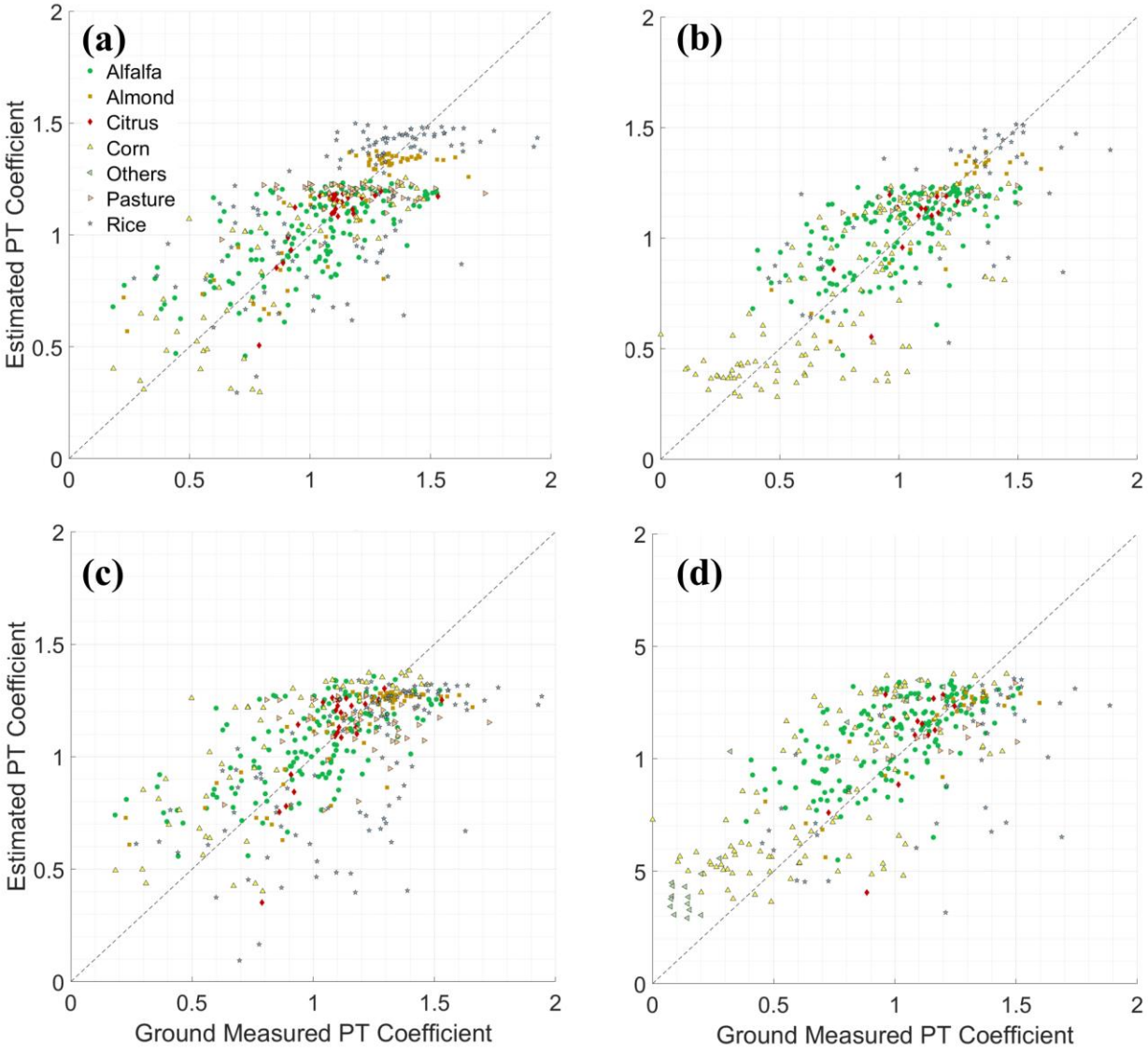

Figure 6. Comparison of remote sensing PT coefficient, derived from crop-specific optimization parameters, vs. field measurements on Landsat overpassing days over all sites, based on (a) training data (N=447) and (b) testing dataset (N=368). The corresponding results, when using generalized optimization, are shown in the bottom panel (c) and (d).

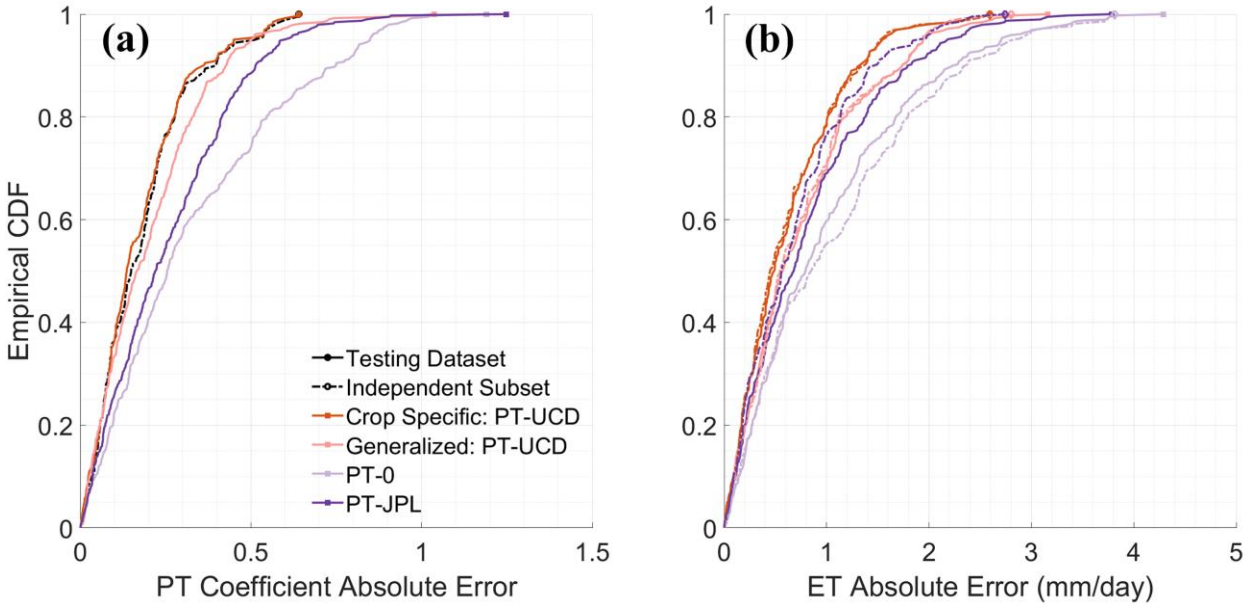

Figure 7. Comparison of empirical cumulative distribution errors among estimated (a) PT coefficient and (b) evapotranspiration using four models on clear-sky Landsat overpassing days. All three Priestley Taylor methods shown here were driven with the same forcing data.

Two types of cross-validation testing further showed the optimization of the parameters in Eq. 3 for estimating the actual Priestley Taylor coefficient was reasonably robust. The distribution of the estimated parameters showed a very small variance, for the majority of the crops and the generalized optimization (Appendix I Table S1). One exception was Parameter D, which represented the moisture regulation over the coefficient, for citrus and pasture (typically

well-watered). The estimated actual Priestley Taylor coefficients were shown to be stable among the repeat and leave-two-out cross-validations (Figure 8 a,b 9-11 a), with an Interquartile Range (IQR) of RMAD of less than 5% (Figure 8a).

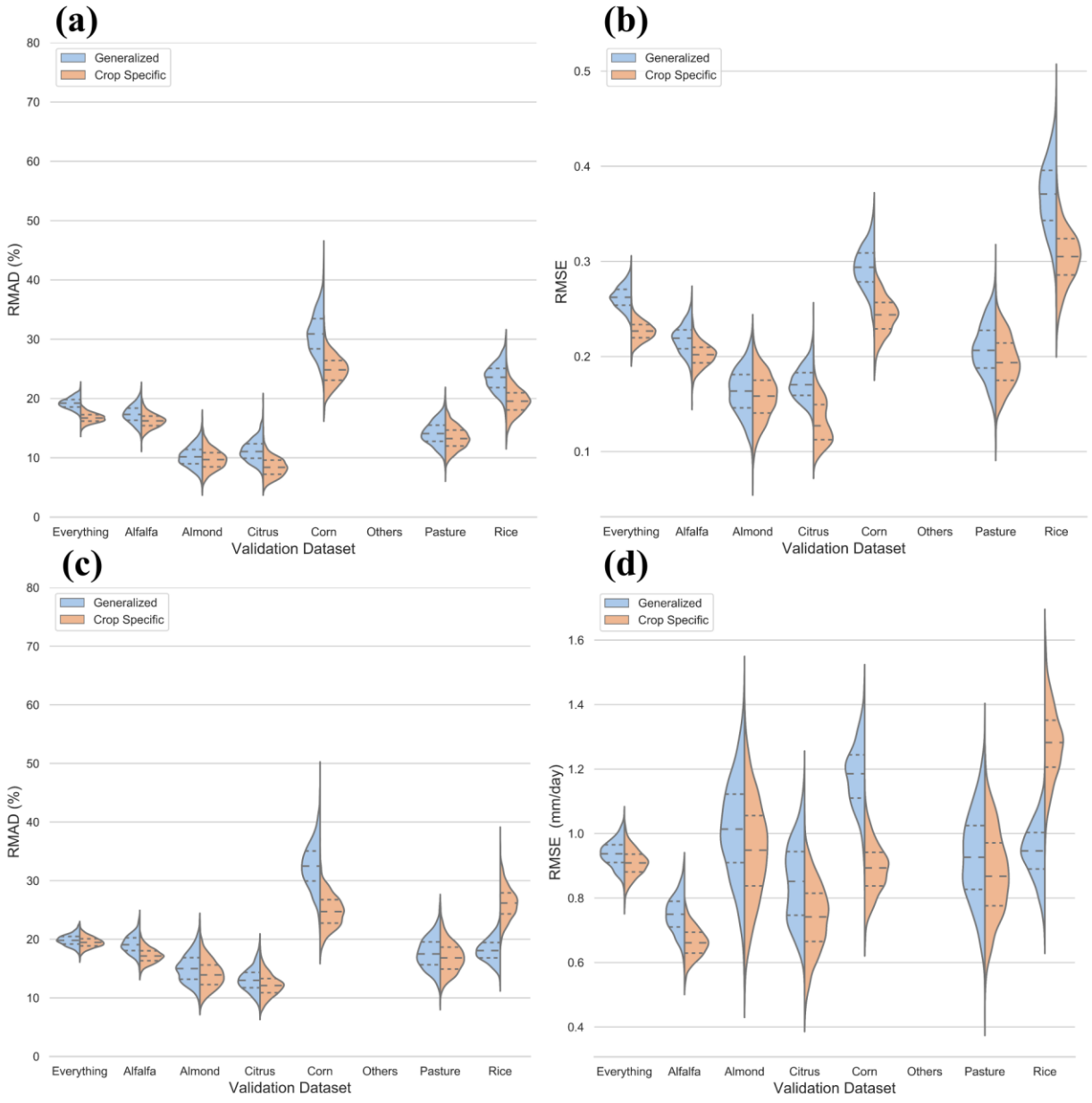

Figure 8. Distribution of RMAD (a, c), RMSE (b, d) of Priestley Taylor coefficients (Top), and evapotranspiration (Bottom) from the repeated cross-validation approach.

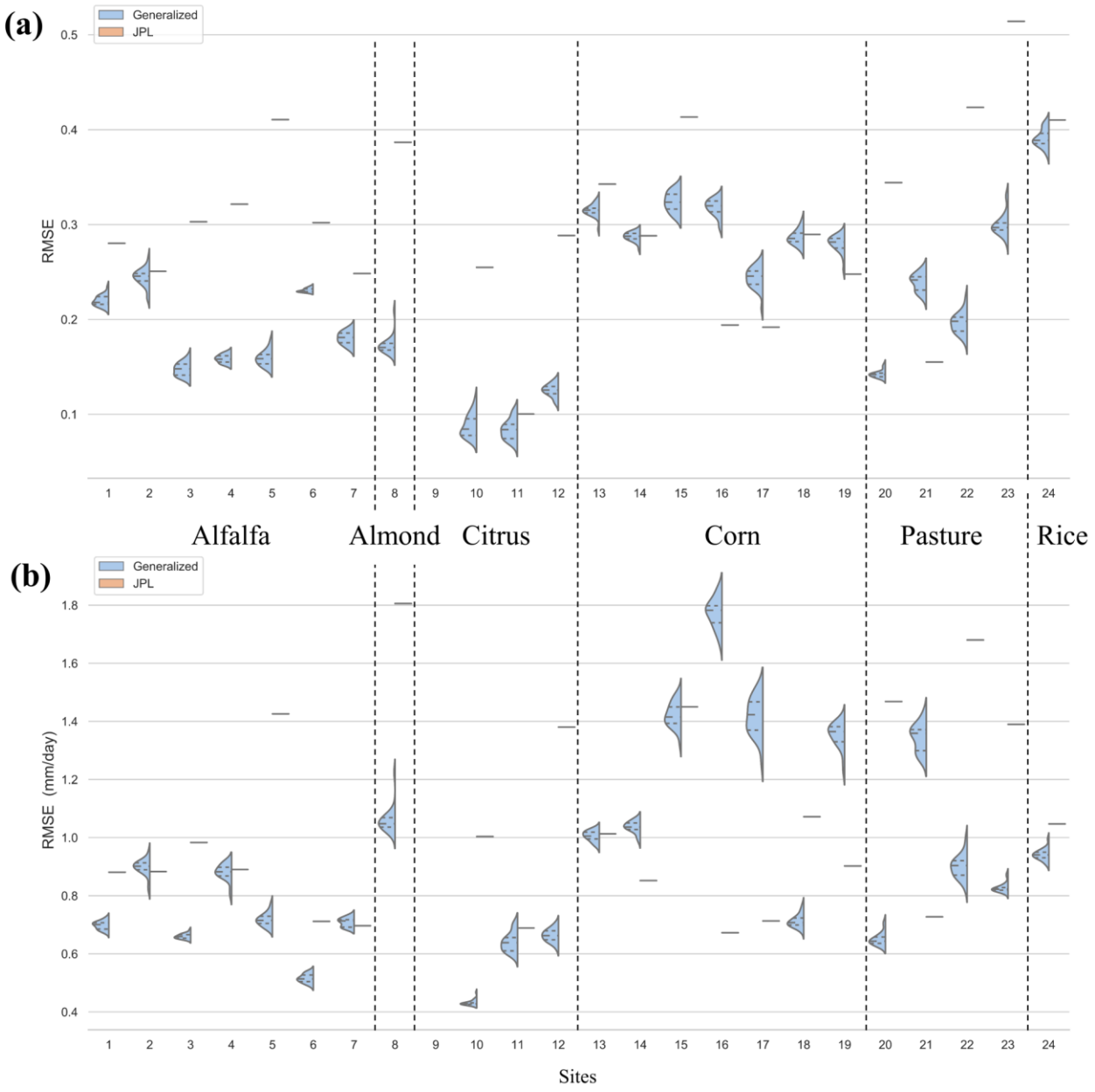

Figure 9. RMSE distribution for the actual Priestley Taylor coefficients (Top) and evapotranspiration (Bottom), comparing the performance of generalized PT-UCD against PT-JPL over testing data from the leave-two-out cross-validation approach at individual sites. Both PT-UCD and PT-JPL methods shown here were driven with the same forcing data.

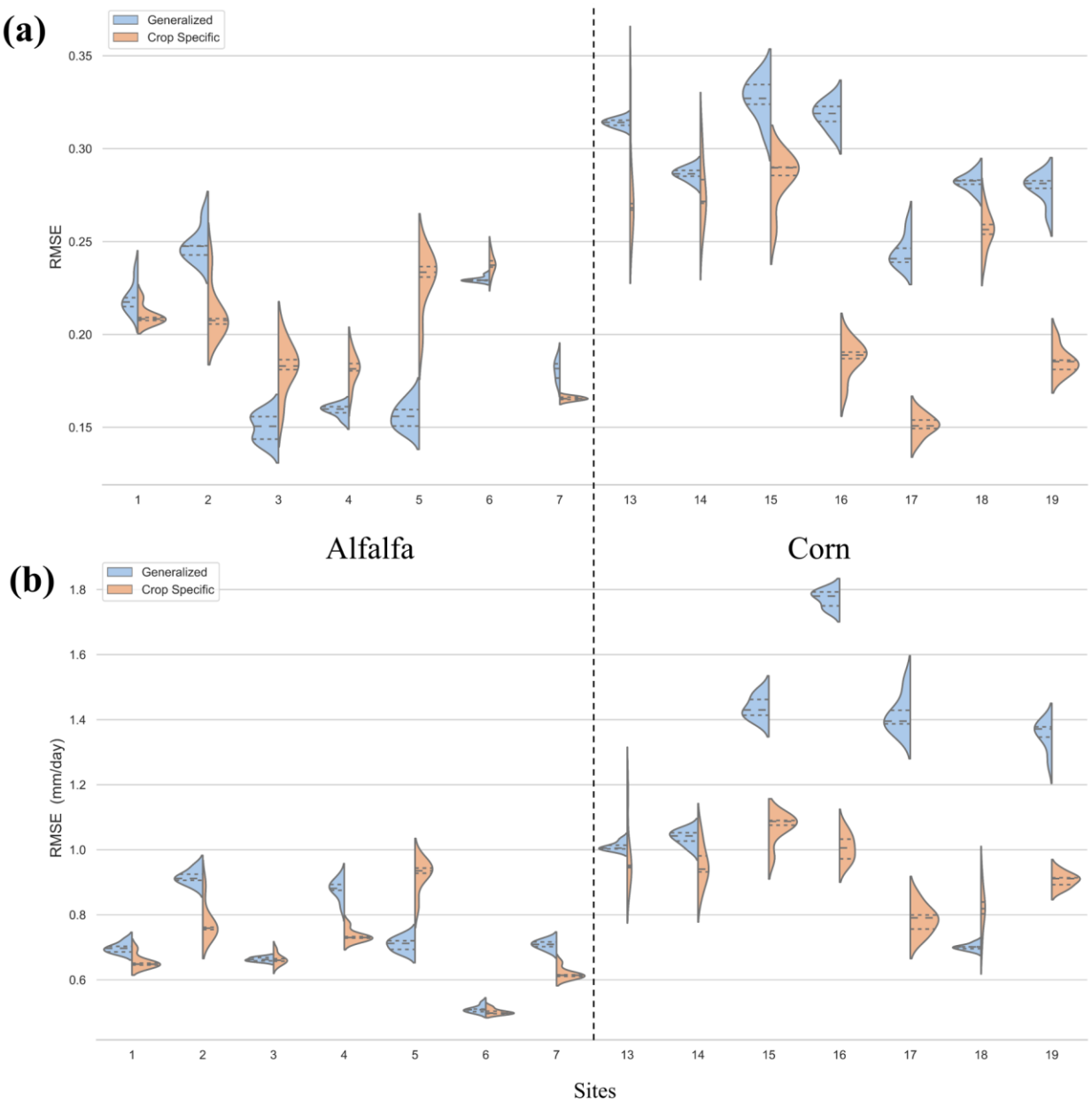

Figure 10. RMSE distribution for Priestley Taylor coefficients (Top) and evapotranspiration (Bottom), comparing the performance of generalized against crop-specific PT-UCD over testing data from the leave-two-out cross-validation approach at individual alfalfa or corn sites.

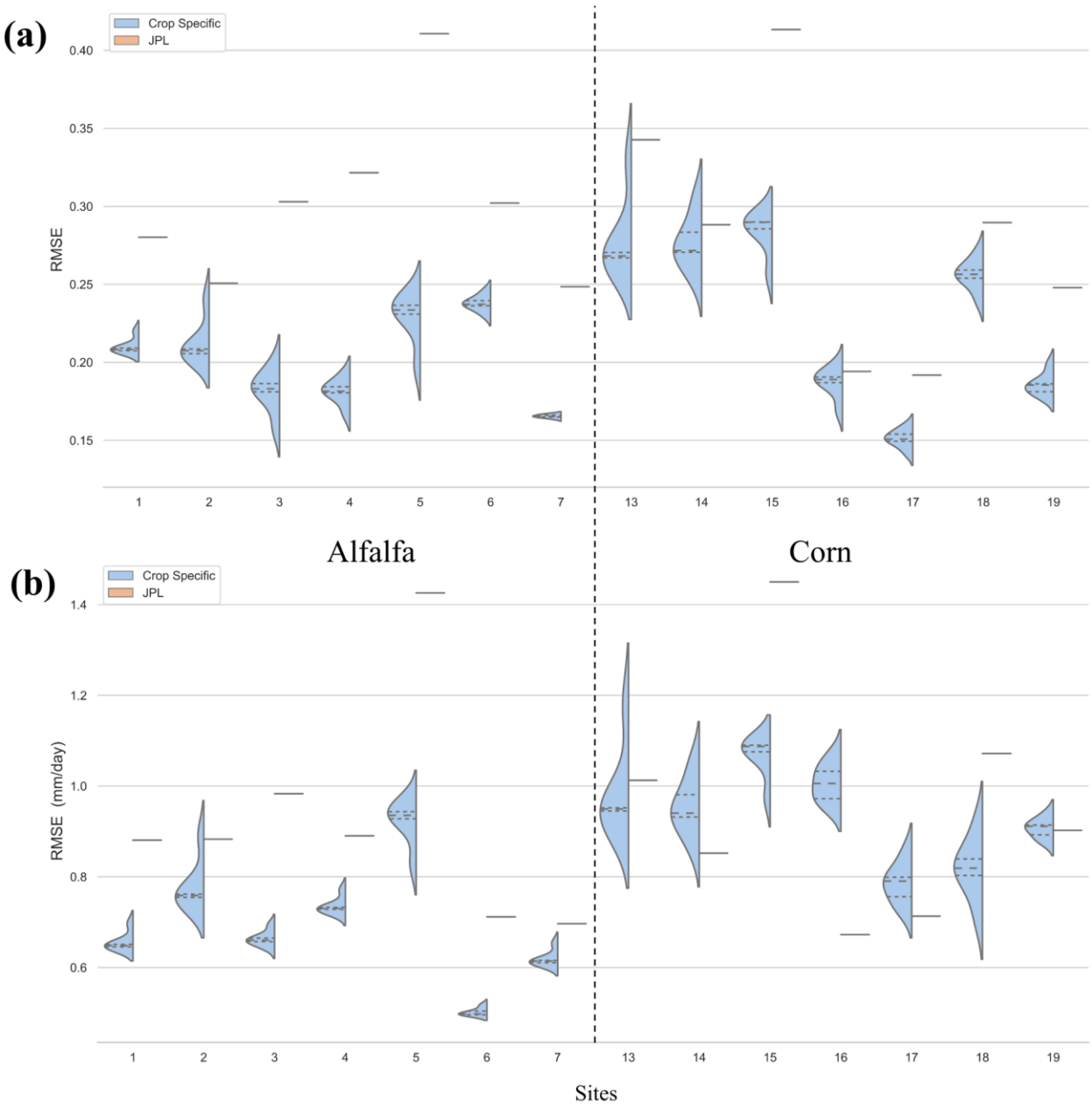

Figure 11. RMSE distribution for Priestley Taylor coefficients (Top) and evapotranspiration (Bottom), comparing the performance of crop-specific PT-UCD against PT-JPL over testing data from the leave-two-out cross-validation approach at individual alfalfa or corn sites. Both PT-UCD and PT-JPL methods shown here were driven with the same forcing data.

3.3 Evapotranspiration estimates

3.3.1 Daily mean evapotranspiration on clear-sky Landsat overpassing days

We found a good agreement between field measurements of evapotranspiration and satellite-based estimates during the clear-sky days with Landsat acquisitions. When evaluated with the testing dataset, both the crop-specific and generalized evapotranspiration models captured the seasonal variability well (Figure 12). Across all sites, the crop-specific evapotranspiration had an R^2 of 0.79, RMSE of 0.90 mm day^{-1}, and RMAD of 20.5% (Figure 13b). Only a small bias of 0.14 mm day^{-1} was found. When using the generalized actual Priestley Taylor coefficients, slightly higher uncertainties were found, with an R^2 of 0.76, RMSE of 0.98 mm day^{-1}, and RMAD of 23.1% (Figure 13d).

The performance of evapotranspiration estimates varied by crop types. When using the crop-specific Priestley Taylor optimization, the RMSE and RMAD ranged from 0.68 to 1.34 mm day^{-1} and 13.3% to 28.4%, based on the comparison with the testing dataset (Table 2). The best performance was found for alfalfa, citrus, and pasture sites, while the weakest performance in rice. The generalized approach also performed the best for alfalfa and citrus and performed the poorest for rice and corn (Figure 8, 11b, Appendix I Table S2). The leave two out cross-validation showed relatively small differences in RMSEs of daily ET estimates from site to site (Figure 10b), e.g., 0.7 mm day^{-1} in alfalfa site #6 vs. 0.9 mm day^{-1} in site #5 based on the results from alfalfa-specific optimization, and 0.7 to 1.2 mm day^{-1} among the corn sites.

Crop-specific PT-UCD showed an improvement over PT-0, PT-JPL, and generalized PT-UCD. About 80% of crop-specific evapotranspiration estimates in the testing and independent dataset had an error of less than 1 mm day^{-1}, as shown by the empirical cumulative distribution

functions of the absolute errors between the daily crop-specific evapotranspiration estimates and field measurements (Figure 12b). In contrast, both generalized PT-UCD and PT-JPL appeared to perform similarly, i.e., about 70-76% of samples had an evapotranspiration error less than 1mm day^{-1}, and about 85-90% less than 1.5 mm day^{-1}. However, for the PT-0 evapotranspiration estimates, only 55% and 70% of samples had an error less than 1mm day^{-1} and 1.5 mm day^{-1}, respectively.

Table 2. Comparison of daily evapotranspiration estimates from three Priestley Taylor approaches with field measurements during days with clear-sky Landsat observations and other days (from temporal interpolation). For clear-sky overpassing days, statistics were based on the full dataset, the testing dataset only (in parenthesis), respectively.

Crop types	**R^2**				**RMSE (mm day^{-1})**			
	PT-0	PT-JPL	PT-UCD		PT-0	PT-JPL	PT-UCD	
	Clear Sky Overpassing Days			Interpolated	Clear Sky Overpassing Days			Interpolated
Alfalfa	0.64 (0.57)	0.69 (0.71)	0.83 (0.82)	0.75	0.94 (1.05)	0.87 (0.86)	0.65 (0.68)	0.77
Almond	0.78 (0.78)	0.48 (0.53)	0.85 (0.86)	0.89	1.13 (1.18)	1.73 (1.72)	0.95 (0.94)	0.86
Citrus	0.40 (0.24)	<0 (<0)	0.70 (0.56)	0.70	0.99 (1.08)	1.39 (1.48)	0.69 (0.83)	0.86
Corn	0.18 (0.11)	0.72 (0.70)	0.75 (0.71)	0.68	1.65 (1.66)	0.97 (0.97)	0.91 (0.96)	1.01
Pasture	0.75 (0.66)	0.42 (0.36)	0.77 (0.72)	0.69	0.86 (0.86)	1.31 (1.81)	0.82 (0.77)	0.94
Rice	0.80 (0.77)	0.80 (0.72)	0.75 (0.67)	0.77	1.03 (1.11)	1.03 (1.25)	1.16 (1.34)	1.09
All (Crop Specific)	N/A	N/A	0.81 (0.79)	0.80	N/A	N/A	0.87 (0.90)	0.93
All (Generalized)	0.70 (0.57)	0.70 (0.71)	0.80 (0.76)	0.78	1.15 (1.32)	1.12 (1.07)	0.91 (0.98)	0.95

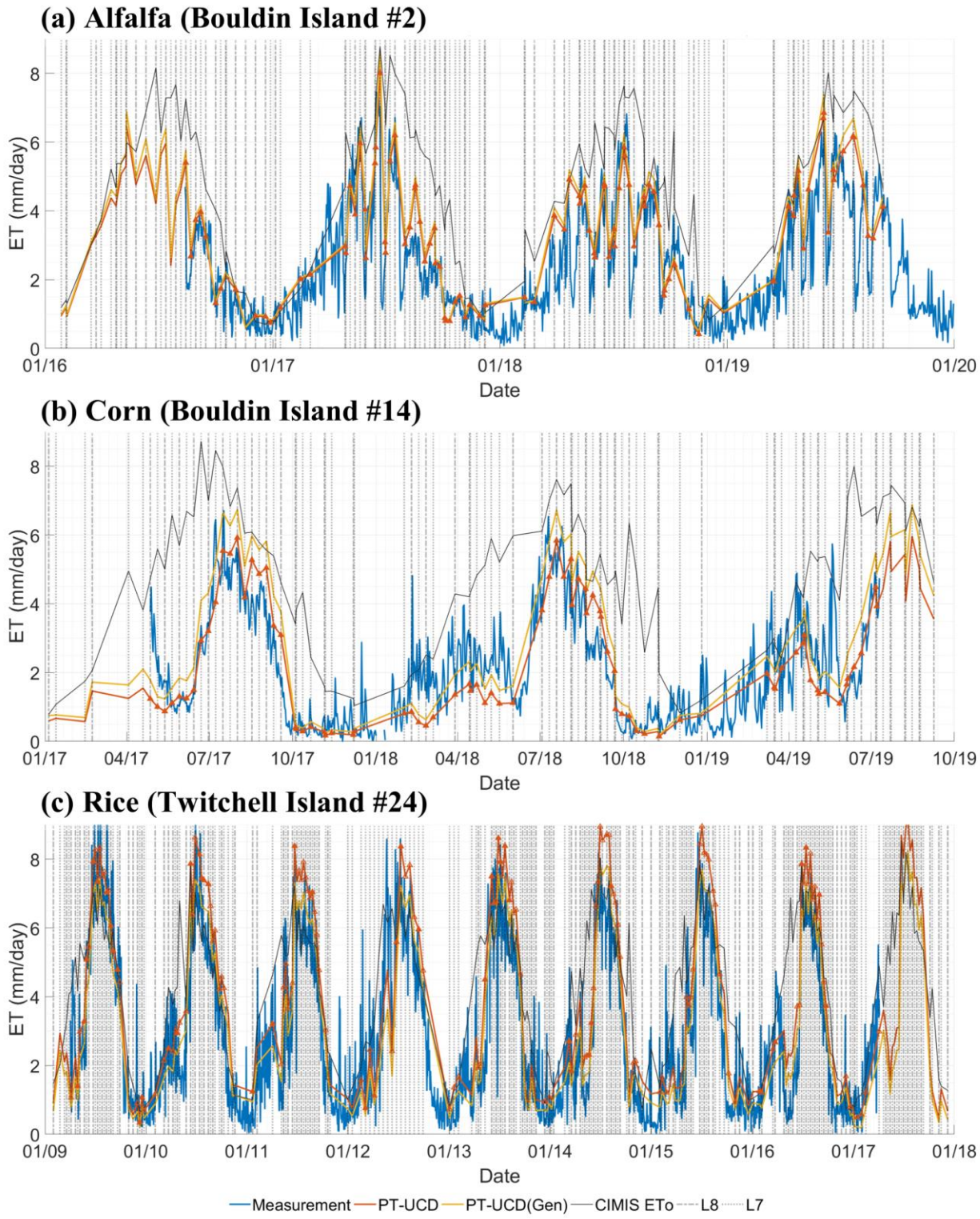
(a) Alfalfa (Bouldin Island #2)
ET (mm/day)
0
2
4
6
8
01/16
01/17
01/18
01/19
01/20
Date
(b) Corn (Bouldin Island #14)
ET (mm/day)
0
2
4
6
8
01/17
04/17
07/17
10/17
01/18
04/18
07/18
10/18
01/19
04/19
07/19
10/19
Date
(c) Rice (Twitchell Island #24)
ET (mm/day)
0
2
4
6
8
01/09
01/10
01/11
01/12
01/13
01/14
01/15
01/16
01/17
01/18
Date
Measurement
PT-UCD
PT-UCD(Gen)
CIMIS ETo
L8
L7

Figure 12. Time Series of crop-specific and generalized (yellow) evapotranspiration vs. daily evapotranspiration measurement. The un-filled symbols on overpassing dates indicate that the data points were previously partitioned into the training dataset.

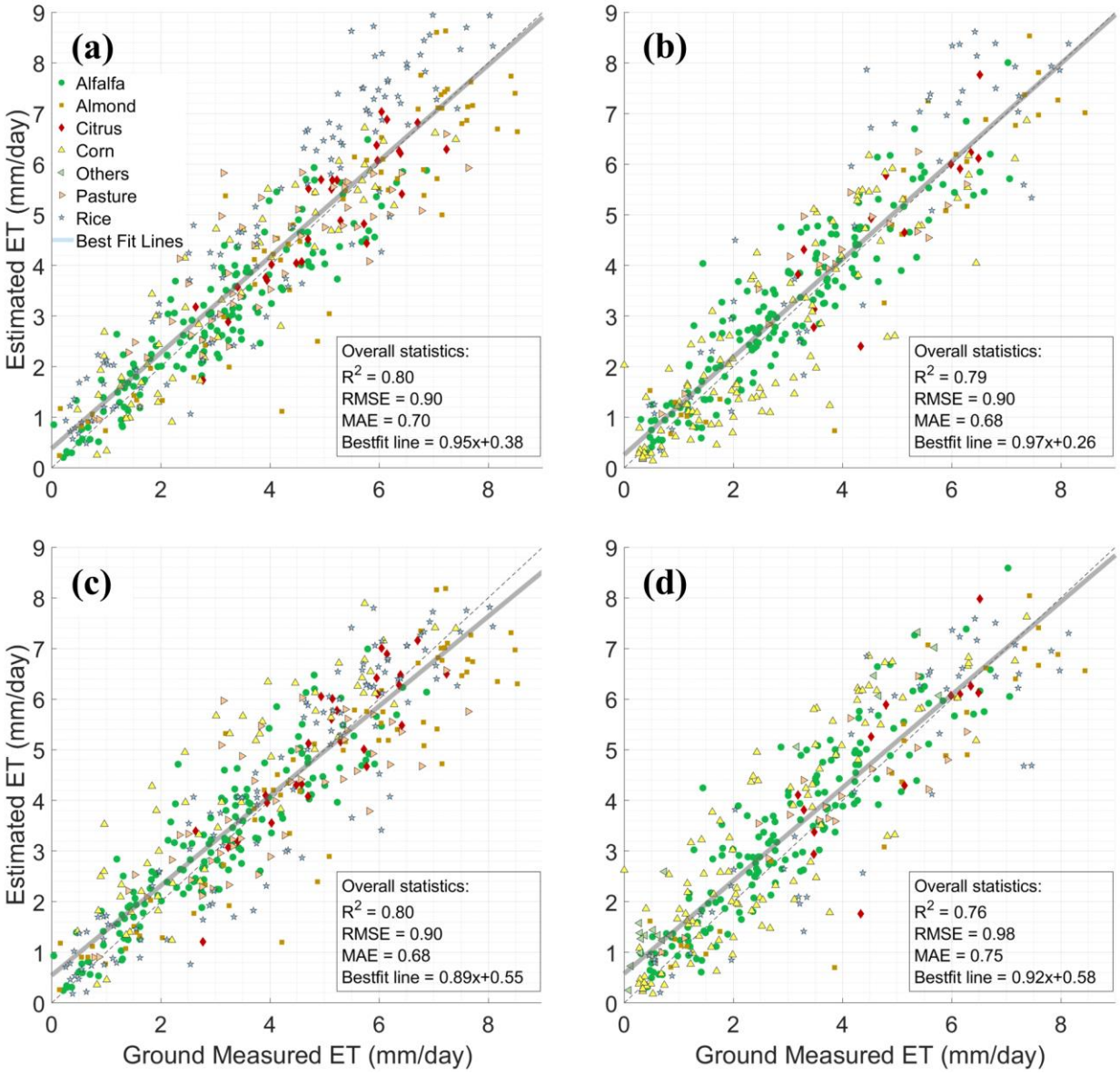

Figure 13. Comparison of remote sensing-derived daily evapotranspiration vs. field measurements on Landsat overpassing days over all sites, based on (a) training data (N=345) and (b) testing dataset (N=149), when using crop-specific optimization

parameters. The corresponding results from the generalized optimization are shown in (c) and (d).

3.3.2 Continuous evapotranspiration estimates

The interpolation of EToF from adjacent overpassing days introduced a small overall uncertainty in daily evapotranspiration estimates, e.g., RMSE increased by 0.10 – 0.17 mm day^{-1} and decreased R^2 by 0 – 0.08 when estimating evapotranspiration for alfalfa, citrus, corn, and pasture (Table 2, Figure 14). When further aggregated to weekly and monthly time scales, the satellite-derived evapotranspiration estimates agreed better with those from the field measurements (Figures 15). For example, across all sites, R^2 was increased to 0.83 and 0.88, and RMSE reduced to 0.79 and 0.65 mm day^{-1}, respectively, for weekly and monthly evapotranspiration values based on the crop-specific Priestley Taylor optimization.

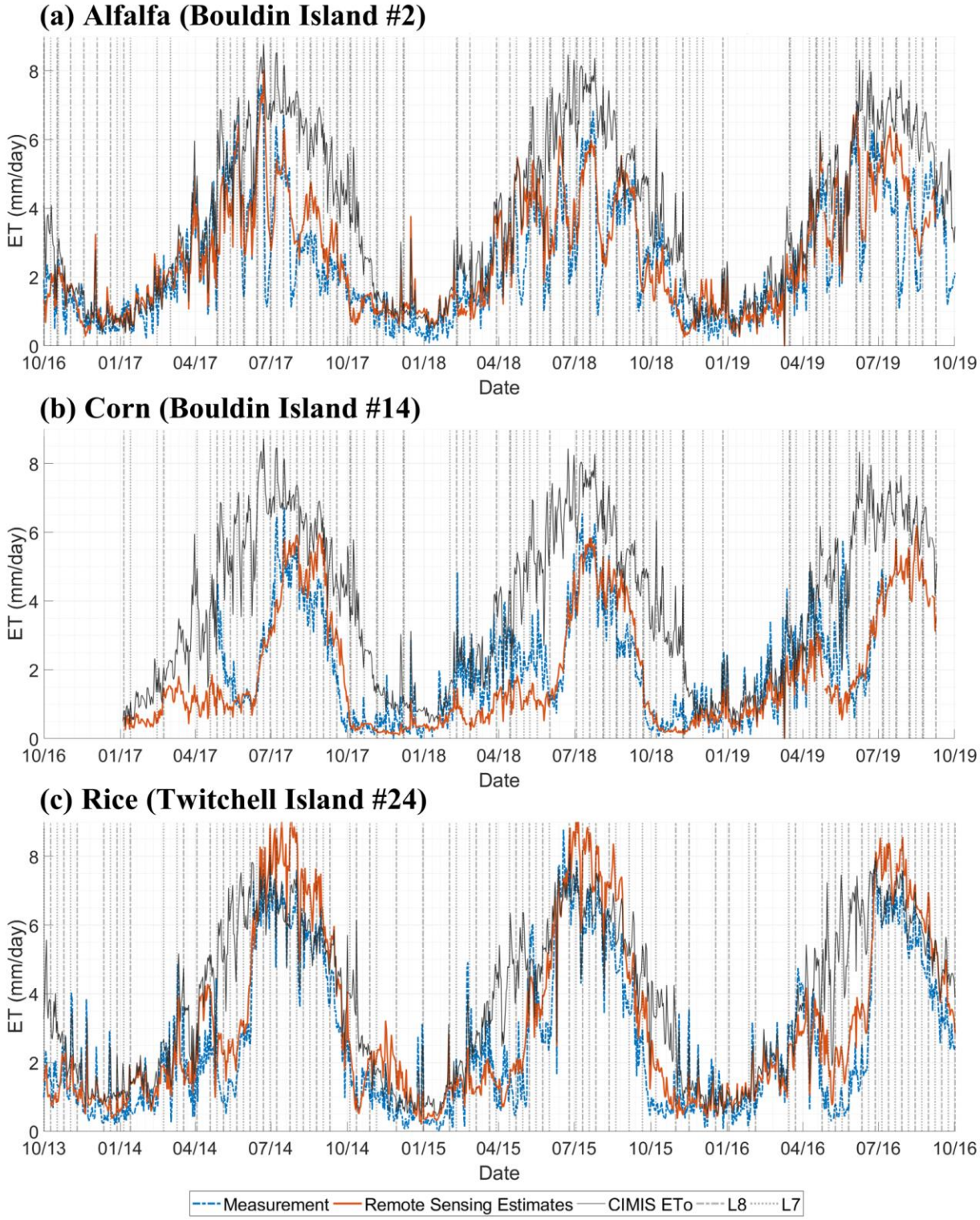

Figure 14. Time Series of crop-specific and interpolated evapotranspiration vs. daily evapotranspiration measurement.

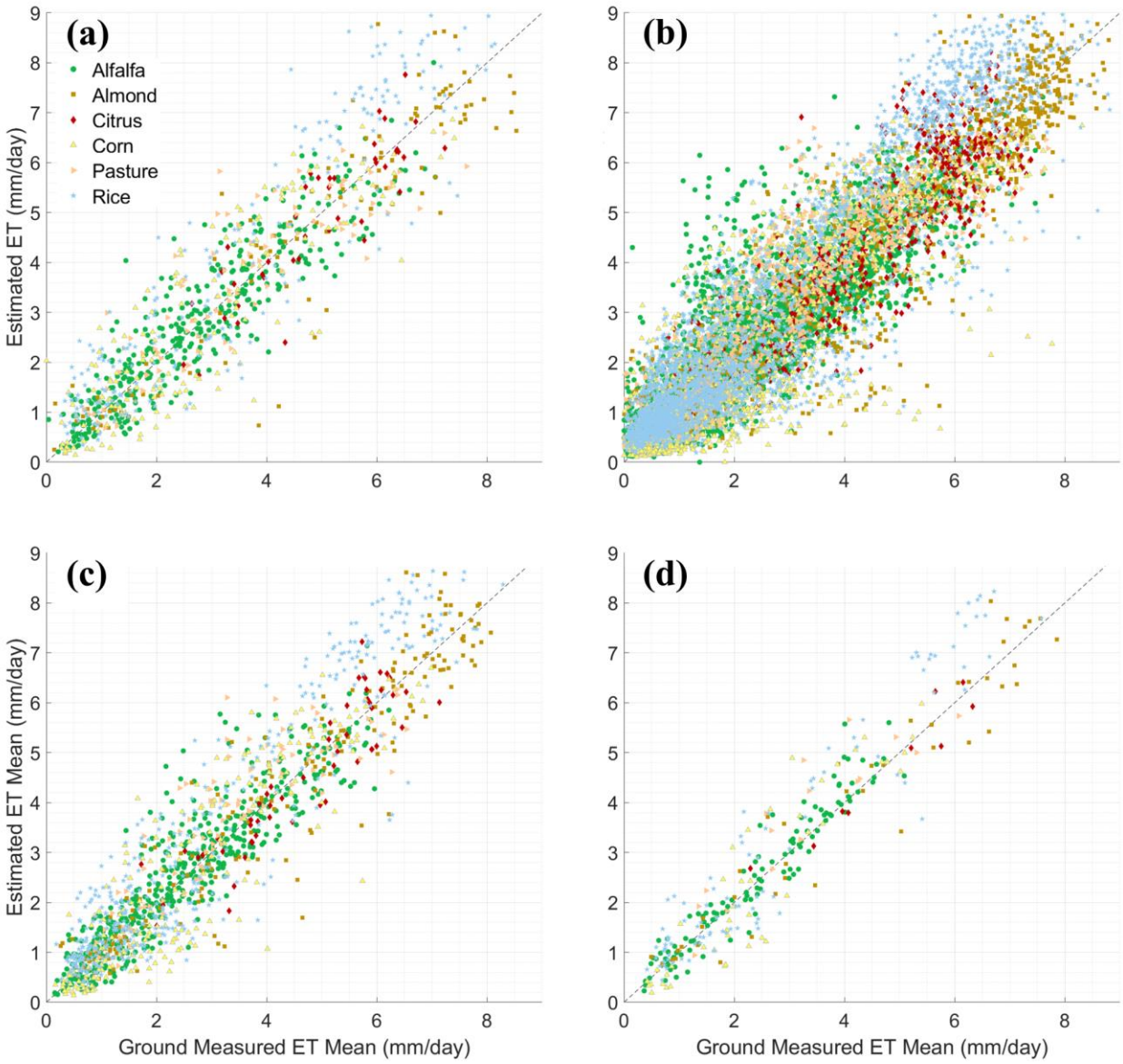

Figure 15. Comparison of remote sensing-derived evapotranspiration using crop-specific parameterization over all sites during (a) Landsat overpassing days (N=600) and (b) days without clear-sky Landsat imagery (N=5600). Aggregated mean evapotranspiration at (c) weekly (N=1046) and (d) monthly (N=249) time scales are also shown.

4. Discussion

4.1 Site-level performance

Our study showed that the semi-empirical Priestley Taylor algorithm, when calibrated with ground measurement data over diverse crop types and driven by Landsat Analysis Ready Data, improved the accuracy of the older 1 km MODIS-driven PT-0 model (Jin et al., 2011). The crop-specific Priestley Taylor optimization performed consistently between the testing and independent datasets, and slightly better than the PT-JPL method (Fisher et al., 2008) (Figure 7, 11). The generalized Priestley Taylor optimization had a similar overall performance with PT-JPL when driven by the same input data. However, relatively larger uncertainties were found during non-growing seasons, from November to March, when the evapotranspiration rate was relatively low. This was partly due to the limited field measurements data during winter and early spring for optimizing the sensitivity of actual Priestley Taylor coefficients to the moisture content. Moreover, our Priestley Taylor approach does not separate soil evaporation and plant transpiration. This introduces uncertainty in evapotranspiration estimates during non-growing seasons when evapotranspiration is mainly driven by evaporation from the soil due to minimal canopy coverage or leaf area. For example, we did find that PT-JPL better captured the peak of the actual Priestley Taylor coefficient for the corn site during the dormant season (Figure 5b), when PT-JPL's estimates showed that soil evaporation was the most significant component.

The uncertainty of our refined Priestley Taylor approach here is similar to the DisALEXI model, as shown by the report from the Sacramento San Joaquin Delta inter-comparison project (Medellín-Azuara, J. et al., 2018). For additional reference, Anderson et al., (2018) reported that DisALEXI had an RMSE of 1.09 mm day^{-1} at site number 1 (alfalfa) and 1.24 mm day^{-1} at site

number 24 (rice) when compared to daily measurements. Being a process-based model, DisALEXI does not depend on land use maps and field measurements for calibration once validated. The semi-empirical Priestley Taylor approach, however, has the advantage of easy implementation, compared to other more sophisticated and computationally more expensive approaches.

Remote sensing evapotranspiration estimates, if properly calibrated and validated with locally available measurements, are well suited for soil water balance in groundwater models during non-rainy seasons over agricultural areas, especially in semi-arid regions such as California's Central Valley. Based on the most recent fine grid groundwater-surface water simulation model (Sustainable Groundwater Management Office, 2020), DWR estimated that monthly percolation, between water years 2003 and 2015, at the root zone, over all croplands in the Central Valley, ranges from 0.23 mm day^{-1}in dry winter to 1.32 mm day^{-1} in summer. Meanwhile, the ratio of percolation to DWR's actual evapotranspiration estimates ranges from a minimum of 22% in summer to a maximum of 193% in winter. During non-rainy seasons, e.g., between May and September, applied water estimates are primarily driven by evapotranspiration. The estimated applied water value affects soil moisture computation in the root zone, which in turn affects percolation estimates. Therefore, during non-rainy seasons, the derived ratio could be used to approximate percolation from evapotranspiration. From section 3.3.2, we found that our monthly averaged evapotranspiration has an overall RMSE of 0.65 mm day^{-1}. By adding or subtracting DWR's actual evapotranspiration by our overall RMSE value, and then multiplying it with the previously derived ratio to approximate percolation, a maximum deviation of $\pm$30% (about 0.23 mm day^{-1}) from the original value, during the non-rainy season, was found in September, and the minimum of $\pm$14-15% (about 0.15 mm day^{-1}) was found in July.

4.2 Limitation and potential improvement

Although overall our refined evapotranspiration estimation approach here has similar performance to that in more complex models such as DisALEXI (Anderson et al., 2018; Medellín-Azuara, J. et al., 2018), there are still a few factors that can cause errors in our estimates. PT-UCD is a single-source approach. We noticed an overestimation of rice net radiation when the field was flooded, probably due to the challenges posed by heat storage in the water column and the effect of a wet surface, and an underestimation of net radiation over the two Ameriflux corn sites between every April and July. We also found a larger uncertainty in estimating actual Priestley Taylor coefficients for corn during the dormant season between January and April. Although evapotranspiration during the non-growing season accounts for a small fraction of total annual water use, explicit consideration of soil and plant components of energy balance is expected to improve the accuracy of evapotranspiration estimates. Besides, the research community often views the remote sensing-based Priestley Taylor approach to over-simplified the actual evapotranspiration process in irrigated fields. The novelty of the proposed approach could be enhanced through more theoretical research. For example, the Priestley Taylor coefficient estimation can be formulated in the terms of input variables, such as aerodynamic and canopy surface resistances from the Penman-Monteith equation, which can be further tested with all datasets that were previous used in Penman-Monteith related studies (see Appendix II for the proposed method).

The errors of field measurements of evapotranspiration can propagate to the optimization. The energy balance closure issue, for example, has been well recognized for the eddy covariance measurements (Twine et al., 2000; Wilson et al., 2002). Baldocchi et al., (2016) and Eichelmann et al., (2018), for example, conducted several analyses at AmeriFlux sites in the Sacramento San

Joaquin Delta and found closure of 79.3% in an alfalfa site, i.e., the ratio of the sum of sensible and latent heat flux over the residual between net radiation and ground heat flux and storage, and 71% in a rice site. Their study suggests that incomplete storage calculation, rather than underestimation of eddy covariance measurements of fluxes, plays a major role in the lack of energy balance closure for their sites in the Sacramento San Joaquin Delta. Therefore, we did not perform the correction for eddy covariance measurement sites from our dataset.

Additional uncertainties can be introduced due to the varying footprint size of the flux towers and the scale mismatch between 30m ET and tower measurements. We compared the annual evapotranspiration value extracted from a single Landsat pixel collocated with measurement sites and the mean (and standard deviation) of the values within the surrounding larger areas (Appendix I Table S3). The differences in estimates between a 90m by 90m window and the single-pixel were small, with the largest difference of -3.2% occurred at site 18 in 2016. The differences generally increased with a larger footprint, depending on the heterogeneity of the areas, e.g., over a 510 m by 510 m window at site 16 (corn) in 2016 had the largest mean relative difference of -10.3% from the corresponding center pixel value. Other studies also suggested that a rigorous footprint approximation is needed in future studies to make a fair comparison with field measurements (Anderson et al., 2018). For example, the Kljun et al., (2015) flux footprint model could be implemented at flux tower sites to determine the weight and extent of the pixel window.

Compared to those driven by MOIDS with daily revisiting (Jin et al., 2011), the evapotranspiration estimates derived from Landsat have the benefit of capturing finer spatial details, which is critical for water use assessment over a heterogeneous landscape. Landsat's 16-day repeating cycle, however, can potentially lead to uncertainty in water use monitoring,

especially during the rainy season or during the rapid plant growth and senescence stages. In this study, the uncertainty due to the temporal interpolation of the missing days was found minimal overall, likely because the rainy season coincides with dormancy or the very beginning or ending of the crop growth for the majority of crops in Central Valley due to its Mediterranean climate (Figure 14, Table 2, Appendix I Table S4). There were situations, e.g., right after irrigation or right after harvesting for crops that undergo multiple harvests (alfalfa), when a relatively large error was introduced from the estimates interpolated from observations a few days apart. Future work is also needed to increase the temporal resolution of water use estimate by fusing Sentinel 2 A&B satellite observations every 5 days with Landsat data. A sophisticated data fusion technique will also improve the accuracy of evapotranspiration monitoring and assessment, by taking advantage of complementary observations from multiple sensors (Anderson et al., 2018).

The robustness of our optimization approach partly relies on the availability of multiple field measurements for diverse crop types across the Central Valley. The automatic workflow developed here allows for a continuous improvement of the optimization accuracy, by taking advantages of the increasingly available crop evapotranspiration measurements with the increased deployment of both research-grade and commercialized surface renewal stations in the state (Clay et al., 2019; Jin et al., 2018; Souto et al., 2019; Xue et al., 2020). Although the Priestley Taylor parameters in this study were tailored for California's cropland, our data-model integration framework is generalizable to other regions. Once recalibrated and tested with local field data, the PT-UCD approach can be applied to monitor daily evapotranspiration and assess water use at various scales over regions besides the Central Valley.

5 Conclusions

To enable estimation of agriculture consumptive water use at the field scale in Central Valley, we further refined the semi-empirical Priestley-Taylor approach (Jin et al., 2011), by optimizing the actual Priestley Taylor coefficient as a function of LAI and moisture index with recently compiled ground measurements of evapotranspiration for California's major crops. The net radiation estimates with Landsat Analysis Ready Data had an RMSE of 25.8 Wm^{-2} and R^2 of 0.74. Our study shows that the crop-specific optimization with field data is relatively robust, and the locally optimized approach captured well the regulation of plant growth and moisture stress on latent heat exchange and thus improved the accuracy of evapotranspiration estimation. The daily evapotranspiration, directly estimated during Landsat overpassing days under clear-sky and interpolated for other days, agreed well with the field measurements, with an R^2 of 0.78 and an RMSE of 0.95 mm day^{-1}.

Much could be improved in the parameterization of the PT coefficient when more field data are available in the future. This makes the method robust, adaptive, and relatively easy to implement for operational evapotranspiration estimation over both agricultural and natural ecosystems. Additional field observations, such as LAI measurement, dates of irrigation, flooding, draining, and harvest, and temporal field-camera images, could also help researchers to interpret the errors in remote sensing estimates, inciting ideas for model improvement. The daily evapotranspiration maps at 30m moderate resolution, from our fully automated workflow, could provide growers with spatially explicit information to tailor irrigation management at the field scale, thus improving water use efficiency. At the watershed or regional scale, it could inform the water agencies that monitor water use among various water basins and sectors and to improve water allocation and planning. The evapotranspiration estimates can also be combined with

available data on surface water delivery and applied water efficiency to estimate groundwater pumping. By further developing this model and researching its application, we can provide timely and reliable information to help growers and water use planners to implement practices and monitor progresses toward sustainable groundwater management.

Acknowledgments

We are grateful to all the field crew that collected field data, including J. Verfaillie and D. Szutu, and the California Department of Water Resources CIMIS program for providing spatial reference evapotranspiration data. We also thank Han Liu, Emily Hurry, Noah Bennett, and Abigail Neat for contributing to the workflow automation, and Dr. S. Liang and Dr. T. He for sharing their coefficients for estimating albedo using Landsat 8 data.

This project was partially funded by a consumptive use study for the Sacramento-San Joaquin Delta convened by the Office of the Delta Watermaster as part of the Sacramento-San Joaquin Delta Consumptive Water Use Project. Support for this project was also provided by NASA JPL's ECOSTRESS project.

References

Akbar, R., Gianotti, D. J. S., Salvucci, G. D., & Entekhabi, D. (2019). Mapped Hydroclimatology of Evapotranspiration and Drainage Runoff Using SMAP Brightness Temperature Observations and Precipitation Information. *Water Resources Research*, *55*(4), 3391–3413. https://doi.org/10.1029/2018WR024459

Allen, R. G., Masahiro, T., & Ricardo, T. (2007). Satellite-Based Energy Balance for Mapping Evapotranspiration with Internalized Calibration (METRIC)—Model. *Journal of Irrigation and Drainage Engineering*, *133*(4), 380–394. https://doi.org/10.1061/(ASCE)0733-9437(2007)133:4(380)

Allen, R. G., Burnett, B., Kramber, W., Huntington, J., Kjaersgaard, J., Kilic, A., et al. (2013). Automated Calibration of the METRIC-Landsat Evapotranspiration Process. *JAWRA*

Journal of the American Water Resources Association, *49*(3), 563–576. https://doi.org/10.1111/jawr.12056

Anderson, M. C., Norman, J. M., Diak, G. R., Kustas, W. P., & Mecikalski, J. R. (1997). A two-source time-integrated model for estimating surface fluxes using thermal infrared remote sensing. *Remote Sensing of Environment*, *60*(2), 195–216. https://doi.org/10.1016/S0034-4257(96)00215-5

Anderson, M. C., Norman, J. M., Mecikalski, J. R., Torn, R. D., Kustas, W. P., & Basara, J. B. (2004). A Multiscale Remote Sensing Model for Disaggregating Regional Fluxes to Micrometeorological Scales. *Journal of Hydrometeorology*, *5*(2), 343–363. https://doi.org/10.1175/1525-7541(2004)005<0343:AMRSMF>2.0.CO;2

Anderson, M. C., Allen, R. G., Morse, A., & Kustas, W. P. (2012). Use of Landsat thermal imagery in monitoring evapotranspiration and managing water resources. *Remote Sensing of Environment*, *122*, 50–65. https://doi.org/10.1016/j.rse.2011.08.025

Anderson, M. C., Gao, F., Knipper, K., Hain, C., Dulaney, W., Baldocchi, D., et al. (2018). Field-Scale Assessment of Land and Water Use Change over the California Delta Using Remote Sensing. *Remote Sensing*, *10*(6), 889. https://doi.org/10.3390/rs10060889

Baldocchi, D., Hicks, B. B., & Meyers, T. P. (1988). Measuring Biosphere-Atmosphere Exchanges of Biologically Related Gases with Micrometeorological Methods. *Ecology*, *69*(5), 1331–1340. https://doi.org/10.2307/1941631

Baldocchi, D., Falge, E., Gu, L., Olson, R., Hollinger, D., Running, S., et al. (2001). FLUXNET: A New Tool to Study the Temporal and Spatial Variability of Ecosystem-Scale Carbon Dioxide, Water Vapor, and Energy Flux Densities. *Bulletin of the American Meteorological Society*, *82*(11), 2415–2434. https://doi.org/10.1175/1520-0477(2001)082<2415:FANTTS>2.3.CO;2

Baldocchi, D., Knox, S., Dronova, I., Verfaillie, J., Oikawa, P., Sturtevant, C., et al. (2016). The impact of expanding flooded land area on the annual evaporation of rice. *Agricultural and Forest Meteorology*, *223*, 181–193. https://doi.org/10.1016/j.agrformet.2016.04.001

Baldocchi, D., Dralle, D., Jiang, C., & Ryu, Y. (2019). How Much Water Is Evaporated Across California? A Multiyear Assessment Using a Biophysical Model Forced With Satellite Remote Sensing Data. *Water Resources Research*, *55*(4), 2722–2741. https://doi.org/10.1029/2018WR023884

Bastiaanssen, W. G. M., Pelgrum, H., Wang, J., Ma, Y., Moreno, J. F., Roerink, G. J., & van der Wal, T. (1998). A remote sensing surface energy balance algorithm for land (SEBAL).: Part 2: Validation. *Journal of Hydrology*, *212–213*, 213–229. https://doi.org/10.1016/S0022-1694(98)00254-6

Burt, C. M., Mutziger, A., Howes, D., & Solomon, K. H. (2002). Evaporation from irrigated agricultural land in California. *Report No. 02-001*.

California Department of Water Resources. (2005, December). How much water has your crop used since your last irrigation? Retrieved from https://cimis.water.ca.gov/Content/pdf/Crop_Coeffients.pdf

Castellví, F., Snyder, R. L., Baldocchi, D. D., & Martínez-Cob, A. (2006). A comparison of new and existing equations for estimating sensible heat flux using surface renewal and similarity concepts. *Water Resources Research*, *42*(8).

Cawse-Nicholson, K., Fisher, J., & Wang, A. (2017, May). *ECOSTRESS Calibration and Validation*. Presented at the ECOSTRESS Science Team Meeting. Retrieved from https://ecostress.jpl.nasa.gov/downloads/science_team_meetings/2017/day2/1_ECOSTRESS_calval.pdf

Chávez, J. L., Howell, T. A., & Copeland, K. S. (2009). Evaluating eddy covariance cotton ET measurements in an advective environment with large weighing lysimeters. *Irrigation Science*, *28*(1), 35–50. https://doi.org/10.1007/s00271-009-0179-7

Clay, J., Paw U, K. T., McAuliffe, M., Schmiedeler, M., Mangan, M. R., & Lambert, J. J. (2019). Comparing In-situ Measurements of Evapotranspiration of Crop and Fallow Fields in the Sacramento-San Joaquin River Delta of California in 2018 Using Surface Renewal and Eddy Covariance Methods. *AGU Fall Meeting Abstracts*, *41*. Retrieved from http://adsabs.harvard.edu/abs/2019AGUFM.B41L2473C

Consoli, S., O'Connell, N., & Snyder, R. (2006). Estimation of evapotranspiration of different-sized navel-orange tree orchards using energy balance. *Journal of Irrigation and Drainage Engineering*, *132*(1), 2–8.

Cook, M. J. (2014, October 22). *Atmospheric Compensation for a Landsat Land Surface Temperature Product*. Rochester Institute of Technology. Retrieved from https://scholarworks.rit.edu/cgi/viewcontent.cgi?article=9669&context=theses

Couvreur, V., Kandelous, M. M., Sanden, B. L., Lampinen, B. D., & Hopmans, J. W. (2016). Downscaling transpiration rate from field to tree scale. *Agricultural and Forest Meteorology*, *221*, 71–77. https://doi.org/10.1016/j.agrformet.2016.02.008

Cuenca, R. H., Ciotti, S. P., & Hagimoto, Y. (2013). Application of Landsat to evaluate effects of irrigation forbearance. *Remote Sensing*, *5*(8), 3776–3802.

Debruin H. A. R. (1983). A Model for the Priestley-Taylor Parameter-Alpha. *Journal of Climate and Applied Meteorology*, *22*(4), 572–578.

Delta Stewardship Council. (2018). *The Delta Plan: Chapter 3 - A More Reliable Water Supply for California*. Delta Stewardship Council. Retrieved from http://deltacouncil.ca.gov/docs/delta-plan/chapter-3-more-reliable-water-supply-california-amended-april-2018

D'Errico, J. (2020). *SLM - Shape Language Modeling*. Retrieved from https://www.mathworks.com/matlabcentral/fileexchange/24443-slm-shape-language-modeling

Duarte, H. F., Dias, N. L., & Maggiotto, S. R. (2006). Assessing daytime downward longwave radiation estimates for clear and cloudy skies in Southern Brazil. *Agricultural and Forest Meteorology*, *139*(3), 171–181. https://doi.org/10.1016/j.agrformet.2006.06.008

Dwyer, J. L., Roy, D. P., Sauer, B., Jenkerson, C. B., Zhang, H. K., & Lymburner, L. (2018). Analysis Ready Data: Enabling Analysis of the Landsat Archive. *Remote Sensing*, *10*(9), 1363. https://doi.org/10.3390/rs10091363

Eichelmann, E., Hemes, K. S., Knox, S. H., Oikawa, P. Y., Chamberlain, S. D., Sturtevant, C., et al. (2018). The effect of land cover type and structure on evapotranspiration from agricultural and wetland sites in the Sacramento–San Joaquin River Delta, California. *Agricultural and Forest Meteorology*, *256–257*, 179–195. https://doi.org/10.1016/j.agrformet.2018.03.007

Eichinger, W. E., Parlange, M. B., & Stricker, H. (1996). On the Concept of Equilibrium Evaporation and the Value of the Priestley-Taylor Coefficient. *Water Resources Research*, *32*(1), 161–164. https://doi.org/10.1029/95WR02920

Falk, M., Pyles, R. D., Ustin, S. L., Paw U, K. T., Xu, L., Whiting, M. L., et al. (2013). Evaluated Crop Evapotranspiration over a Region of Irrigated Orchards with the Improved ACASA–WRF Model. *Journal of Hydrometeorology*, *15*(2), 744–758. https://doi.org/10.1175/JHM-D-12-0183.1

Fisher, J. B. (2008). *Evapotranspiration Model (PT-JPL): MATLAB for spatial arrays*. Retrieved from http://josh.yosh.org/

Fisher, J. B., Tu, K. P., & Baldocchi, D. D. (2008). Global estimates of the land–atmosphere water flux based on monthly AVHRR and ISLSCP-II data, validated at 16 FLUXNET sites. *Remote Sensing of Environment*, *112*(3), 901–919. https://doi.org/10.1016/j.rse.2007.06.025

Fisher, J. B., Melton, F., Middleton, E., Hain, C., Anderson, M., Allen, R., et al. (2017). The future of evapotranspiration: Global requirements for ecosystem functioning, carbon and climate feedbacks, agricultural management, and water resources: THE FUTURE OF EVAPOTRANSPIRATION. *Water Resources Research*, *53*(4), 2618–2626. https://doi.org/10.1002/2016WR020175

Fisher, J. B., Lee, B., Purdy, A. J., Halverson, G. H., Dohlen, M. B., Cawse-Nicholson, K., et al. (2020). ECOSTRESS: NASA's Next Generation Mission to Measure Evapotranspiration From the International Space Station. *Water Resources Research*, *56*(4), e2019WR026058. https://doi.org/10.1029/2019WR026058

Ganguly, S., Nemani, R. R., Zhang, G., Hashimoto, H., Milesi, C., Michaelis, A., et al. (2012). Generating global Leaf Area Index from Landsat: Algorithm formulation and

demonstration. *Remote Sensing of Environment*, *122*, 185–202. https://doi.org/10.1016/j.rse.2011.10.032

Gao, B. (1996). NDWI—A normalized difference water index for remote sensing of vegetation liquid water from space. *Remote Sensing of Environment*, *58*(3), 257–266. https://doi.org/10.1016/S0034-4257(96)00067-3

Hart, Q. J., Brugnach, M., Temesgen, B., Rueda, C., Ustin, S. L., & Frame, K. (2009). Daily reference evapotranspiration for California using satellite imagery and weather station measurement interpolation. *Civil Engineering and Environmental Systems*, *26*(1), 19–33. https://doi.org/10.1080/10286600802003500

He, R., Jin, Y., Kandelous, M., Zaccaria, D., Sanden, B., Snyder, R., et al. (2017). Evapotranspiration estimate over an almond orchard using landsat satellite observations. *Remote Sensing*, *9*(5), 436.

Hemes, K. S., Eichelmann, E., Chamberlain, S. D., Knox, S. H., Oikawa, P. Y., Sturtevant, C., et al. (2018). A Unique Combination of Aerodynamic and Surface Properties Contribute to Surface Cooling in Restored Wetlands of the Sacramento-San Joaquin Delta, California. *Journal of Geophysical Research: Biogeosciences*, *123*(7), 2072–2090. https://doi.org/10.1029/2018JG004494

Hemes, K. S., Chamberlain, S. D., Eichelmann, E., Anthony, T., Valach, A., Kasak, K., et al. (2019). Assessing the carbon and climate benefit of restoring degraded agricultural peat soils to managed wetlands. *Agricultural and Forest Meteorology*, *268*, 202–214. https://doi.org/10.1016/j.agrformet.2019.01.017

Ji, L., Zhang, L., Wylie, B. K., & Rover, J. (2011). On the terminology of the spectral vegetation index (NIR − SWIR)/(NIR + SWIR). *International Journal of Remote Sensing*, *32*(21), 6901–6909. https://doi.org/10.1080/01431161.2010.510811

Jiang, C., & Ryu, Y. (2016). Multi-scale evaluation of global gross primary productivity and evapotranspiration products derived from Breathing Earth System Simulator (BESS). *Remote Sensing of Environment*, *186*, 528–547. https://doi.org/10.1016/j.rse.2016.08.030

Jin, Y., Randerson, J. T., & Goulden, M. L. (2011). Continental-scale net radiation and evapotranspiration estimated using MODIS satellite observations. *Remote Sensing of Environment*, *115*(9), 2302–2319. https://doi.org/10.1016/j.rse.2011.04.031

Jin, Y., He, R., Marino, G., Whiting, M., Kent, E., Sanden, B. L., et al. (2018). Spatially variable evapotranspiration over salt affected pistachio orchards analyzed with satellite remote sensing estimates. *Agricultural and Forest Meteorology*, *262*, 178–191. https://doi.org/10.1016/j.agrformet.2018.07.004

Kljun, N., Calanca, P., Rotach, M. W., & Schmid, H. P. (2015). A simple two-dimensional parameterisation for Flux Footprint Prediction (FFP). *Geoscientific Model Development*, *8*(11), 3695–3713. https://doi.org/10.5194/gmd-8-3695-2015

Knox, S. H., Matthes, J. H., Sturtevant, C., Oikawa, P. Y., Verfaillie, J., & Baldocchi, D. (2016). Biophysical controls on interannual variability in ecosystem-scale CO2 and CH4 exchange in a California rice paddy. *Journal of Geophysical Research: Biogeosciences*, *121*(3), 978–1001. https://doi.org/10.1002/2015JG003247

Liang, S. (2001). Narrowband to broadband conversions of land surface albedo I: Algorithms. *Remote Sensing of Environment*, *76*(2), 213–238. https://doi.org/10.1016/S0034-4257(00)00205-4

MATLAB. (2018). *MATLAB and Optimization Toolbox Release 2018a*. Natick, Massachusetts, United States: The MathWorks, Inc.

Medellín-Azuara, J., Paw U, K.T., Jin, Y., Jankowski, J., Bell, A.M., Kent, E., et al. (2018). *A Comparative Study for Estimating Crop Evapotranspiration in the Sacramento-San Joaquin Delta*. Center for Watershed Sciences, University of California Davis. Retrieved from https://watershed.ucdavis.edu/project/delta-et

Melton, F. S., Johnson, L. F., Lund, C. P., Pierce, L. L., Michaelis, A. R., Hiatt, S. H., et al. (2012). Satellite Irrigation Management Support With the Terrestrial Observation and Prediction System: A Framework for Integration of Satellite and Surface Observations to Support Improvements in Agricultural Water Resource Management. *IEEE Journal of Selected Topics in Applied Earth Observations and Remote Sensing*, *5*(6), 1709–1721. https://doi.org/10.1109/JSTARS.2012.2214474

Nagler, P. L., Scott, R. L., Westenburg, C., Cleverly, J. R., Glenn, E. P., & Huete, A. R. (2005). Evapotranspiration on western U.S. rivers estimated using the Enhanced Vegetation Index from MODIS and data from eddy covariance and Bowen ratio flux towers. *Remote Sensing of Environment*, *97*(3), 337–351. https://doi.org/10.1016/j.rse.2005.05.011

Norman, J. M., Anderson, M. C., Kustas, W. P., French, A. N., Mecikalski, J., Torn, R., et al. (2003). Remote sensing of surface energy fluxes at 101-m pixel resolutions. *Water Resources Research*, *39*(8). https://doi.org/10.1029/2002WR001775

Norman, John M., & Becker, F. (1995). Terminology in thermal infrared remote sensing of natural surfaces. *Agricultural and Forest Meteorology*, *77*(3), 153–166. https://doi.org/10.1016/0168-1923(95)02259-Z

Oki, T., Valeo, C., & Heal, K. (2006). *Hydrology 2020: An Integrating Science to Meet World Water Challenges*. IAHS-AISH publication.

Paw U, K. T., & Gao, W. (1988). Applications of solutions to non-linear energy budget equations. *Agricultural and Forest Meteorology*, *43*(2), 121–145. https://doi.org/10.1016/0168-1923(88)90087-1

Paw U, K. T., Qiu, J., Su, H.-B., Watanabea, T., & Brunet, Y. (1995). Surface renewal analysis: a new method to obtain scalar fluxes. *Agricultural and Forest Meteorology*, *74*(1), 119–137. https://doi.org/10.1016/0168-1923(94)02182-J

Paw U, K. T., Baldocchi, D. D., Meyers, T. P., & Wilson, K. B. (2000). Correction Of Eddy-Covariance Measurements Incorporating Both Advective Effects And Density Fluxes. *Boundary-Layer Meteorology*, *97*(3), 487–511. https://doi.org/10.1023/A:1002786702909

Priestley, C. H. B., & Taylor, R. J. (1972). On the Assessment of Surface Heat Flux and Evaporation Using Large-Scale Parameters. *Monthly Weather Review*, *100*(2), 81–92. https://doi.org/10.1175/1520-0493(1972)100<0081:OTAOSH>2.3.CO;2

Ryu, Y., Baldocchi, D. D., Kobayashi, H., Ingen, C. van, Li, J., Black, T. A., et al. (2011). Integration of MODIS land and atmosphere products with a coupled-process model to estimate gross primary productivity and evapotranspiration from 1 km to global scales. *Global Biogeochemical Cycles*, *25*(4). https://doi.org/10.1029/2011GB004053

Shapland, T. M., Snyder, R. L., Smart, D. R., & Williams, L. E. (2012). Estimation of actual evapotranspiration in winegrape vineyards located on hillside terrain using surface renewal analysis. *Irrigation Science*, *30*(6), 471–484. https://doi.org/10.1007/s00271-012-0377-6

Snyder, R. L., & O'Connell, N. V. (2007). Crop coefficients for microsprinkler-irrigated, clean-cultivated, mature citrus in an arid climate. *Journal of Irrigation and Drainage Engineering*, *133*(1), 43–52.

Souto, C., Lagos, O., Holzapfel, E., Maskey, M. L., Wunderlich, L., Shapiro, K., et al. (2019). A Modified Surface Energy Balance to Estimate Crop Transpiration and Soil Evaporation in Micro-Irrigated Orchards. *Water*, *11*(9), 1747. https://doi.org/10.3390/w11091747

Storey, J., Lacasse, J., Smilek, R., Zeiler, T., Scaramuzza, P., Rengarajan, R., & Choate, M. (2005). Image Impact of the Landsat 7 ETM+ Scan Line Corrector Failure.

Su, Z. (2002). The Surface Energy Balance System (SEBS) for estimation of turbulent heat fluxes. *Hydrology and Earth System Sciences*, *6*(1), 85–100. https://doi.org/10.5194/hess-6-85-2002

Sustainable Groundwater Management Office. (2020). *C2VSimFG Version 1.0*. Retrieved from https://data.cnra.ca.gov/dataset/c2vsimfg-version-1-0

Swinbank, W. C. (1951). The measurement of vertical transfer of heat and water vapor by eddies in the lower atmosphere. *Journal of Meteorology*, *8*(3), 135–145. https://doi.org/10.1175/1520-0469(1951)008<0135:TMOVTO>2.0.CO;2

Tucker, C. J. (1979). Red and photographic infrared linear combinations for monitoring vegetation. *Remote Sensing of Environment*, *8*(2), 127–150. https://doi.org/10.1016/0034-4257(79)90013-0

Twine, T. E., Kustas, W. P., Norman, J. M., Cook, D. R., Houser, P. R., Meyers, T. P., et al. (2000). Correcting eddy-covariance flux underestimates over a grassland. *Agricultural*

and Forest Meteorology, *103*(3), 279–300. https://doi.org/10.1016/S0168-1923(00)00123-4

U.S. Geological Survey. (2016). *Landsat 7* (Fact Sheet).

Vinukollu, R. K., Wood, E. F., Ferguson, C. R., & Fisher, J. B. (2011). Global estimates of evapotranspiration for climate studies using multi-sensor remote sensing data: Evaluation of three process-based approaches. *Remote Sensing of Environment*, *115*(3), 801–823. https://doi.org/10.1016/j.rse.2010.11.006

Wilson, K., Goldstein, A., Falge, E., Aubinet, M., Baldocchi, D., Berbigier, P., et al. (2002). Energy balance closure at FLUXNET sites. *Agricultural and Forest Meteorology*, *113*(1), 223–243. https://doi.org/10.1016/S0168-1923(02)00109-0

Xue, J., Bali, K. M., Light, S., Hessels, T., & Kisekka, I. (2020). Evaluation of remote sensing-based evapotranspiration models against surface renewal in almonds, tomatoes and maize. *Agricultural Water Management*, *238*, 106228. https://doi.org/10.1016/j.agwat.2020.106228

Yao, Y., Liang, S., Li, X., Chen, J., Wang, K., Jia, K., et al. (2015). A satellite-based hybrid algorithm to determine the Priestley–Taylor parameter for global terrestrial latent heat flux estimation across multiple biomes. *Remote Sensing of Environment*, *165*, 216–233. https://doi.org/10.1016/j.rse.2015.05.013

Chapter 2: Multi-scale Assessment of Agricultural Consumptive Water Use in California's Central Valley

Andy. J.Y. Wong[1], Y. Jin[1], J. Medellín-Azuara[2], K. T. Paw U[1], E. R. Kent[1], J. M. Clay[1], K. S. Hemes[3], E. Eichelmann[4], D. D. Baldocchi[5]

[1] Department of Land, Air and Water Resources, University of California, Davis, CA, USA.

[2] Department of Civil and Environmental Engineering, University of California, Merced, CA, USA.

[3] Stanford Woods Institute for the Environment, Stanford University, Stanford, CA, USA.

[4] School of Biology and Environmental Science, University College Dublin, Ireland.

[5] Dept. of Environmental Sciences, Policy, & Management, University of California, Berkeley, CA, USA.

All analyses in this chapter, except the part related to the empirical Almond orchard age and NDVI based crop coefficient modeling, were submitted along with Chapter 1 to the Journal of Water Resources Research. The manuscript, titled Multi-scale Assessment of Agricultural Consumptive Water Use in California's Central Valley, is under review. The analysis regarding the Almond orchard age will be expanded with long-term evapotranspiration spatial estimates, which date from 2003 to 2016. Professor Jin will expand on the writing while Andy will assist with the data analysis. We aim to submit the manuscript in September 2021.

Abstract

Due to population growth and progress in sustainable water management, water resources availability to California's croplands is becoming more scarce. Besides, year-to-year water supplies are becoming increasingly unpredictable due to climate change. As 80% of all human use of water is diverted for farmland irrigation, spatial estimates of crop evapotranspiration with high accuracy, from the field to watershed scale, have become increasingly important for water resources management. We here provided a comprehensive assessment on patterns of annual agricultural water use over California's Central Valley, using the 30m daily evapotranspiration estimates from Landsat satellite data. When aggregated over the Valley, we estimated the average evapotranspiration of 820 mm yr^{-1} with a standard deviation of 290 mm yr^{-1} in 2014. Agricultural water use varied significantly across and within crop types, with a coefficient of variation ranging from 8% for Rice ($\bar{x}$ = 1110, σ = 85 mm yr^{-1}) to 59% for Pistachio ($\bar{x}$ = 592, σ = 352 mm yr^{-1}). Total water uses in 2016 increased by 9.6%, as compared to 2014, mostly because of land-use conversion from fallow/idle land to cropland. Analysis across 134 Groundwater Sustainability Agencies (GSAs) further showed a large variation of agricultural evapotranspiration among and within GSAs, especially for tree crops, e.g., almond evapotranspiration ranging from 339 (σ =80) mm yr^{-1} in Tracy to 1240 (σ =136) mm yr^{-1} in Tri-County Water Authority. An empirical model using NDVI and orchard age was optimized and evaluated to understand and predict the variability of evapotranspiration within and across GSAs. Trained with the 2014 data, the empirical model could respectively explain 84% and 80% of evapotranspiration across and within GSAs in 2016. Continuous monitoring and assessment of the dynamics and spatial heterogeneity of agricultural evapotranspiration provide data-driven guidance for more effective land use and water planning across scales.

1. Introduction

Evapotranspiration, also known as crop consumptive water use in agricultural lands, is often the largest yet a second-most uncertain component of the agricultural water balance in semi-arid regions (Burt et al., 2002; Fisher et al., 2017; Oki et al., 2006). Irrigation accounts for 70% of human freshwater use and supports 45% of the world's food supply production (Koech & Langat, 2018). Most irrigation water is lost to the atmosphere via evapotranspiration (California Department of Water Resources, 2020a). Information of evapotranspiration can be applied to optimized sustainable regional water allocations and farm-level irrigation management, improving water and food security in a changing climate to meet the demands of a growing population (Fisher et al., 2017).

As one of the world's most productive agricultural regions, California is the major producer of various specialty crops including half of the fruits, vegetables, and nuts grown in the United States(California Department of Food and Agriculture, 2018). A quarter of the nation's produce comes from the Central Valley alone, due to its fertile soils and extended growing season, generating $20 billion of agricultural sales in 2017 (U.S. Department of Agriculture - National Agricultural Statistics Service, 2019). More than 7 million acres (28,000 square kilometers) of the Central Valley are irrigated via the system of reservoirs and canals, accounting for about 75% of the state's irrigated lands and consuming about 23 trillion liters of water per year (Faunt, 2009). The acreage of high-value yet water-intensive tree crops, such as almonds, pistachios, and walnuts, has been expanding in recent decades, increasing water demand in the state's largest groundwater basin (Strom, 2014). Groundwater is a major source of water supply in the Central Valley, ranging from 30% during wet years to 70% during extremely dry years (Faunt et al., 2016). During the recent 2012-2016 drought, groundwater pumping was intensified,

which led to the doubling of the reduction in the valley's groundwater storage to 11 trillion liters per year from the 2007-2009 value (Xiao et al., 2017). This groundwater overdraft due to excessive pumping accounts for 13% of water sources in the San Joaquin Valley, which is the southern half of the Central Valley (Hanak et al., 2017). It caused significant land subsidence (Faunt et al., 2016), and subsequent damages to aqueducts. The damages cost the state "tens of millions of dollars" in repairs to the aqueduct in the last 40 years (Smith, 2015) and will cost even more to fix the most recent damages (CBS, 2015).

The intensifying drought and reduction in water supply during the summer-growing-season are expected to continue, due to a projected decrease in snowpack and increasing temperature in the coming decades (Cvijanovic et al., 2017). Consequences of chronic groundwater overdraft and non-point sources pollution motivated the enactment of the Sustainable Groundwater Management Act in 2014. It requires local groundwater agencies in critically over-drafted basins to achieve a sustainable water balance by 2040 (California Department of Water Resources, 2019a). Another management challenge under water scarcity is to balance the competing beneficial water uses by many stakeholders, e.g., maintaining river flows to support estuarine habitat (Escriva-Bou et al., 2019). Some potential water management alternatives to attain Sustainable Groundwater Management Act requirements include demand management. e.g., via reduced irrigated area, in addition to increasing supply via groundwater recharge. Spatial evapotranspiration estimate records could inform stakeholders on historical and present water demand. Time series of accurate evapotranspiration maps can also help water managers better understand the dynamics of groundwater pumping, improve estimates of groundwater recharge, improve regulation oversight, and evaluate the impacts of the implemented water policy (Garcia et al., 2016; Hanak, 2011). As 77% of cropland owners in

California have fields smaller than 0.4 km^2 (Macaulay & Butsic, 2017), remotely monitoring individual land owner's water use is only possible by using routine satellite observations at a relatively high spatial resolution.

In this study, our primary objective is to improve our understanding of the agricultural water use patterns in California's Central Valley, to facilitate water resources planning, in the context of the Sustainable Groundwater Management Act. The improved semi-empirical Priestley Taylor method (PT-UCD) presented in Chapter I was implemented to generate spatial estimates of crop evapotranspiration. The method was chosen for this study based on its relatively good performance and computational efficiency for large-scale applications (Medellín-Azuara, J. et al., 2018). The automated workflow for regional applications was applied to assess the spatial patterns of evapotranspiration across the Central Valley and among dominant crop types and to analyze water use changes between 2014 and 2016 water years. To provide insights for water management agencies in their efforts to prepare for droughts and implement Sustainable Groundwater Management Act, we further provided a comprehensive assessment on agricultural evapotranspiration by boundaries of Groundwater Sustainability Agencies (GSAs). An empirical model was developed to estimate annual evapotranspiration using normalized difference vegetation index (NDVI) (Tucker, 1979) and orchard age for almonds, the largest agricultural land use in the Central Valley. The simple model helped better understand the influence of orchard age on the variability of evapotranspiration among and within GSAs and could potentially be used for predicting almond crop water consumptive use.

2. Data and Methods

2.1 Study Area

We focused on the major agricultural production area, about 25 thousand km^2, in the Central Valley of California (Figure 1a). The top 8 crop types include almond, grapes, corn, rice, alfalfa, walnuts, pistachios, and tomatoes, based on the updated crop layers from the California Department of Water Resources (DWR) (California Department of Water Resources, 2020b) (Figures 2a, c, 3a). Together, these accounted for 68 and 73% of agricultural land use in 2014 and 2016, respectively. This semi-arid region has a Mediterranean climate, with mild winter and hot, dry summer. Its mean annual precipitation ranges from 51 mm yr^{-1} in the north to 13 mm yr^{-1} in the far south, and the majority of rainfall occurs from November to March. The valley is therefore highly dependent on irrigation and vulnerable to water scarcity. Its groundwater storage depleted by approximately 16 trillion liters between spring 2005 and 2010 (California Department of Water Resources, 2019a). The depletion during the recent 2012-2016 drought is expected to be much worse, since Xiao et al., (2017) estimated that the valley's groundwater storage depletion doubled to 11 trillion liters per year from the 2007-2009 value.

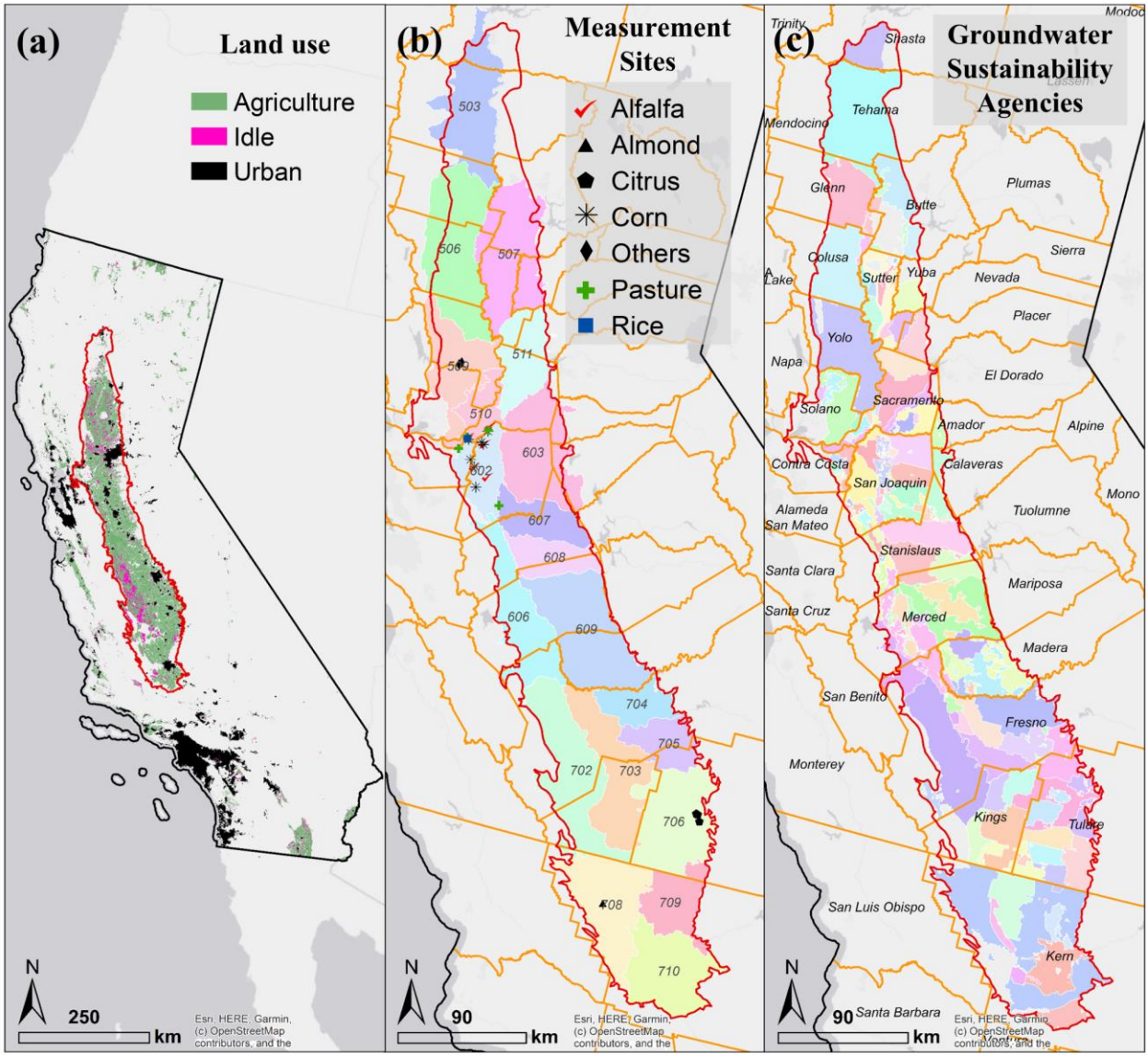

Figure 1. Study area, with locations of measurement sites from which the data were used to calibrate the PT-UCD model in Chapter I. Also shown are 2014 agricultural land use (a) over California (black line), County boundaries (orange lines), DWR water planning areas (colored base map) (b), and Groundwater Sustainability Agencies (colored base map) (c) in the Central Valley (red line).

GSAs were established under the Sustainable Groundwater Management Act to manage California's groundwater resources at the local scale. Over 260 GSAs were initially formed in

the State's high and medium priority and some are currently under reorganization and consolidation. Figure 1c shows 134 GSAs in the Central Valley that have more than 1km^2 of farmland in both 2014 and 2016. The GSAs boundaries are defined by the most recently available DWR's Exclusive GSA map (California Department of Water Resources, 2019b); GSAs boundaries were sometimes split into parts by other political boundaries, so we merged the polygon parts that share an identical GSA name, e.g. Byron-Bethany Irrigation District GSA - East Contra Costa and Byron-Bethany Irrigation District GSA – Tracy were merged into a single GSA.

2.2 Spatial Land Use and Orchard Age Data

Spatial land use data from 2014 and 2016 (California Department of Water Resources, 2020b) were prepared by Land IQ using remote sensing and machine learning techniques with extensive field survey campaigns. The crop identity and boundaries of individual agricultural fields across the entire state of California were recorded in a shapefile. The land use information in polygons is clipped by the area extent of the Central Valley and is rasterized into a 30m grid. Besides, the land use map from 2014 was used to estimate planting years of all almond orchards in the Central Valley (Chen et al., 2019). In specific, for each field polygon, a change detection algorithm was implemented to examine the long-term time series of remote sensing vegetation indices beginning in 1984 to 2014 and then identify the most recent planting event.

2.3 Spatial Evapotranspiration Estimates

The PT-UCD method optimized in Chapter 1 was applied over the whole California Central Valley to estimate crop evapotranspiration during the 2014 and 2016 water years. Satellite images from 8 tiles of the Landsat Analysis Ready Dataset were processed to estimate evapotranspiration at 30m across the Central Valley. The crop-specific actual Priestley Taylor coefficient parameterization results were used for daily averaged evapotranspiration estimation over alfalfa, almond, corn, citrus, pasture, and rice areas during Landsat overpassing days. For remaining crop types, including but not limited to grapes, walnut, pistachio, tomatoes, wheat, and cotton, where no field evapotranspiration data were available for crop-specific optimization, the generalized actual Priestley Taylor coefficient parameterizations was applied.

Remote sensing estimates of evapotranspiration on clear-sky satellite overpassing days were divided by the concurrent Spatial-CIMIS daily reference evapotranspiration (Hart et al., 2009) to derive the fraction of reference evapotranspiration (EToF). Temporal interpolation was applied to derive a complete time series of daily evapotranspiration for each Landsat pixel. For each month, an EToF pixel is interpolated only if there are at least two estimates on clear-sky overpassing days with a ±2-month moving time window; the un-interpolated pixels were gap-filled by multiplying daily reference evapotranspiration by EToF averaged by corresponding month and crop within each Landsat Analysis Ready Data tile. Daily evapotranspiration estimates were further averaged to annual time scales to analyze the regional patterns. Evapotranspiration was summarized for each crop type and compared the differences among crops by evaluating the annual evapotranspiration, reference evapotranspiration, and EToF. Specifically, the per-area water consumptive use average was computed by dividing the sum of

annual evapotranspiration by crop area over non-gap-filled pixels, while total consumptive use was computed over all crop area pixels.

2.4 Regional evapotranspiration patterns

We further summarized annual evapotranspiration by GSA boundaries (Figure 1c) to provide agricultural water use information for water planning. Specifically, the annual water use and variability were quantified for each planning area and compared across areas. We also analyzed the association of water use with the corresponding land use, Rn, actual Priestley Taylor coefficient, EToF, and reference evapotranspiration, to understand what contributed to water use differences among GSAs. While GSAs manage local groundwater resources, DWR oversees water resources regionally by water planning area. We summarized our annual crop evapotranspiration estimates by water planning areas in the Central Valley with mean and standard deviation. The mean value is further compared with DWR's estimates for the water year 2014.

2.5 Influence of orchard age on almond evapotranspiration

To better understand how orchard ages may affect a region's mean and variation in evapotranspiration, an empirical model was developed, as shown in Equation (1), using age, NDVI, and reference evapotranspiration (ETo) to estimate annual evapotranspiration.

$$ET = (a + b * (1 - e^{-((Age-c)^2/d^2)})) * (e * NDVI + f) * ET_o \quad (1)$$

We implemented the model for almond because it is the largest agricultural land and crop consumptive water user in the Central Valley. Equation (1) resembles the crop coefficient approach, where the crop coefficient here is predicted with orchard age and NDVI. To estimate

the coefficient with age, a Gaussian semivariogram fitting equation was used, which caps the maximum coefficient value as age approaches toward infinity. The equation was modified with a parameter, c, to increase the flexibility of the shape of the curve in describing the relationship between young orchards and evapotranspiration.

To compute evapotranspiration, the annual average of reference evapotranspiration was computed from the Spatial-CIMIS daily data, and the maximum NDVI value in June for each almond pixel was extracted. To optimize the parameters a through f, all evapotranspiration and model inputs at 30m resolution were summarized into median by fields. Only fields with young orchards between 3 to 12 years old in 2014 were used for optimization. The parameters are optimized with a non-linear least-square curve fitting function with the Python Scipy package. The equation, optimized with data in 2014, was evaluated with the field-summarized remote sensing evapotranspiration estimates in 2016. The four evaluation metrics include R^2, $1 - \frac{\sum_{i=1}^{n}((P_i - M_i)^2)}{\sum_{i=1}^{n}\left((M_i - \underline{M})^2\right)}$, mean absolute error where $Bias = \frac{\sum_{i=1}^{n}(|P_i - M_i|)}{n}$, RMSE, and mean absolute percentage error (MAPE), $MAPE(\%) = \frac{\sum_{i=1}^{n}\left(\frac{|P_i - M_i|}{M_i} * 100\%\right)}{n}$, where P and M are empirical Age & NDVI driven crop coefficient model estimates and remote sensing estimates respectively. Equation 1, after optimized at the field scale, was implemented to estimate annual evapotranspiration in 2014 and 2016 at a pixel level. The estimates were summarized by GSA boundaries and compared with Almond specific data summary from section 2.4.

3. Results

3.1 Evapotranspiration patterns and dynamics over the Central Valley

We estimated a total of 19.9 and 21.8 tera-liter of water consumption via evapotranspiration over the agricultural land in California's Central Valley in 2014 (24.1 thousand km^2) and 2016 water years (25.8 thousand km^2), respectively (Figures 2c, d). In the water year 2014, the top eight crop types accounted for 75% of total crop consumptive water use in the valley, including almond (22.2%), rice (10.2%), grapes (9.4%), alfalfa (9.4%), corn (8.9%), walnuts (7.3%), pistachios (4.1%), and tomatoes (3.6%) (Figures 3a, b). Overall, rice was the second largest water consumer after almonds, although it only used 7.6% of cropland, due to its highest annual evapotranspiration rate of 1109 (σ = 85) mm yr^{-1}, on a per unit area basis (Figure 3c). Pasture, walnut, almonds, citrus, and alfalfa also had relatively high evapotranspiration rates (greater than 800 mm yr^{-1}) (Figure 3c) (Table 1). In contrast, wheat consumed the least amount of water per area ($\overline{x}$ = 561, σ =228 mm yr^{-1}) among major crops, whereas pistachio, tomato, corn, cotton, and grapes had a moderate evapotranspiration rate between 600 and 800 mm yr^{-1}. As the second and third largest cropland in the valley, grapes, and corn used less total water than rice but similar water with alfalfa, walnuts, and fruits.

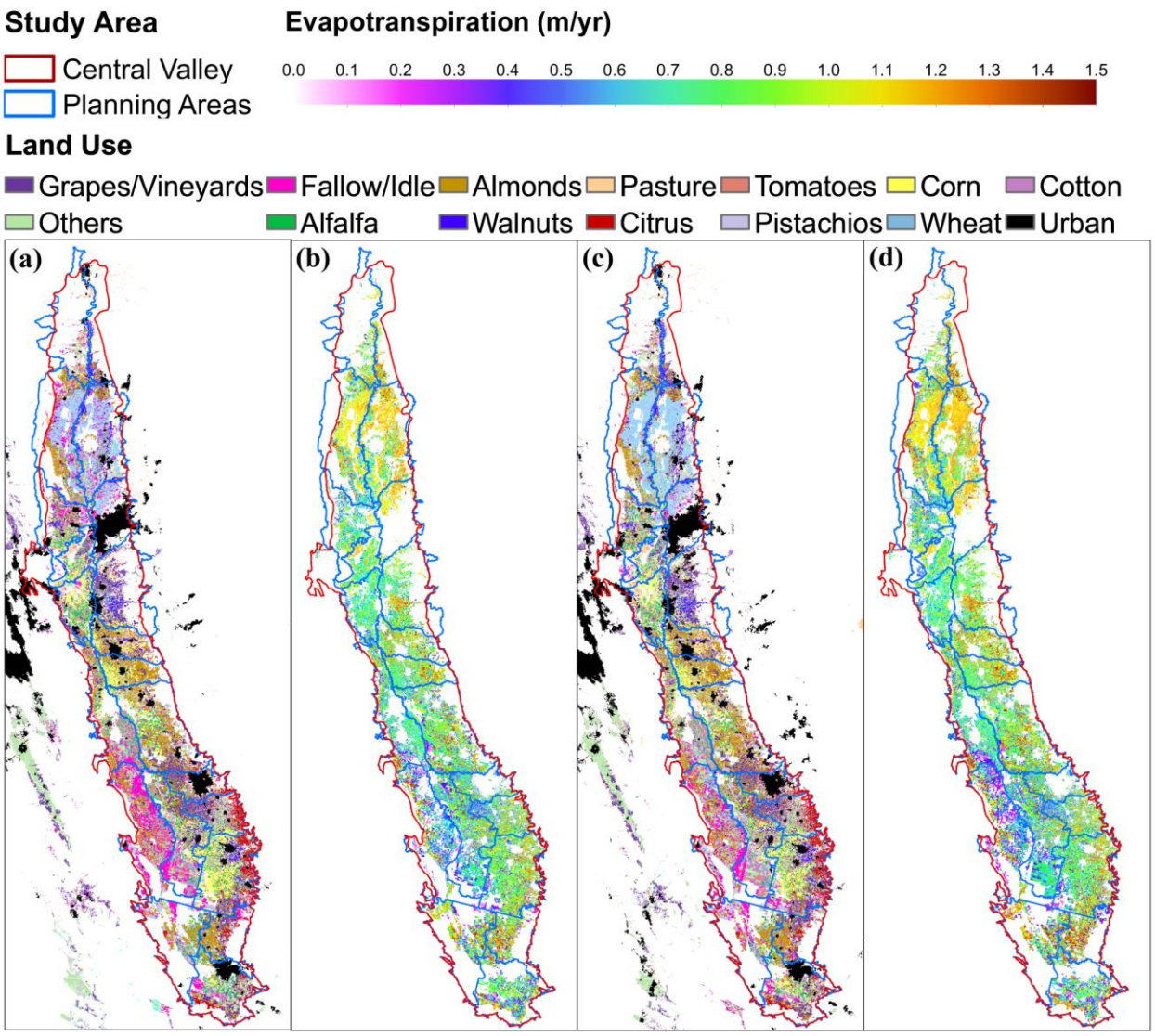

Figure 2. Spatial distributions of (a, c) land use and (b, d) annual evapotranspiration (m yr^{-1}) over the Central Valley in 2014 and 2016 water years, respectively.

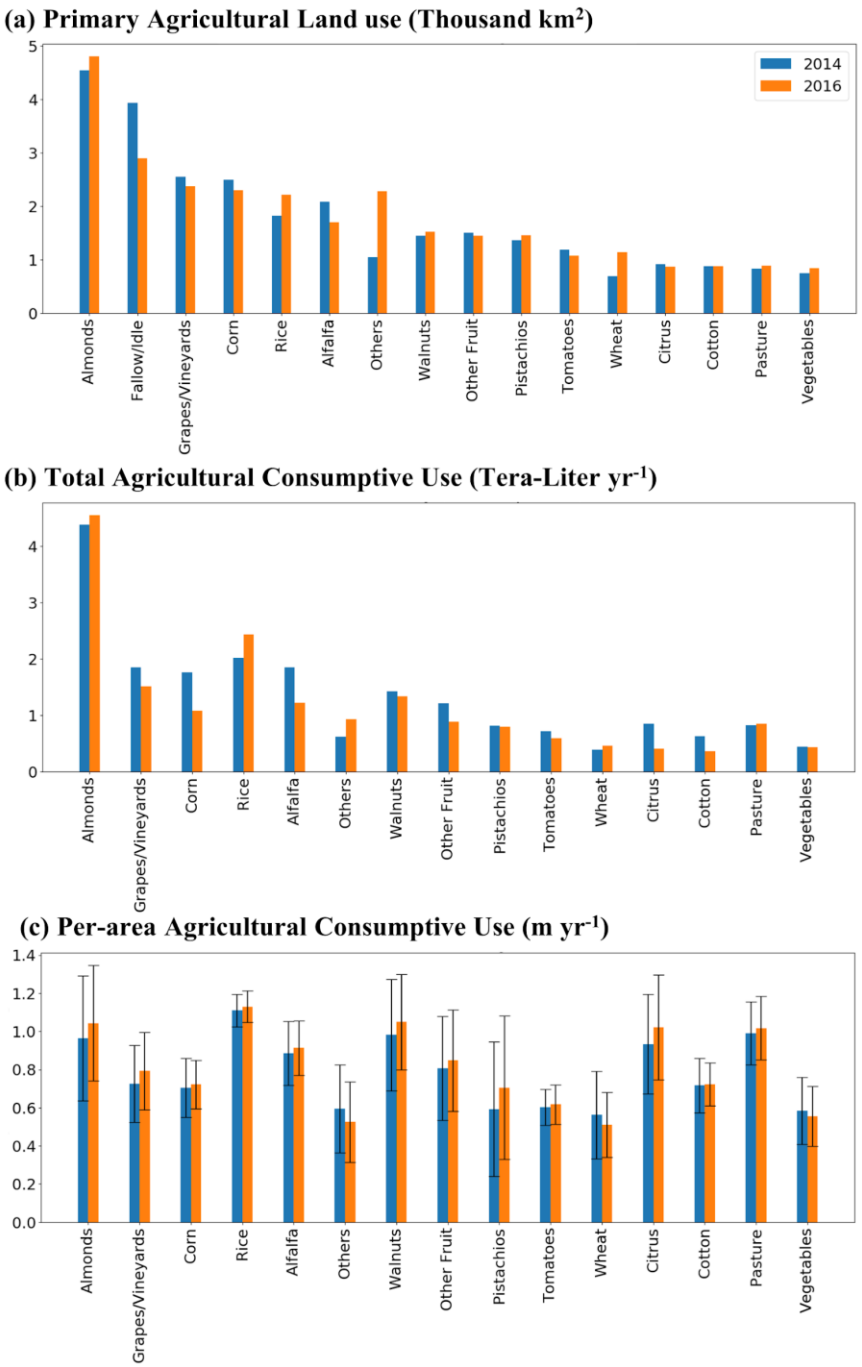

Figure 3. Primary agricultural land use (a) and agricultural consumptive water use (b,c) for each crop type in the Central Valley for 2014 and 2016 water years. The standard deviation of per-area evapotranspiration was also shown (error bars) in (c). Crops are sorted by the combined area in 2014 and 2016. Individual crops with an area less than

690 km^2 in either 2014 or 2016 were grouped into one of the following three categories, vegetables, other fruits, and others. Others include flowers, nursery, Christmas tree, miscellaneous deciduous, miscellaneous grain and hay, miscellaneous grasses, safflower, sunflowers, and young perennials.

Table 1. Statistics (Mean and standard deviation and CV) of per unit area annual evapotranspiration of major crops in the Central Valley.

Crop type	**Mean**		**Standard Deviation**		**CV**	
	(mm yr-1)		(mm yr-1)		(%)	
	WY2014	WY2016	WY2014	WY2016	WY2014	WY2016
Alfalfa	885	914	168	143	19.0	15.6
Almonds	964	1044	328	302	34.0	28.9
Citrus	933	1022	260	275	27.9	26.9
Corn	705	721	155	128	22.0	17.8
Cotton	717	722	143	113	19.9	15.6
Grapes/Vineyards	726	793	203	203	27.9	25.6
Pasture	991	1017	166	167	16.7	16.4
Pistachios	592	705	352	376	59.5	53.3
Rice	1110	1129	85	83	7.7	7.3
Tomatoes	603	617	95	103	15.7	16.7
Walnuts	981	1049	291	249	29.7	23.8
Wheat	562	510	229	171	40.7	33.5

Table 2. Statistics (Mean and standard deviation and CV) of EToF of major crops in the Central Valley.

Crop type	**Mean**		**Standard Deviation**		**CV**	
					(%)	
	WY2014	WY2016	WY2014	WY2016	WY2014	WY2016
Alfalfa	0.55	0.68	0.12	0.12	21.6	18.1
Almonds	0.59	0.75	0.2	0.21	34.0	27.7
Citrus	0.62	0.74	0.18	0.2	29.1	26.7
Corn	0.43	0.53	0.11	0.14	26.3	25.7
Cotton	0.35	0.41	0.07	0.08	20.3	18.8
Grapes/Vineyards	0.42	0.55	0.11	0.14	27.0	25.5
Pasture	0.63	0.77	0.11	0.11	17.4	14.4
Pistachios	0.33	0.47	0.19	0.24	58.6	50.4
Rice	0.62	0.69	0.06	0.08	9.1	11.0
Tomatoes	0.31	0.37	0.07	0.09	22.3	25.2
Walnuts	0.58	0.73	0.17	0.15	28.9	21.0
Wheat	0.37	0.44	0.15	0.16	39.8	36.0

Across the valley, the mean annual evapotranspiration rate varied by 35% ($\overline{x}$ = 820, σ = 290 mm yr^{-1}) over all agricultural pixels in 2014, mostly due to the diversity of the crop types. We also found high variability of evapotranspiration rate within each crop type, especially over orchards such as almond, pistachios, and walnut, with a CV higher than 20% (Table 1), most likely due to differences in planting density, age, canopy structures and stressors among orchards (Ferguson et al., 2005). For example, the almond evapotranspiration rate varied by 34% ($\overline{x}$ = 964, σ = 328 mm yr^{-1}), and the rate for pistachio varied by 59% ($\overline{x}$ = 592, σ = 352 mm yr^{-1}) in 2014. Wheat also had a very high variability (CV: 41%), different from other annual crops, which typically had a much lower variation of evapotranspiration rate than perennial crops. For all major crop categories, the difference in CV between 2014 and 2016 was less than 7.2%.

Compared to 2014, total crop consumptive water use increased by 9.6% in 2016 (Figure 3b), with an evapotranspiration rate of 856 (σ =306) mm yr^{-1}, although the reference evapotranspiration from Spatial-CIMIS decreased by 4%. This increase in evapotranspiration was mostly caused by land-use changes (Figure 3a). Total irrigated agriculture land use increased by 7.0% in 2016, partly due to a 2370 km^2 land-use conversion from fallow/idle lands in 2014 to cropland in 2016. A large portion of fallow land conversion grew rice (18%), wheat (16%), and perennial (9.7%) crops in 2016, leading to an increase of total water use by 1.3 tera-liters. Another major land-use change was the conversion from annual crops (386 km^2) to high water demand orchards, including almonds, walnuts, citrus, or grape in 2016, accounting for 1.5% of 2016 cropland and decreasing water use by 0.07 tera-liters due to the low evapotranspiration rate of young orchards.

3.2 Evapotranspiration difference among GSAs

Across a total of 134 GSAs in the valley, the annual mean per-crop-area evapotranspiration rate was averaged at 803 (σ = 154) mm yr^{-1} in the 2014 water year, and it varied significantly among GSAs, with a CV of 19% and IQR of 173 mm yr^{-1} (Figure 4a). Most GSAs with a high ET rate (>1000 mm yr^{-1}) were located in the north-eastern Central Valley, such as the Vina, Yuba Water Agency, and Southern Sutter Water District GSAs in Butte, Sutter, and Yuba counties. On the other hand, most GSAs with ET rates lower than 700 mm yr^{-1} were scattered across the south-western Central Valley, e.g. East Contra Costa Irrigation District GSA in the Contra Costa County, City of Tracy GSA, and the City of Stockton GSA in San Joaquin County, El Rico GSA in Kings county, and Pleasant Valley GSA and Westlands Water District GSA in the western part of Fresno county.

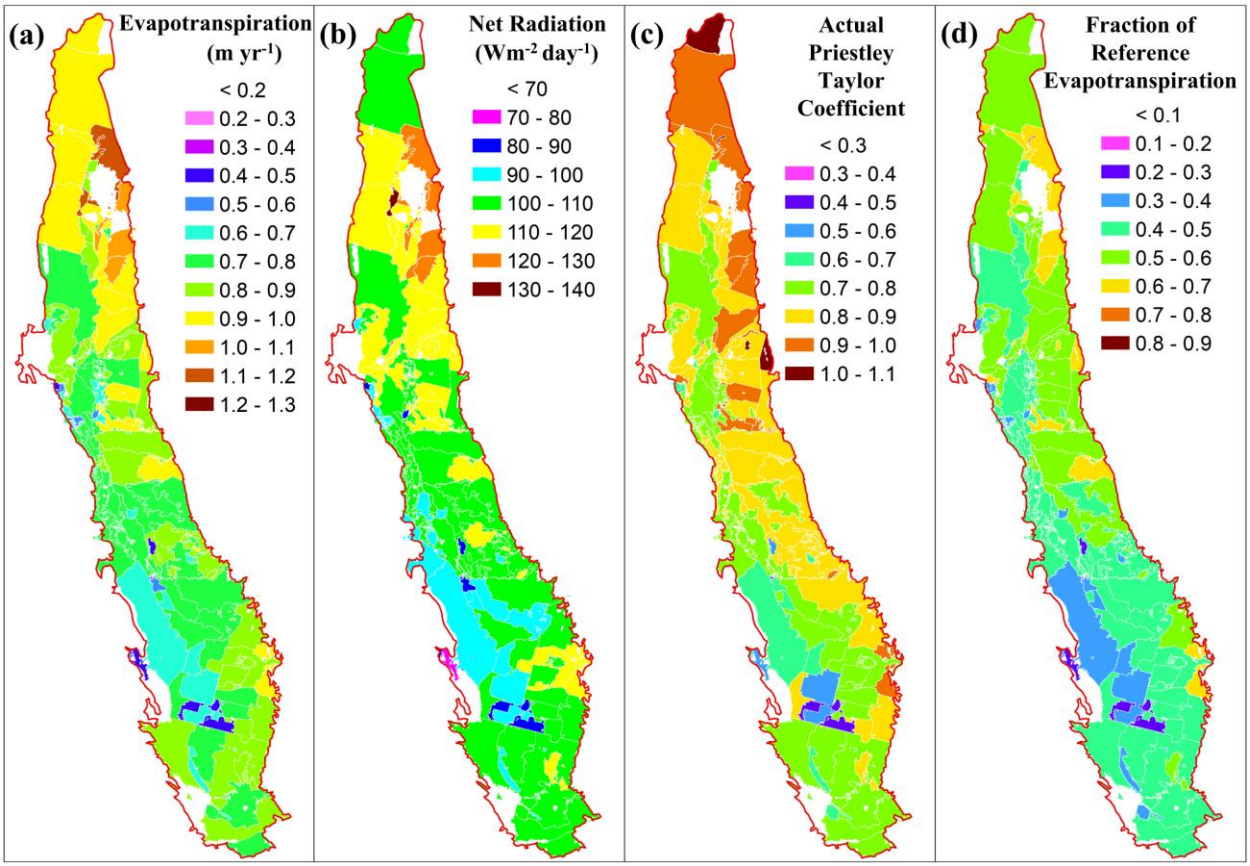

Figure 4. Spatial variation across Groundwater Sustainability Agencies in 2014 for (a) Per-area evapotranspiration rate (m yr^{-1}), (b) Net radiation ($Wm^{-2}day^{-1}$), (c) Actual Priestley Taylor coefficient, (d) EToF over all cropland averaged by GSAs.

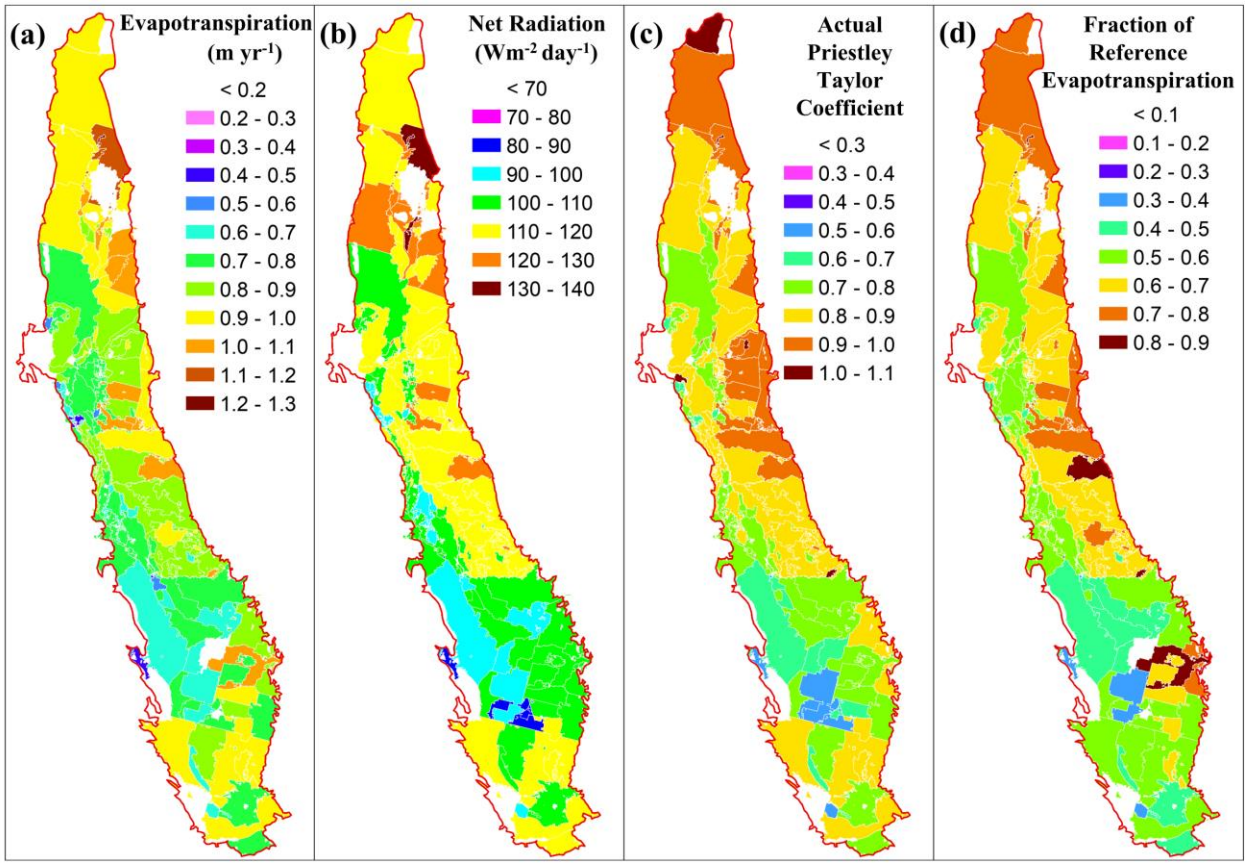

Figure 5. Spatial variation across Groundwater Sustainability Agencies in 2016 for (a) Per-area evapotranspiration rate (m yr^{-1}), (b) Net radiation ($Wm^{-2}day^{-1}$), (c) Actual Priestley Taylor coefficient, (d) EToF over all cropland averaged by GSAs.

Variability of evapotranspiration rate among GSAs was primarily driven by non-meteorological drivers. Across GSAs, we found that the evapotranspiration rate highly correlated with net radiation (r=0.92) and actual Priestley Taylor coefficient (r=0.88) (Figures 4b, c). Many

of these factors were regulated by land-use types, vegetation cover, and plant water stress status. The annual ETo ($\bar{x}$ = 1498 σ = 74 mm yr^{-1}) could only explain 4.5% of the variation in annual evapotranspiration rate among GSAs (Figure 6a). In contrast, EToF was the dominant driver of evapotranspiration rate variability among GSAs (r=0.96) (Figure 4d), mostly driven by crop types, e.g. rice with EToF of 0.61 (σ = 0.06), tomato 0.33 (σ = 0.07), almond 0.52 (σ = 0.11), and pistachio 0.37 (σ = 0.16) summarized at the GSA scale. The observed correlations for 2014 are similar to 2016 (Figure 5).

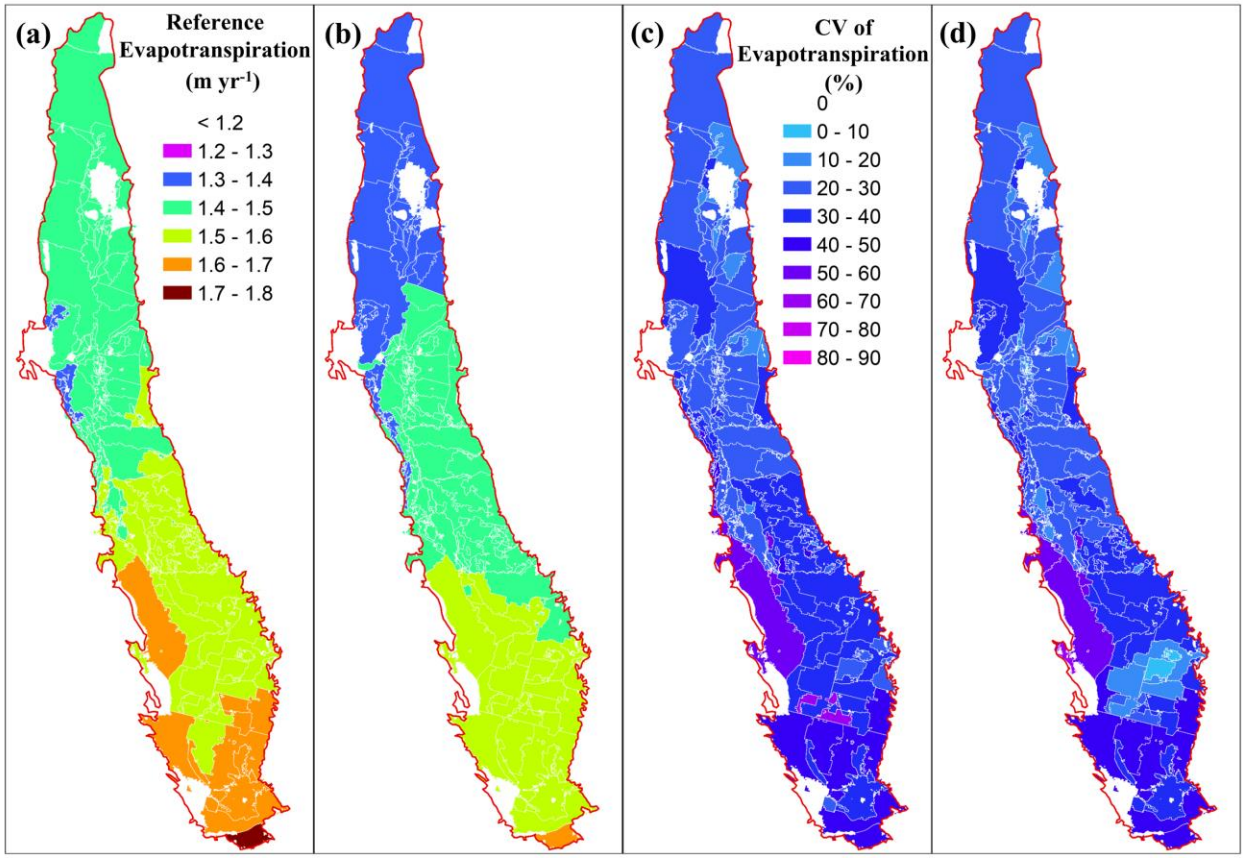

Figure 6. Reference evapotranspiration (m $year^{-1}$) in 2014 (a) and 2016 (b) over all cropland averaged by GSAs. CV (%) of per-crop-area evapotranspiration rate in 2014 (a) and 2016 (b) by GSAs.

Even for the same crop type, EToF varied significantly among GSAs for some tree crops and wheat 0.36 ($\sigma = 0.09$). The average almond EToF (Figure 7c), for example, ranged from 0.25 in the City of Tracy GSA in Tracy county to 0.75 in Rock Creek Reclamation District GSA in Chico county. Pistachio's EToF was much lower in the majority of the western San Joaquin Valley areas (Figure 7d), probably due to the plant stress caused by salinity (Hanak et al., 2017; Jin et al., 2018; Letey, 2000). Citrus EToF ($\overline{x} = 0.57$, $\sigma = 0.11$) had an IQR of 0.16 at the GSA scale. In contrast, the mean EToF showed much smaller variation among GSAs for the majority of annual crops such as alfalfa 0.54 ($\sigma = 0.08$) (Figure 12a), rice 0.61 ($\sigma = 0.06$) (Figure 7b), pasture 0.57 ($\sigma = 0.09$), and cotton 0.35 ($\sigma = 0.05$). Similar observations can be found in 2014 with figure 8.

Within each GSAs, the annual EToF also showed large spatial variation, with a mean CV of 31% ($\sigma = 12\%$) across all agricultural fields; Some GSAs with a lower evapotranspiration rate had the highest variability (Figures 6c, 4a), mostly located at and around the Westlands Water District region in the western-Fresno and Kings county. In addition to crop diversity within each GSA, significant variation of EToF was also found for each tree crop type, such as almonds and pistachios (Figures 7g, h), with IQRs of CVs among GSAs greater than 15%. For examples, the CVs of pistachio EToF within each GSAs had a mean of 34% ($\sigma = 20\%$) and an IQR of 33% across GSAs, with the largest within-GSA variation found in the Central Delta-Mendota GSA; In the Southeast Kings GSA, CV of Pistachio EToF is 29%, much lower than its neighbor, Tri-County Water Authority GSA (64%). Other types with highly variable EToF (CV of 18+% with $\sigma = 10+\%$) included almond, citrus, walnut, and wheat. In contrast, EToF was more

homogeneous within GSA for alfalfa with a mean CV of 17% (σ = 7%) and IQR of 6% (Figure 7e), and rice (Figure 7f).

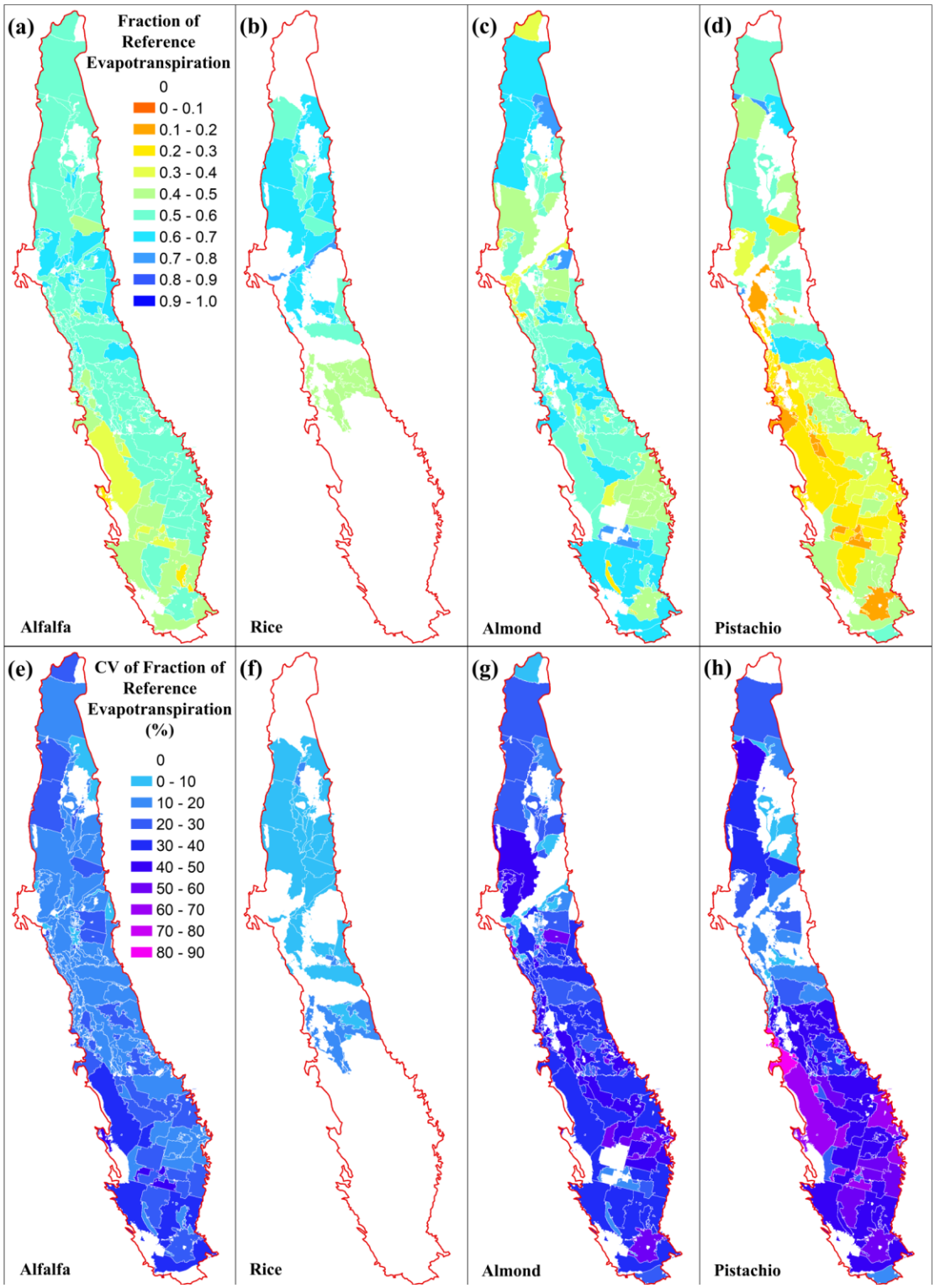

Figure 7. Mean (Top) and CV of the fraction of reference evapotranspiration by GSAs in 2014 for alfalfa (a, e), rice (b, f), almond (c, g), and pistachio (d, h).

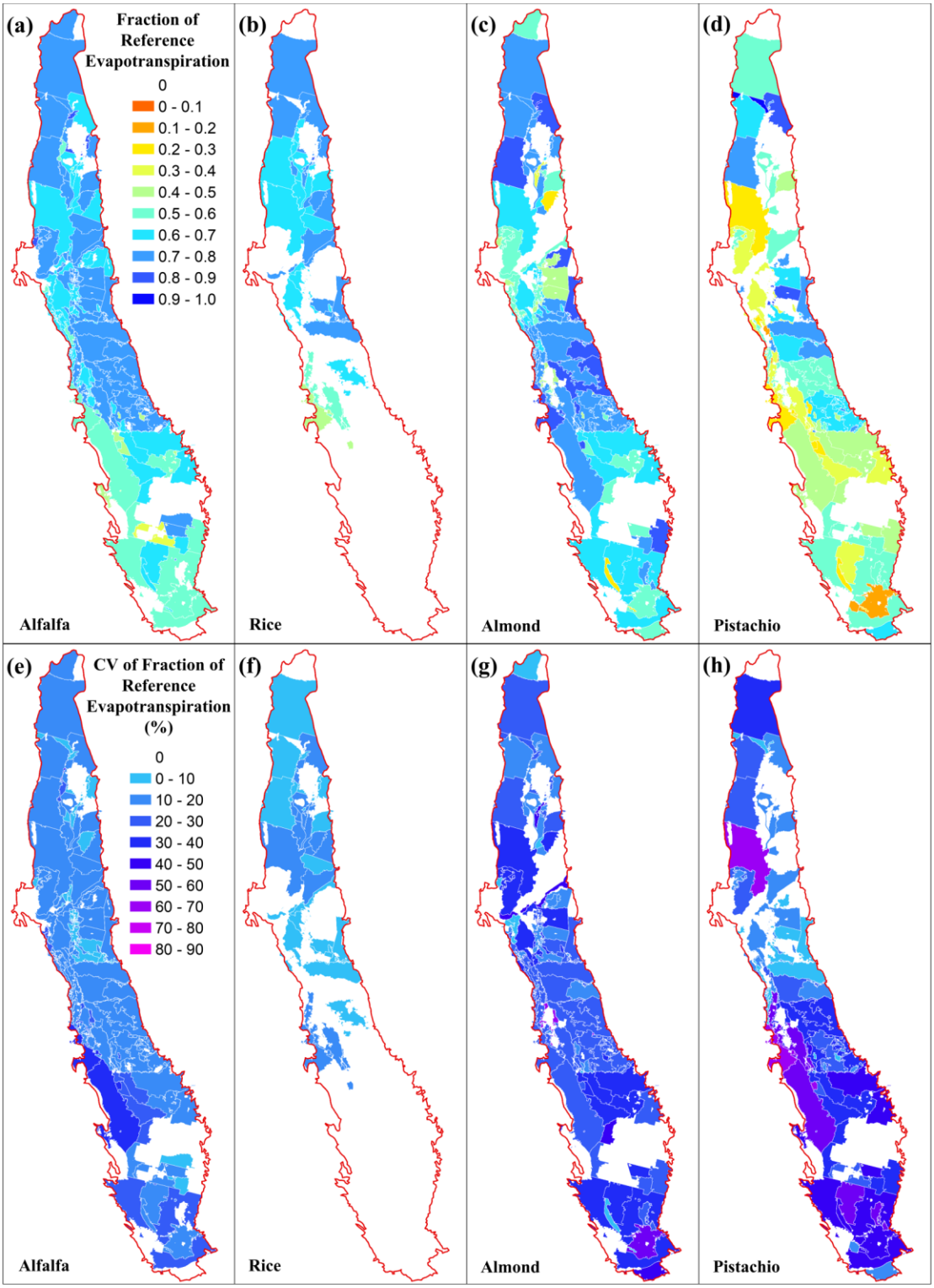

Figure 8. Mean (Top) and CV of the fraction of reference evapotranspiration by GSAs in 2016 for alfalfa (a, e), rice (b, f), almond (c, g), and pistachio (d, h).

About 39 GSAs had more than 60% of agricultural land areas planted with perennial crops including almond, pistachio, citrus, walnut, and grape in 2014, which accounted for 76% of total agricultural water use by these GSAs and 27% of Central Valley's total agricultural water use in 2014 (Figure 7b). These GSAs will likely face greater vulnerability to prolonged drought due to the high cost of fallowing productive orchards. When dividing the total consumptive use of perennial crops by the GSA area (Figure 7c), we found that some small and medium-size GSAs, such as Delano-Earlimart Irrigation District GSA, Madera Water District GSA, and New Stone Water District GSA, will need to reserve a much greater depth (400 mm yr^{-1}) of groundwater storage to maintain the orchards during drought.

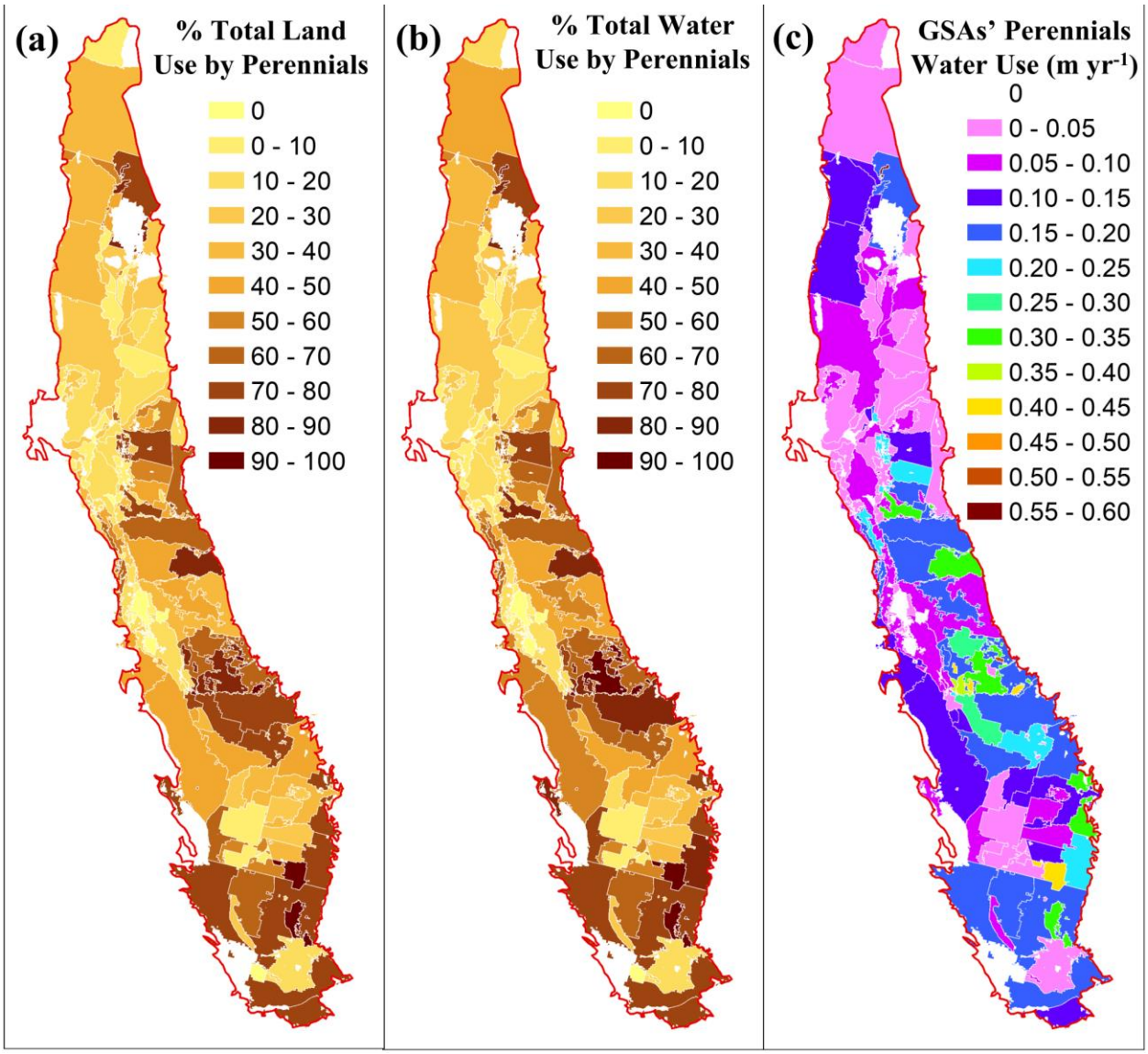

Figure 9. Percent of cropland (a) and total water consumptive use (a) in 2014 by major perennial crops (Almond, Pistachio, Citrus, Walnut, and Grape) in GSAs, and their total water consumptive use normalized by GSA area size (c).

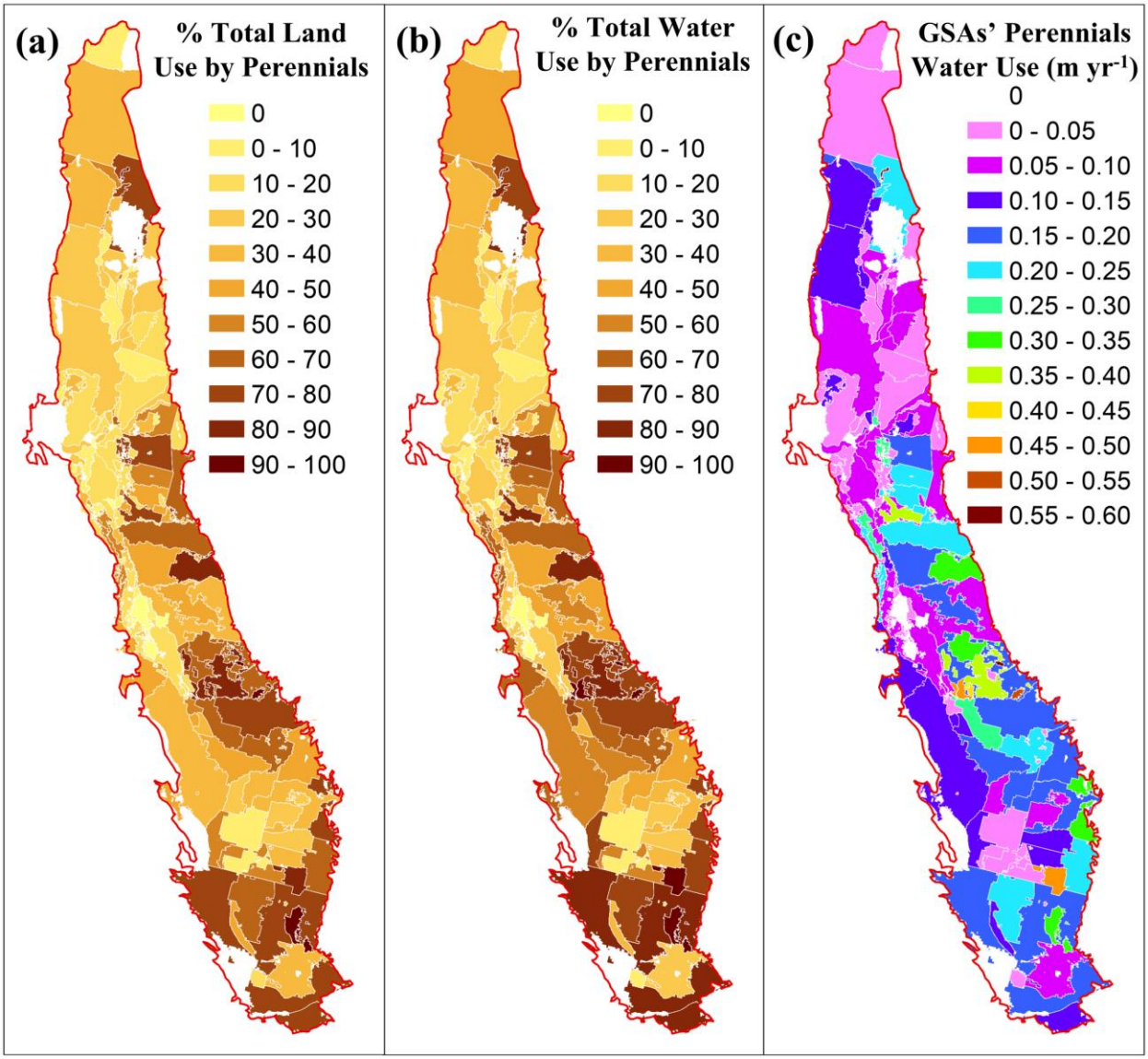

Figure 10. Percent of cropland (a) and total water consumptive use (a) in 2016 by major perennial crops (Almond, Pistachio, Citrus, Walnut, and Grape) in GSAs, and their total water consumptive use normalized by GSA area size (c).

3.3 Almond Evapotranspiration in Relation With Orchard Age and NDVI

A pattern of increasing evapotranspiration can be observed among orchards younger than 10 years old (Figure 11). For older orchards, the median of annual field-scale evapotranspiration

estimates by remote sensing, as shown in the box plots, fluctuates around 3 mm day^{-1}. Comparing between the water years 2014 and 2016, almond's evapotranspiration across the central valley is generally higher in 2016 (Figure 11a). Across the three basins (Figure 11b), we observed some differences in the pattern of evapotranspiration. In the Sacramento River Basin, younger orchards have higher evapotranspiration than the other two basins in the southern Central Valley. However, after age 12, evapotranspiration in the Sacramento River Basin is often lower than the other two basins. Between the two basins in the southern Central Valley, evapotranspiration is generally higher in Tulare than in the San Joaquin River Basin. The box further shows that the interquartile range of evapotranspiration is generally less than 1mm day^{-1}. However, some outliers could not be explained, and significant variability in evapotranspiration could be explained by orchard age.

NDVI, on the other hand, could well describe the variability of evapotranspiration (Figure 12). However, we did not observe a significant difference in the relationship between evapotranspiration and NDVI, among Basins and water years. An exception was the best fit line in 2914 for the Sacramento River Basin (Figure 12a). The slope was found to be lower, while the intercept to be higher than the other basins. This is consistent with the previous observations regarding orchard age and evapotranspiration in the Sacramento River Basin.

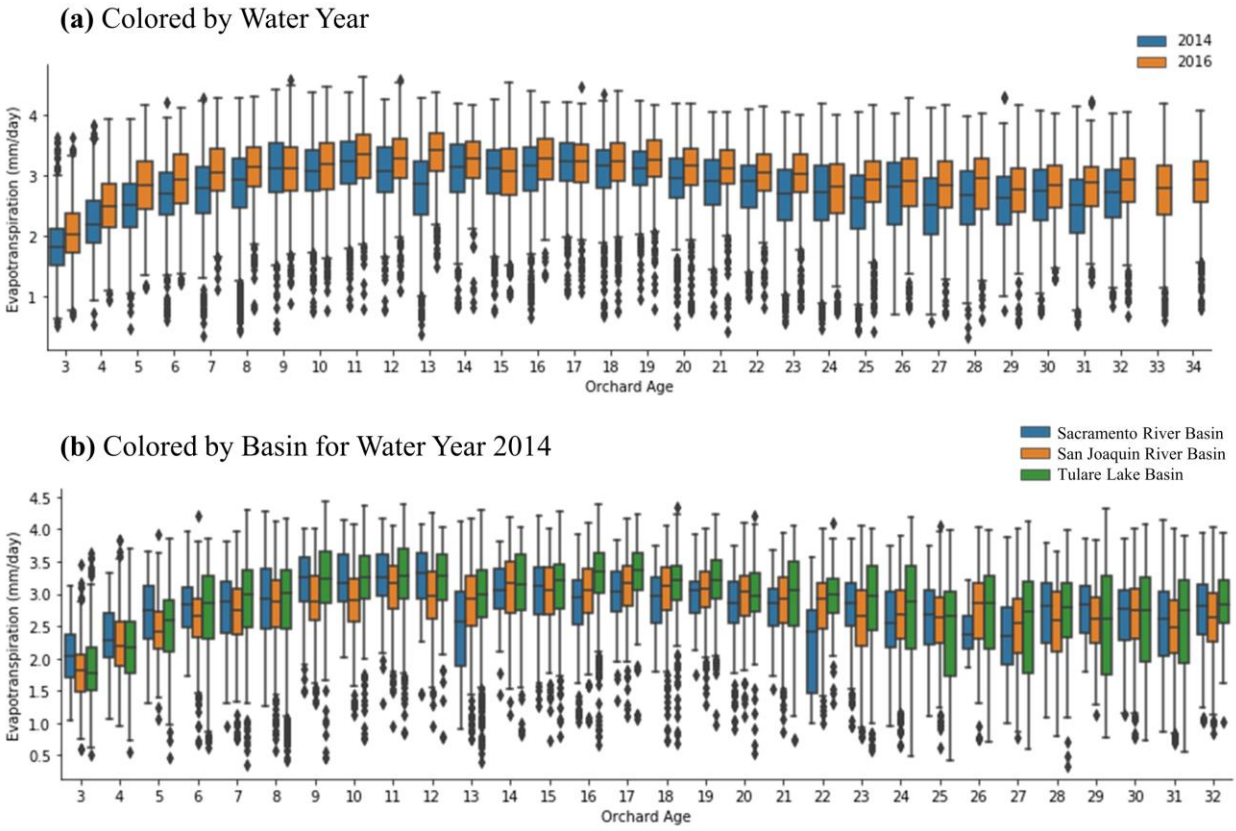

Figure 11. Box plots of field median evapotranspiration. The summarized evapotranspiration across the Central Valley by water year in (a) and the 2014 evapotranspiration in by the three basins of the Valley in (b). The box plot shows the quartiles of the dataset. The upper whisker is extended to the last datum less than the sum of the 1.5 times of interquartile range and the 3rd quartile. Similarly, the lower whisker is extended to the first datum greater than the first quartile subtracted by the 1.5 times of interquartile range.

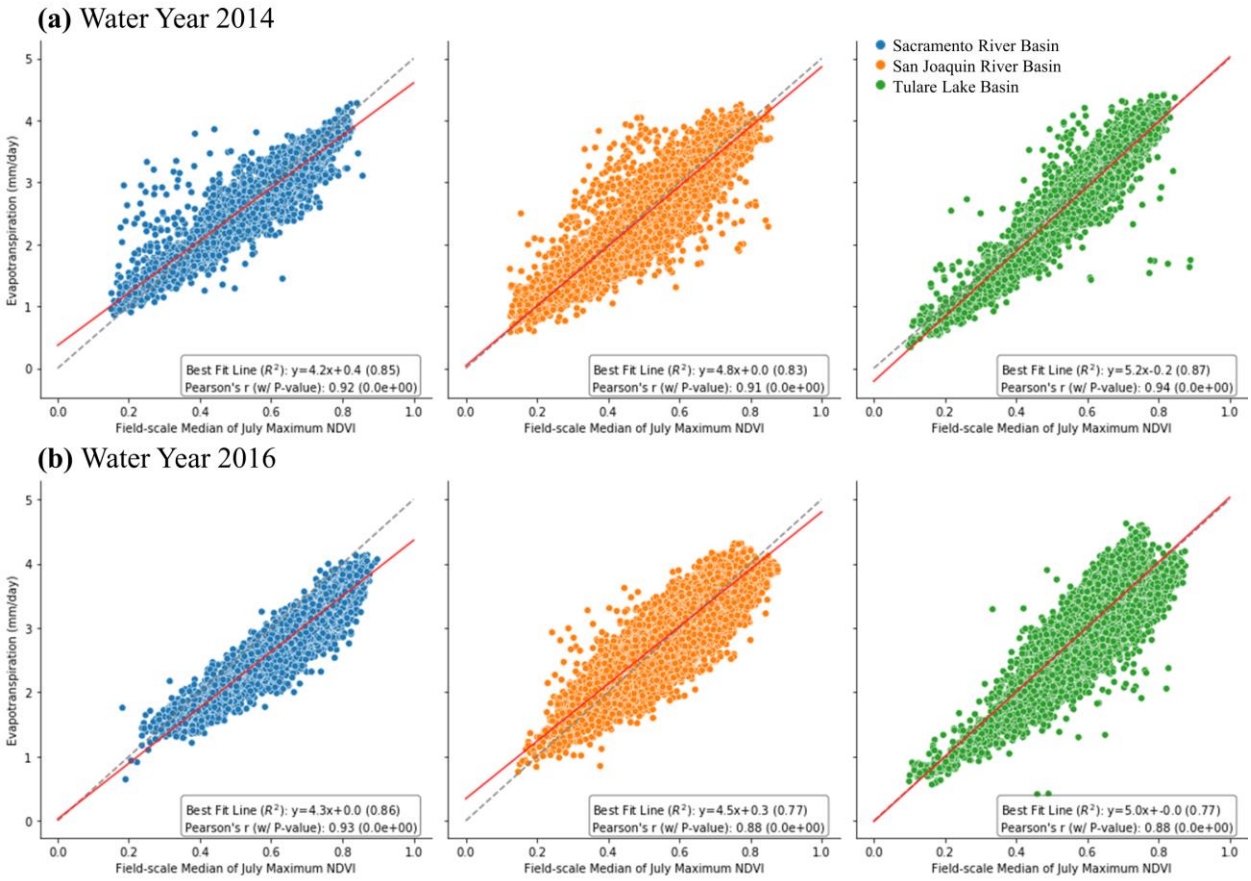

Figure 12. Scatter plots of NDVI and evapotranspiration. The water year 2014 data were shown on top and the 2016 data on the bottom. The dots are colored by basins of the Central Valley. The best line for each plot was also shown.

Using both orchard age and NDVI together could effectively estimate annual evapotranspiration in both 2014 and 2016. The empirical equation (2) was generated by optimizing equation (1) with the 2014 dataset over orchards that are younger than 12 years old.

$$ET = (-0.66 + 1.36 * (1 - e^{-((Age+9.99)^2/61.89)})) * (1.57 * NDVI + 0.07) * ET_o \quad (2)$$

The empirical model explained at least 71% of the variability of evapotranspiration across orchards of all ages (Figure 13), with an RMSE, MAE, and MAPE of less than 0.34 mm day^{-1},

0.28 mm day^{-1}, and 9.71%, respectively. The model has a similar performance between young and old orchards. For orchards between 2 and 12 years old, the R^2 was greater than 0.73, and RMSE, MAE, and MAPE were less than 0.33 mm day^{-1}, 0.28 mm day^{-1}, and 9.71%, respectively. As for orchards older than 12 years old, the R^2 was greater than 0.68, and RMSE, MAE, and MAPE were less than 0.34 mm day^{-1}, 0.28 mm day^{-1}, and 9.70%, respectively.

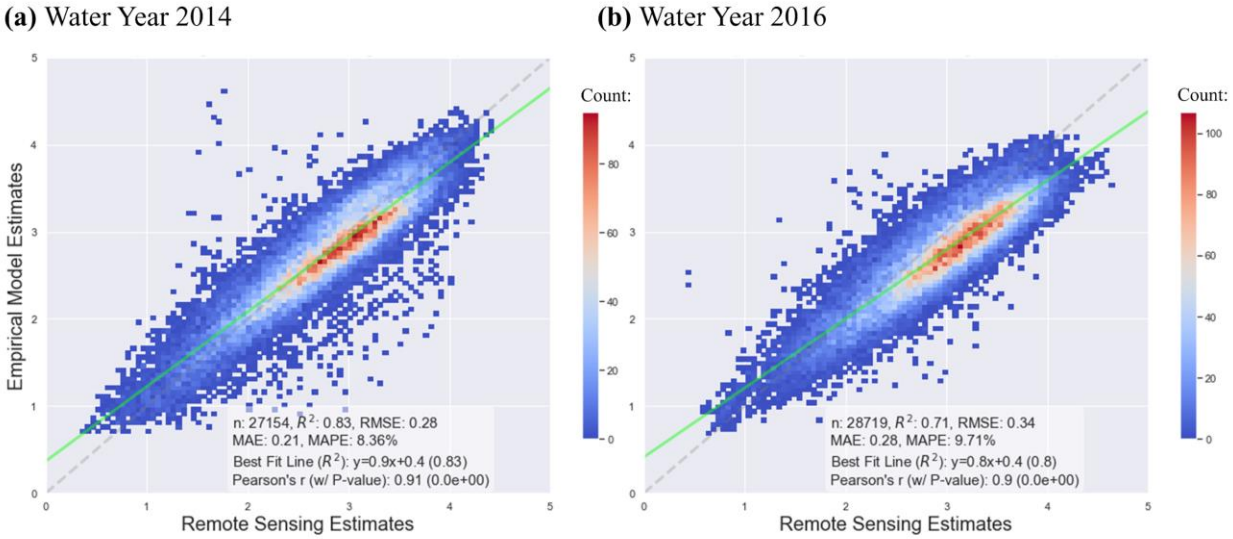

Figure 13. 2D-Density plot comparing the fields-median of remote sensing evapotranspiration estimates with empirically estimated evapotranspiration. Comparison with the dataset for 2014 and 2016 was shown separately in (a) and (b).

The empirical model, when implemented at a pixel level and aggregated by GSAs, agreed well with the summarized statistics from section 3.2. The model, trained with young orchard data in 2014, could explain 84% of the variance in mean evapotranspiration of 2016 across GSAs, with an RMSE, MAE, and MAPE of 0.21 mm day^{-1}, 0.17 mm day^{-1}, and 6.9%, respectively (Figure 14a). It could also explain 80% of the variance across GSAs in terms of the standard deviation of evapotranspiration within individual GSAs, with an RMSE, MAE, and MAPE of 0.1

mm day^{-1}, 0.08 mm day^{-1}, and 19.78%, respectively (Figure 14b). The summary statistics based on the remote sensing and empirical models are highly correlated with Pearson's r-value of at least 0.92 and a P-value less than 7.3E-38. The error in estimating mean and standard deviation is propagated to the estimation of CV. Our 2016 empirical estimates could only explain 70% of the variance, with an RMSE, MAE, and MAPE of 3.82%, 3.15%, and 19.5%, respectively.

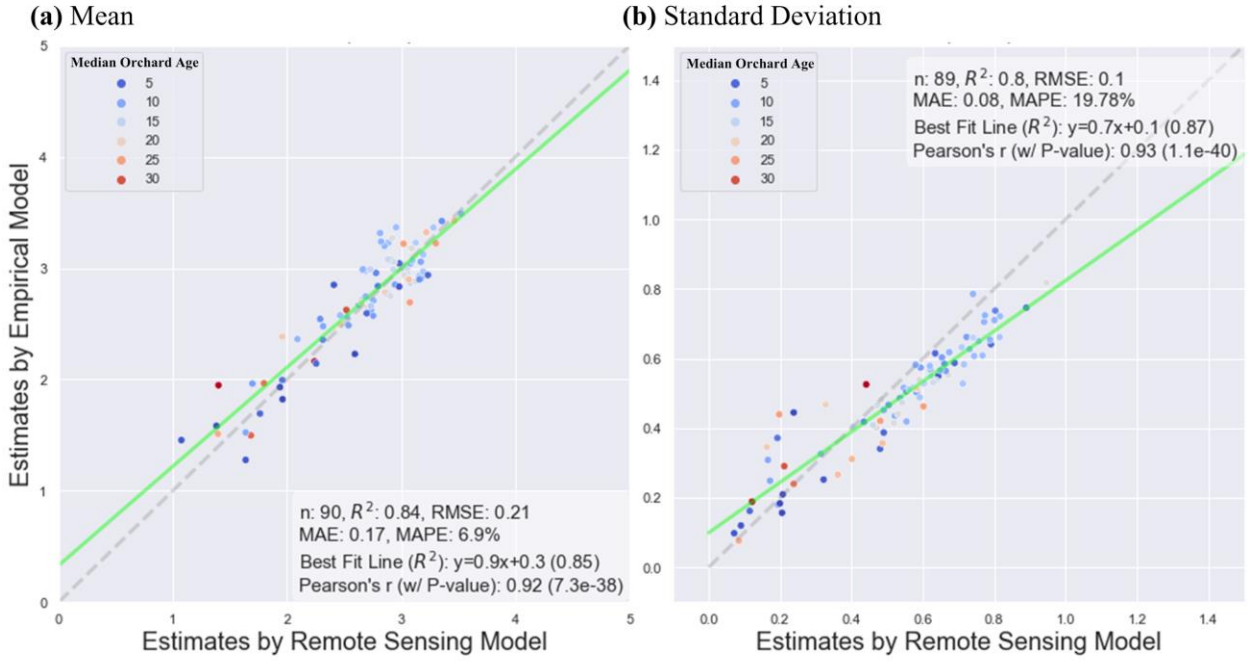

Figure 14. Scatter plots, comparing GSAs-scale statistics based on the 2016 estimates by remote sensing model vs empirical model. The mean and standard deviation were compared in (a) and (b), respectively. The dots were colored by the median orchard age for each GSA.

To our surprise, the agreement in the estimated mean across GSAs was less in the training year 2014 than the prediction year 2016. For 2014, the empirical model could explain only 58% of the

variance in mean evapotranspiration across GSAs, with an increase in RMSE, MAE, and MAPE of 0.37 mm day^{-1}, 0.23 mm day^{-1}, and 11.36%, respectively (Figure 15a). The increase is primarily caused by an outlier, at the County of Glenn GSA in the northern Central Valley, where the empirical estimates are nearly 2mm day^{-1} higher than remote sensing estimates. The GSA had less than 0.07 km^2 of orchards all at the age of 15 in 2014. In terms of standard deviation, it also captured 80% of the variance in 2014 across GSAs, with a slight improvement in RMSE, MAE, and MAPE of 0.09 mm day^{-1}, 0.07 mm day^{-1}, and 15.99%, respectively (Figure 15b).

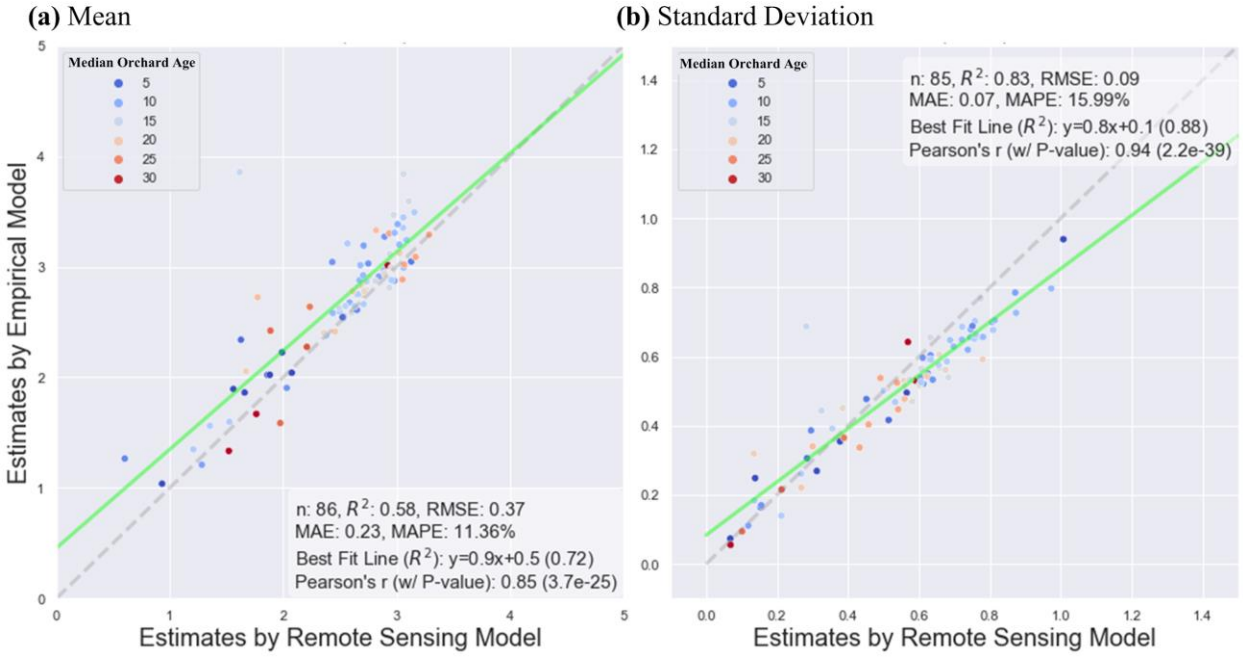

Figure 15. Scatter plots, comparing GSAs-scale statistics based on the 2014 estimates by remote sensing model vs empirical model. The mean and standard deviation were compared in (a) and (b), respectively. The dots were colored by the median orchard age for each GSA.

4. Discussion

4.1 Regional evapotranspiration estimates

At a regional scale, the annual mean values of per-area water use of major crop types in the Central Valley (Table 1) estimated here are generally within the ranges reported in the literature (Burt et al., 2002; California Department of Water Resources, 2019a; Schauer & Senay, 2019). For example, DWR's water portfolio and balances dataset, as part of DWR's 2018 Water Plan, reports that water requirement by corn ranges from 390-835 mm yr^{-1} in 2014 across sub-regions (Detailed Analysis Units by County) of all planning areas in the Central Valley (California Department of Water Resources, 2019a). Burt et al., (2002) estimated that corn in the Central Valley conventionally used 813 mm yr^{-1} in a typical precipitation year. Our regional average of corn evapotranspiration (705 mm yr^{-1}) was 16% more than DWR's average corn water requirement over planning areas (604 mm yr^{-1}). Larger differences were found for alfalfa, pasture, wheat, almonds, pistachio, and vineyard, for which our regional averages were 30-65% lower or higher than DWR's values. Over all the 30m pixels of agricultural lands in Central Valley (~25 thousand km^2), the average annual evapotranspiration rate, estimated here, is higher than the estimates over the whole Central Valley (~47 thousand km^2) by the BESS biophysical process-based model forced with 1km satellite observations (Baldocchi et al., 2019). The discrepancy is likely due to the scale effect (Wu & Li, 2009) and differences in land cover maps. Larger pixels likely contain other land use areas such as fallow, urban, water, and natural vegetation. Nonetheless, our estimates in 2014 align with the values reported in Schauer & Senay, (2019) based on the SSEBop remote sensing evapotranspiration model driven by Landsat thermal data.

We found some differences between DWR's crop coefficient model and our regional estimates, but we could not conclude which estimate is more reliable. Based on findings reported by Medellín-Azuara, et al., (2018), it would appear that our estimate would be more reliable than DWR's estimate at a field scale. They found that DWR's monthly estimates of corn, alfalfa, and pasture's estimate differ significantly from field measurements in the Sacramento San-Joaquin Delta, while the estimates by the early prototype of PT-UCD did not. However, more evapotranspiration measurement data across major crop types and in different parts of the Valley are needed to evaluate the uncertainty of crop coefficient and our estimate. Furthermore, if a model has a high error in estimating evapotranspiration at a field scale over selected fields, the results only show that the model could not account for spatial variability of evapotranspiration at the field scale. When such a model is aggregated at the regional scale, its estimate might agree with the actual regional measurements.

Our estimation of 19.6 tera-liter water consumption in 2014 was equivalent to 74% of DWR's estimate (26.2 tera-liter) over all planning areas within the Central Valley, which was derived from CalSIMETAW (Orang et al., 2013). Among the planning areas, the discrepancies ranged from - 53.4 to -18.5%, with the most significant disagreement (<-50%) occurring in the southern and center-east of the San Joaquin Valley (planning areas 704, 708, 709 in Figure 1b). Similarly, previous studies in the Sacramento San Joaquin Delta, a subset of the Central Valley, showed that remote sensing estimates are lower than CALSIMETAW's estimates by 6 to 24% (Medellín-Azuara, et al., 2018; Paul et al., 2017). Over this Delta area, our crop-specific Priestley Taylor method in this study estimated 1.20 tera-liter in 2016, very similar to the DISALEXI's estimate of 1.16 tera-liter in the water year 2016; both were about 80% of

CalSIMETAW's estimates of 1.49 tera-liters, based on the published data summary table in Medellín-Azuara, et al., (2018).

Two factors may have caused the discrepancy in regional estimates between PT-UCD and CalSIMETAW. First, CalSIMETAW's crop coefficient approach implemented at a regional scale may overestimate actual evapotranspiration, because it didn't account for the impacts of planting variabilities such as orchard age distribution and planting density, field conditions such as salinity and disease, and crop management like deficit irrigation. Secondly, the land-use map used by CALSIMETAW was different from the DWR's land use map that we used here. For example, CALSIMETAW estimated 13.7, 23.9, and 23.9 km^2 of corn, alfalfa, and pasture in PA 704 in 2014, in contrast to our DWR's map-based estimates of 18.2, 21.4, and 9.3 km^2 of corn, alfalfa, and pasture.

4.2 Explanation of variability of almond evapotranspiration within and among GSAs.

The optimization and evaluation of the empirical Age and NDVI based crop coefficient model provides insight into the variation of almond evapotranspiration within and among GSAs (Figure 7 c,g, and 8 c,g). Our study demonstrates that the growth of immature orchards is associated with the increases in crop water use at a field scale. When using both age and NDVI information, the empirical model could explain a large portion of spatial variation within each GSA and among GSAs. Further experimentation reveals that age alone is adequate in estimating the variability of evapotranspiration among GSAs since the comparison of mean evapotranspiration has a MAPE of 18.59%. However, it could not be used to estimate the variability within GSA, since the comparison of standard deviation in evapotranspiration has a MAPE of 67.81%. The results suggest that although NDVI is associated with orchard age, there

are other important factors, such as salinity and farm management, that could both affect NDVI and explain the variability of evapotranspiration within and among GSAs.

4.2 Implications for water resource management

Currently, California's Groundwater Sustainability Agencies (GSAs) use various approaches to estimate evapotranspiration in their water budget accounting and management plan development, causing inconsistency among GSAs. For example, the Olcese GSA estimates monthly evapotranspiration from 1993 to 2015 using the METRIC prepared by the Irrigation Training & Research Center; North Kings GSA uses DWR's crop coefficient to estimate annual evapotranspiration rate over detailed analysis units from 1998 to 2010, while the Delano and Yuba GSAs use crop coefficients published by the Irrigation Training & Research Center in 2003 and derived from SEBAL's evapotranspiration map in 2009, respectively. Our study shows that the fractional of reference ET (EToF), or similarly crop coefficients, for most crops, varies spatially across and even within GSAs, and for some crops, EToF changes considerably between years. More consistent estimates with known uncertainty from a calibrated or thoroughly evaluated approach are needed to ensure consistent quantitative information for data-driven decisions for water planning. Our optimized Priestley Taylor approach driven by remote sensing observations provides an efficient way to capture both spatial heterogeneity and temporal dynamics of water balance. However, remote sensing observations should be verified with locally available field measurements, before being implemented spatially to inform management decisions.

In particular, we found that orchards and wheat generally had a greater spatial variability of evapotranspiration and crop coefficients than other major crop types, across the Central Valley

(Table 1 & 2), within and among GSAs. Age distribution and other stressors such as salinity likely contributed to evapotranspiration variability for tree crops (Jin et al., 2018; UC-ANR, 2008, 2018). Among three major nut tree crops, pistachio had the lowest mean annual evapotranspiration rate ($\bar{x}$ = 592, σ = 352 mm yr^{-1} in 2014), followed by walnut ($\bar{x}$ = 981, σ = 291 mm yr^{-1} in 2014) and almond ($\bar{x}$ = 964, σ = 328 mm yr^{-1} in 2014). Coincidentally, 26% of pistachio acreages in 2014, 18% of walnut in 2015, and 15% of almond in 2014 across California were non-bearing orchards (Administrative Committee for Pistachios, 2020; California Department of Food and Agriculture, 2020; U.S. Department of Agriculture, 2020). The high variability of wheat water use is likely due to cultivar and end-use for the crop (Fulton et al., 2006).

The rapid expansion of perennial crop acreage in the past two decades raises concerns about increasing and hardening water demand (Hanak et al., 2017; Johnson & Cody, 2015; Mall & Herman, 2019). As perennial crops have an expensive initial investment cost, fallowing perennial crops during drought results in greater economic loss than fallowing annual crops. Therefore, GSAs with a high percentage of water use by perennials (Figure 9b, 10b) will likely experience challenges in implementing sustainability management during drought. To minimize economic loss during a severe multi-year drought, a large buffer between the sustainability threshold and actual water level should be maintained for those GSAs, i.e., to prepare for a five-year drought with conditions like 2014's, a groundwater buffer should be aimed with an approximate depth at least five times the values shown in Figure 9c, after accounting for surface water availability and total porosity of the aquifer.

The empirical model developed here for almond orchards could be used for the time-sensitive operation of water resource management, such as predicting in July on the annual total almond consumptive water use during a severe drought year. If future research can demonstrate that NDVI of almond orchards can be predicted using age information and satellite observations from the previous year, our empirical model could be useful to GSAs in project future water use and variability. Furthermore, NDVI measurements are becoming easily accessible to farmers because of the commercialization of affordable, compact field sensors, and drone imaging technology. Therefore, the empirical model could also be used by growers in planning water uses. However, further research is needed to refine the empirical model, so it could estimate daily evapotranspiration estimates using the NDVI data collected by the growers.

5 Conclusions

To facilitate the implementation of sustainable groundwater management, we applied this calibrated approach to the whole Central Valley, one of the world's most productive agricultural regions, to estimate evapotranspiration at 30m resolution for water years 2014 and 2016 when high accuracy local land use maps are available. The evapotranspiration rate averaged at 820 mm yr^{-1} and had a large spatial variability with a standard deviation of 290 mm yr^{-1} over all agricultural pixels in 2014. Total water use in 2016 increased by 9.6%, as compared to 2014, mostly as a result of land-use conversion (2370 km^2) from fallow/idle land in 2014 to cropland in 2016. When aggregated by the GSA boundaries, the annual evapotranspiration rate showed large variation among GSAs, i.e., $\overline{x}$ = 803, σ = 154 mm yr^{-1}, and a CV of 19% in 2014. This variability was mostly associated with variation in net radiation and actual Priestley Taylor coefficient or fraction of reference evapotranspiration, driven by crop type diversity and conditions. Perennial

crops such as pistachios and almonds typically had much higher variability within and among GSAs than annual crops.

Our study demonstrates that remotely sensed evapotranspiration estimates can be combined with land use maps to inform water resources planning and management. In particular, we provided more realistic estimates of crop coefficient and evapotranspiration for local water budget accounting, evaluation of crop water use variation within and among GSAs, and highlighted the importance of crop planning, orchard age structure, and other physiological stressors such as salinity on the trajectory of local orchard water use and demand.

Acknowledgments

We are grateful to Josue Medellin-Azuara and Alvar Escriva-Bou for their assistance. Support for this project was provided by NASA AmericaView and California's Space Grant.

References

Administrative Committee for Pistachios. (2020, February). 2019 Pistachio Bearing Acreage, Production and Yield Per Acre. Retrieved from https://acpistachios.org/wp-content/uploads/2020/02/2019-Pistachio-Statistics-Revised-1.pdf

Baldocchi, D., Dralle, D., Jiang, C., & Ryu, Y. (2019). How Much Water Is Evaporated Across California? A Multiyear Assessment Using a Biophysical Model Forced With Satellite Remote Sensing Data. *Water Resources Research*, *55*(4), 2722–2741. https://doi.org/10.1029/2018WR023884

Burt, C. M., Mutziger, A., Howes, D., & Solomon, K. H. (2002). Evaporation from irrigated agricultural land in California. *Report No. 02-001*.

California Department of Food and Agriculture. (2018). California Agricultural Production Statistics. Retrieved October 23, 2015, from https://www.cdfa.ca.gov/statistics/

California Department of Food and Agriculture. (2020). *2019 California Almond Acreage Report*. Retrieved from https://www.nass.usda.gov/Statistics_by_State/California/Publications/Specialty_and_Other_Releases/Almond/Acreage/202004almac.pdf

California Department of Water Resources. (2019a). *California Water Plan Update 2018*. California Department of Water Resources.

California Department of Water Resources. (2019b). SGMA Groundwater Management. Retrieved May 20, 2019, from http://water.ca.gov/Programs/Groundwater-Management/SGMA-Groundwater-Management

California Department of Water Resources. (2020a). Handbook for Water Budget Development With or Without Models, 446.

California Department of Water Resources. (2020b, January 7). Statewide Crop Mapping. Retrieved from https://data.cnra.ca.gov/dataset/statewide-crop-mapping

CBS. (2015, December 27). Damage from sinking land costing California billions. *CBS NEWS*. Retrieved from https://www.cbsnews.com/news/damage-from-sinking-land-costing-california-billions/

CBS. (2015, December 27). Damage from sinking land costing California billions. *CBS NEWS*. Retrieved from https://www.cbsnews.com/news/damage-from-sinking-land-costing-california-billions/

Chen, B., Jin, Y., & Brown, P. (2019). Automatic mapping of planting year for tree crops with Landsat satellite time series stacks. *ISPRS Journal of Photogrammetry and Remote Sensing*, *151*, 176–188. https://doi.org/10.1016/j.isprsjprs.2019.03.012

Cvijanovic, I., Santer, B. D., Bonfils, C., Lucas, D. D., Chiang, J. C., & Zimmerman, S. (2017). Future loss of Arctic sea-ice cover could drive a substantial decrease in California's rainfall. *Nature Communications*, *8*(1), 1947.

Escriva-Bou, A., Gray, B., Green, S., Harter, T., Jezdimirovic, J., Lund, J., et al. (2019). Water and the Future of the San Joaquin Valley.

Faunt, C. C. (2009). *Groundwater Availability of the Central Valley Aquifer, California* (No. Professional Paper 1766). U.S. Geological Survey.

Faunt, C. C., Sneed, M., Traum, J., & Brandt, J. T. (2016). Water availability and land subsidence in the Central Valley, California, USA. *Hydrogeology Journal*, *24*(3), 675–684. https://doi.org/10.1007/s10040-015-1339-x

Fisher, J. B., Melton, F., Middleton, E., Hain, C., Anderson, M., Allen, R., et al. (2017). The future of evapotranspiration: Global requirements for ecosystem functioning, carbon and climate feedbacks, agricultural management, and water resources: THE FUTURE OF EVAPOTRANSPIRATION. *Water Resources Research*, *53*(4), 2618–2626. https://doi.org/10.1002/2016WR020175

Fulton, A., Bali, K., Mousli, Z., & Jackson, L. (2006). Small grains production manual, Part 5: Irrigation and water relations. *UC Davis*.

Garcia, L. E., Rodriguez, D. J., Wijnen, M. M. P., Pakulski, I., Serrat Capdevila, A., Garcia Ramirez, D. A., et al. (2016). *Earth observation for water resources management : current use and future opportunities for the water sector* (No. 104778) (pp. 1–267). The World Bank. Retrieved from http://documents.worldbank.org/curated/en/783571468196447976/Earth-observation-for-water-resources-management-current-use-and-future-opportunities-for-the-water-sector

Hanak, E. (2011). *Managing California's water: from conflict to reconciliation*. Public Policy Instit. of CA.

Hanak, E., Lund, J., Arnold, B., Escriva-Bou, A., Gray, B., Green, S., et al. (2017). Water stress and a changing San Joaquin Valley. *Public Policy Institute of California*, *1*, 5–48.

Hart, Q. J., Brugnach, M., Temesgen, B., Rueda, C., Ustin, S. L., & Frame, K. (2009). Daily reference evapotranspiration for California using satellite imagery and weather station measurement interpolation. *Civil Engineering and Environmental Systems*, *26*(1), 19–33. https://doi.org/10.1080/10286600802003500

Jin, Y., He, R., Marino, G., Whiting, M., Kent, E., Sanden, B. L., et al. (2018). Spatially variable evapotranspiration over salt affected pistachio orchards analyzed with satellite remote sensing estimates. *Agricultural and Forest Meteorology*, *262*, 178–191. https://doi.org/10.1016/j.agrformet.2018.07.004

Johnson, R., & Cody, B. A. (2015). *California agricultural production and irrigated water use*. Congressional Research Service Sacramento, CA.

Koech, R., & Langat, P. (2018). Improving Irrigation Water Use Efficiency: A Review of Advances, Challenges and Opportunities in the Australian Context. *Water*, *10*(12), 1771. https://doi.org/10.3390/w10121771

Letey, J. (2000). Soil salinity poses challenges for sustainable agriculture and wildlife. *California Agriculture*, *54*(2), 43–48.

Macaulay, L., & Butsic, V. (2017). Ownership characteristics and crop selection in California cropland. *California Agriculture*, *71*(4), 221–230.

Mall, N. K., & Herman, J. D. (2019). Water shortage risks from perennial crop expansion in California's Central Valley. *Environmental Research Letters*, *14*(10), 104014. https://doi.org/10.1088/1748-9326/ab4035

Medellín-Azuara, J., Paw U, K.T., Jin, Y., Jankowski, J., Bell, A.M., Kent, E., et al. (2018). *A Comparative Study for Estimating Crop Evapotranspiration in the Sacramento-San Joaquin Delta*. Center for Watershed Sciences, University of California Davis. Retrieved from https://watershed.ucdavis.edu/project/delta-et

Oki, T., Valeo, C., & Heal, K. (2006). *Hydrology 2020: An Integrating Science to Meet World Water Challenges*. IAHS-AISH publication.

Orang, M. N., Snyder, R. L., Shu, G., Hart, Q. J., Sarreshteh, S., Falk, M., et al. (2013). California Simulation of Evapotranspiration of Applied Water and Agricultural Energy Use in California. *Journal of Integrative Agriculture*, *12*(8), 1371–1388. https://doi.org/10.1016/S2095-3119(13)60742-X

Paul, G., Schmid, B., Chong, C.-S., Roberson, M., Hawkins, T., Smith, A., et al. (2017, May). *California Actual Evapotranspiration (CalETa) Mapping Program: A Critical Component for the Development of Water Budget*. Presented at the Sustainability Groundwater Management Agency Conference.

Schauer, M., & Senay, G. B. (2019). Characterizing Crop Water Use Dynamics in the Central Valley of California Using Landsat-Derived Evapotranspiration. *Remote Sensing*, *11*(15), 1782. https://doi.org/10.3390/rs11151782

Smith, S. (2015, December 28). Damage From Sinking Land Costing California Billions in Infrastructure Repairs. *NBC Bay Area*. Retrieved from https://www.nbcbayarea.com/news/local/damage-from-sinking-land-costing-california-billions-in-infrastructure-repairs/122810/

Strom, S. (2014). California's Thirsting Farmland. *The New York Times*, *20*.

Tucker, C. J. (1979). Red and photographic infrared linear combinations for monitoring vegetation. *Remote Sensing of Environment*, *8*(2), 127–150. https://doi.org/10.1016/0034-4257(79)90013-0

UC-ANR. (2008). Citrus ET by age - Kern County. Retrieved August 25, 2020, from http://cekern.ucanr.edu/Irrigation_Management/Citrus_ET_by_age/

UC-ANR. (2018). Pistachio ET by age - Kern County. Retrieved August 25, 2020, from http://cekern.ucanr.edu/Irrigation_Management/Pistachio_ET_by_age/

U.S. Department of Agriculture. (2020). *2019 California Walnut Acreage Report*. Retrieved from https://www.nass.usda.gov/Statistics_by_State/California/Publications/Specialty_and_Other_Releases/Walnut/Acreage/2020walac_revised.pdf

U.S. Department of Agriculture. (2020, May 8). Quick Stats: National Agricultural Satatistics Service. Retrieved July 28, 2020, from https://quickstats.nass.usda.gov/

U.S. Department of Agriculture - National Agricultural Statistics Service. (2019). 2017 Census of Agriculture - Volume 1, Chapter 2: County Level Data. Retrieved from https://www.nass.usda.gov/Publications/AgCensus/2017/Full_Report/Volume_1,_Chapter_2_County_Level/California/

Wu, H., & Li, Z.-L. (2009). Scale Issues in Remote Sensing: A Review on Analysis, Processing and Modeling. *Sensors*, *9*(3), 1768–1793. https://doi.org/10.3390/s90301768

Xiao, M., Koppa, A., Mekonnen, Z., Pagán, B. R., Zhan, S., Cao, Q., et al. (2017). How much groundwater did California's Central Valley lose during the 2012–2016 drought? *Geophysical Research Letters*, *44*(10), 4872–4879.

Chapter 3: Estimating Agricultural Applied Water by Coupling Remote Sensing Evapotranspiration and Soil Water Balance

Andy. J.Y. Wong[1], Y. Jin[1], G. Fogg[1], S. Solis[1], K.T. Paw U[1], S. Devine[1], W. Henson[2], C. Dogrul[3], T. Kadir[3]

[1] Department of Land, Air and Water Resources, University of California, Davis, CA, USA.

[2] USGS, California Water Science Center, San Diego, CA, USA.

[3] California Department of Water Resources, Sacramento, CA, USA.

The manuscript for this chapter is under revision. We plan to submit this chapter to the Journal of Water Resources Research in May 2021.

Abstract

Information of regional agricultural applied water, or pumping in areas without surface water delivery, is of central importance to sustainable water management activities. However, water accounting is not carefully observed or monitored in most agricultural areas of California, resulting in difficulties in developing an accurate water balance. Field-scale agricultural water use could potentially be inferred from remote sensing of actual crop evapotranspiration, which provides spatial estimates of crop water demands. We here evaluated a pumping estimate, driven by remote-sensing-based daily evapotranspiration at 30m and a soil water balance approach. We focused on the Pajaro Valley, CA, a predominantly agricultural region where groundwater pumping is measured and provides over 90% of the region's water demand. This case study

provides a test of the crop consumptive use approach to estimating groundwater pumping where it is not measured. We first derived the application efficiency for four major crop types in the region, based on 94 field pumping records from a survey, remote sensing evapotranspiration estimates, and a soil water balance model. For regional pumping estimates at the field scale, we applied the median application efficiency for each of the major crop types in the valley. The estimated daily agricultural applied water use at 30m grids is further spatially and temporally aggregated into annual regional and zonal agricultural applied water use estimates. Our applied water estimates can explain 85% of the variability of pumping records at the field scale. However, with a WAPE of 34.7%, it is not suitable for field-scale water accounting. When aggregated to the region, we estimated a total of agricultural groundwater pumping ranging from 53.9 in 2009 to 42.6 billion liters in 2011, which deviated from the sum of all agricultural pumping and surface water delivery by less than 4.6%. Over 16 subregions, our estimates explained more than 89% variance in pumping records with a WAPE of 26.4%. Compared to USGS's estimates from a groundwater model that was finely tuned with zonal water use data, our estimates are more accurate at the regional scale but have larger uncertainty at the local scale. A good agreement was found between USGS's and our estimates, for the major water balance fluxes at sub-regional scale, with R^2 values greater than 0.94. This study results demonstrated that remote sensing evapotranspiration can be used to estimate regional agricultural applied water with reasonable accuracy yet in a cost-efficient way, over areas where only a limited number of field-scale applied water data is available for calibrating a soil water balance model.

1. Introduction

California, as one of the world's most productive agricultural regions, overdrafts 1.2-2.5 trillion liters of groundwater per year (California Department of Water Resources, 2014). In San Joaquin Valley, the southern half of the Central Valley, groundwater overdraft through excessive pumping accounts for 13% of water resources (Hanak et al., 2017). This caused significant land subsidence (Faunt et al., 2016), and the subsequent damages on aqueducts, costing the state "tens of millions of dollars" in repairs to the aqueduct in the last 40 years (Smith, 2015). It also caused many wells to dry up during drought, seawater intrusion, and other undesirable consequences. To address these issues, over 260 Groundwater Sustainability Agencies (GSAs) were formed under the Sustainable Groundwater Management Act to manage local groundwater use and co-manage groundwater basins (California Department of Water Resources, 2019). They depend on groundwater models to develop the water budget and make management and investment decisions (California Department of Water Resources, 2017; Sinclair Knight Merz & National Centre for Groundwater Research and Training, 2012). However, the majority of agricultural groundwater pumping in California is not metered (Escriva-Bou et al., 2016). This creates difficulties in establishing a billing structure for deterring excessive use and funding management operations and infrastructure investments. To estimate regional pumping, modelers adopt different variation the crop consumptive use approach, which uses crop evapotranspiration and irrigation efficiency to estimate agriculture applied water and subtracted by surface water delivery. The lack of pumping measurements, in combination with different assumptions in the crop consumptive use approach, resulted in large discrepancies in pumping estimates of Central Valley's subregions; The subregions, with an average size of 2465 km^2, which is nearly five times the size of the Pajaro Valley, have an average discrepancy of 63% or 271 billion liters per year (Maples, 2019). The discrepancy in Central Valley's sub-regional scale is expected to

magnify at the local GSA scale, potentially mislead local groundwater planning and basin co-management.

Applied water in an agricultural setting refers to water supplied to crops through irrigation. Most irrigated fields in California draw water from both surface water and groundwater. As surface water delivery strictly follows water right regulation, groundwater pumping estimates at a regional scale are generally computed by subtracting surface water delivery records from applied water estimates. Therefore, improving the accuracy of applied water estimates is critical to reducing the uncertainty of the water budget. Due to various geographical factors and individuals' irrigation and field management practices, applied water estimates could differ significantly from crop water demand. For example, in the central coastal regions of California, precipitation typically fulfills the majority of crop water demands during the early growing season, while croplands in the Central Valley may be entirely dependent on irrigation. Meanwhile, irrigation methods, soil characteristics, the slope of irrigated fields, and other conditions, require additional irrigation to ensure soil water moisture at the root zone is sufficient for crop water needs.

For regional water planning purposes, applied water is often estimated as a residual of agricultural water balance. A water balance generally accounts for precipitation, evapotranspiration, and application efficiency. A simple approach, such as the groundwater box model, subtracts temporally-aggregated actual (crop) evapotranspiration from precipitation to compute irrigation requirement, then divides the irrigation requirement by application efficiency to estimate agriculture water demand (Garza-Díaz et al., 2019). If regional measurements of applied water and land use information were available, application efficiency can be calibrated for individual crop types by year to improve the regional applied water estimate.

A more complex approach of agricultural water balance accounts for soil moisture storage (Brady & Weil, 1999; Devine & O'Geen, 2019; McCauley et al., 2005; O'Geen, 2012). In a soil-moisture storage model, precipitation and applied water are stored at the root zone until soil moisture reaches field capacity. The storage is depleted overtime through evapotranspiration. When soil-moisture storage depletes to a predefined threshold (generally at 50% between wilting point and field capacity), irrigation is triggered to fill soil-moisture storage to field capacity. If storage were beyond field capacity, such as during a heavy precipitation event, excess water is partitioned to percolation and surface runoff. The most complex approaches of agricultural water balance involve modeling soil moisture dynamics over time (Hanson et al., 2014; Schmid et al., 2011). These approaches first estimate effective precipitation, which is the amount of precipitation subtracted by the runoffs from precipitation. Then, the models estimate the percolation rate, which should theoretically vary by soil types and soil moisture condition. These approaches are often coupled with a groundwater model. With available measurements, such as metered groundwater pumping, observed groundwater level, stream gauge data, the parameters in the coupled model can be calibrated to match water balance fluxes to measurements.

Although agricultural water balance is constrained by mass balances, regional water balance estimates generally have large uncertainty (Maples, 2019). Modelers lack information on farms' soil property and crop-type and farmer's irrigation method and timing. Uncertainties in forcing data and model parameters could also be propagated and magnified in a model, causing a significant error in applied water estimates. Furthermore, model parameters could be overfitted during the calibration process, introducing errors in estimating water budgets during time periods when measurements are not available. As the majority of local applied water and pumping are

not measured in California (Escriva-Bou et al., 2016), stakeholders rely on the best available water budget estimates to develop water management plans.

Crop evapotranspiration - a key driver for spatial-temporal variability of agricultural applied water - is traditionally estimated using the crop coefficient method (Garza-Díaz et al., 2019; Hanson et al., 2014; Snyder et al., 2012). This method is simple to implement but does not account for field-specific factors, such as water stress, irrigation management, and crop physiological variations, when being implemented for regional water budget purposes. Therefore, this method will likely overestimate actual evapotranspiration (Anderson et al., 2012; Cuenca et al., 2013). The absence of field-specific information hinders regional water managers from accurately estimating local crop evapotranspiration. Thus, some Groundwater Sustainability Agencies (GSAs) in California began to adopt satellite data-driven evapotranspiration estimates in the computation of water budget.

In recent years, many satellite data-driven evapotranspiration estimates have been evaluated (Anderson et al., 2018; Fisher, 2008; He et al., 2017) and commercialized such as products provided by LandIQ, Open ET, Formation Environmental, and The Irrigation Training & Research Center (ITRC). Compared to field measurements, some studies reported a $\pm$10% error. These approaches generally use satellite multispectral and thermal data to model the surface energy balance and then estimate evapotranspiration as a residual of the energy balance. One example is a recently developed semi-empirical model, PT-UCD. It can estimate daily evapotranspiration at 30m resolution in California, with an RMSE of 0.87 mm day^{-1} (Wong et. al. 2021). Since remote sensing evapotranspiration can better capture the temporal changes and spatial variability of crop water use than the traditional crop coefficient approach, it is expected that a water budget driven by remote sensing evapotranspiration can improve estimates of

agricultural applied water. At Olcese GSA, the modeler recently incorporated monthly remote sensing evapotranspiration, from 1993 to 2015, prepared by ITRC using the METRIC model, to prepare a water budget for the groundwater sustainability plan. Similarly, Yuba GSA purchased SEBAL's evapotranspiration map in 2009 and derived crop coefficients to estimate annual evapotranspiration in their water budget. Besides regional water budget preparation, the Environmental Defense Fund and Rosedale-Rio Bravo Water Storage District are experimenting with the application of Open ET's evapotranspiration estimates in field-scale water accounting and trading. While remote sensing evapotranspiration could potentially revolutionize water management, few have evaluated whether it could be used to accurately estimate regional applied water (Martínez-Santos & Martínez-Alfaro, 2010).

In this study, our primary objective is to develop an accurate regional agricultural applied water estimation method at the local GSA scale, using a limited number of field water use data, remote sensing techniques, and soil water balance. We addressed a knowledge gap in using remote sensing actual evapotranspiration to estimate applied water, by quantifying the uncertainty of our estimates from field to GSA scale. We further evaluated our water balance against that of a well-calibrated model and reported the limitations and constraints of remote sensing evapotranspiration in the water budget. Our findings will inform best practices of developing the water budget, thus improving resource planning in the context of the Sustainable Groundwater Management Act.

2. Data and Methods

PT-UCD was applied to estimate daily actual evapotranspiration over the Pajaro Valley in 2009 and 2011 calendar year; A soil water balance model was implemented at daily time-step

in 30m resolution, then the model outputs were spatial-temporally aggregated to the regional and zonal annual average; metered pumping data were used to derive application efficiency at a field scale and to validate applied water estimates from field to regional scales.

2.1 Study Area

Pajaro Valley, with a size of approximately 388 km^2, located in the central coastal part of California, is an excellent region for studying regional agricultural water use because it is one of the few areas in California where agricultural pumping was metered (Figure 1a). If Pajaro Valley were a county, it would rank 5th in agricultural production in California (City of Watsonville, 2009). In 2009, the largest land use in the Pajaro Valley was native vegetation/riparian (47.7%), followed by urban land uses (16.6%). Excluding water, fallow, and non-irrigated crops, 30.3% of the entire valley was irrigated cropland (Hanson et al., 2014). The temperate climate in the region, with mild summer and wet, cool winters, is suitable for growing fruits, vegetables, and nurseries, such as berries, grapes, apples, lettuces, and cut flowers. The most dominant irrigated cropland is vegetable row crops (truck crops) (9.5% of all land uses), followed by strawberry (8.7%), deciduous (orchards) (5.1%), and raspberries, blackberries, and blueberries (3.4%). Pajaro Valley encompasses the Watsonville city and is adjacent to Salinas city; As of 2021, the Watsonville/Salinas district is the largest strawberry production region in California with 49.7km^2 or 43.2% of total fall planted acreage (California Strawberry Commission, 2021), surpassing the total acreage in Florida and is nearly half of the total acreage in Mexico.

The ~100 km^2 irrigated cropland in the Valley consume 48-64 billion-liters of water per year, over 90% of which were extracted from groundwater (Garza-Díaz et al., 2019). Since the 1940s, groundwater overdrafts resulted in seawater intrusion along the coast (Hanson et al.,

2014). Beginning in 2000, wells that pump greater than 12.3 million liters per year (10 acre-feet per year) were required to report pumping measurements to the Pajaro Valley Water Management Agency (PVWMA) (Hanson et al., 2014). PVWMA has since expanded water supply with a Recycled Water Project, a Harkins Slough Recharge Project, and an Import Water Pipeline Project (Hanson et al., 2014). To reduce coastal pumping, PVWMA also built a Coastal Distribution System (CDS) pipeline to deliver water from Harkin Slough, supplemental wells, and a recycled water facility to coastal farms.

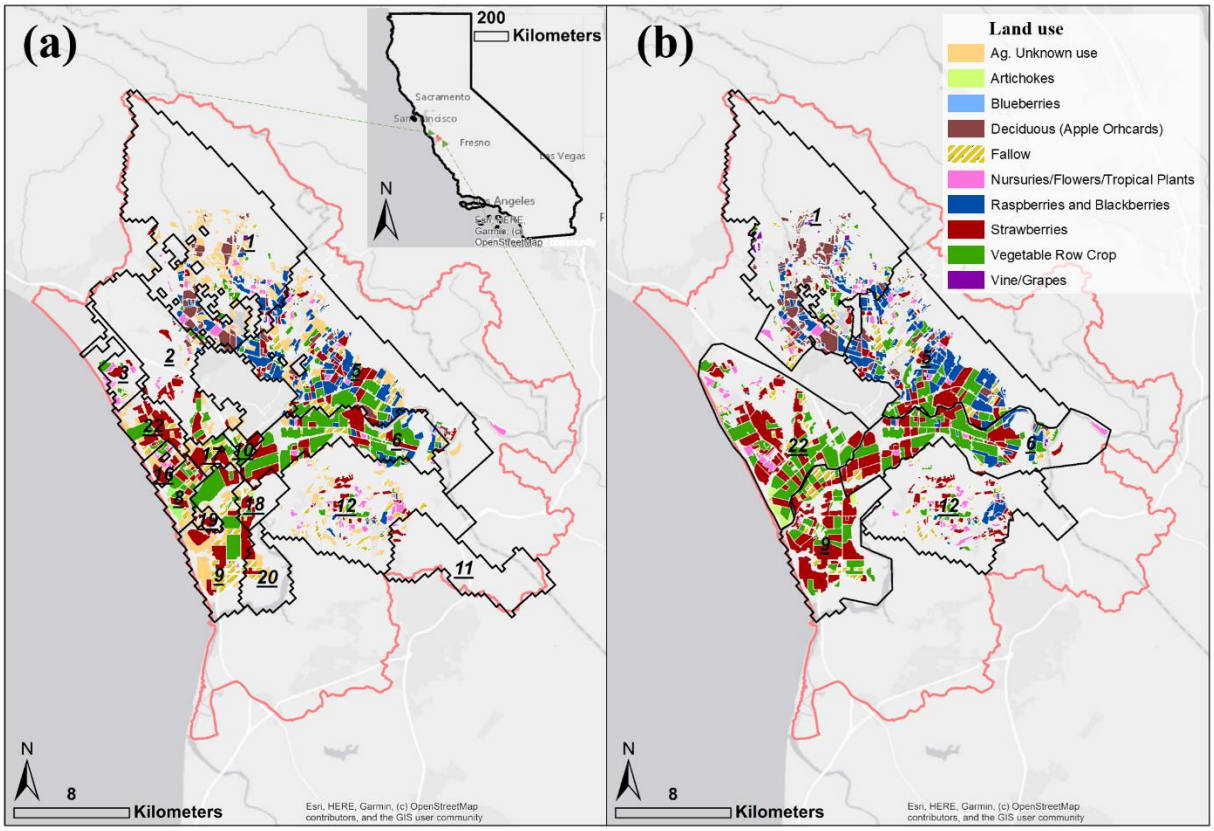

Figure 1. Agricultural land use of the Pajaro Valley watershed in 2009 (a) and 2011 (b). The 22 subregions, as defined by Hanson et al., 2014 were shown in (a), and the modified zones are shown in (b).

Croplands in the Pajaro Valley typically receive about 530 mm yr^{-1} of precipitation. While most of the precipitation occurs in quarters 1 and 4 (January-March and October-December), a significant amount of precipitation is generally available to support crop water needs in quarters 2 (April-June). For example, a total of 31mm and 69mm of precipitation were available in 2009 and 2011 in quarter 2, alleviating the need for irrigation (Figure 2). The total reference evapotranspiration, e.g. crop water needs of well-watered, standardized height pasture, are typically over 800 mm yr^{-1}. The majority of reference evapotranspiration occurred in quarters 2 and 3, each accounting for 35-37% of the annual total in 2009 and 2011. Between the two years, quarter 3's evapotranspiration is 46mm higher in 2009. Higher quarter 3 reference evapotranspiration and lower quarter 2 precipitation helped explain why pumping in spring and summer in 2009 were higher (Figure 2).

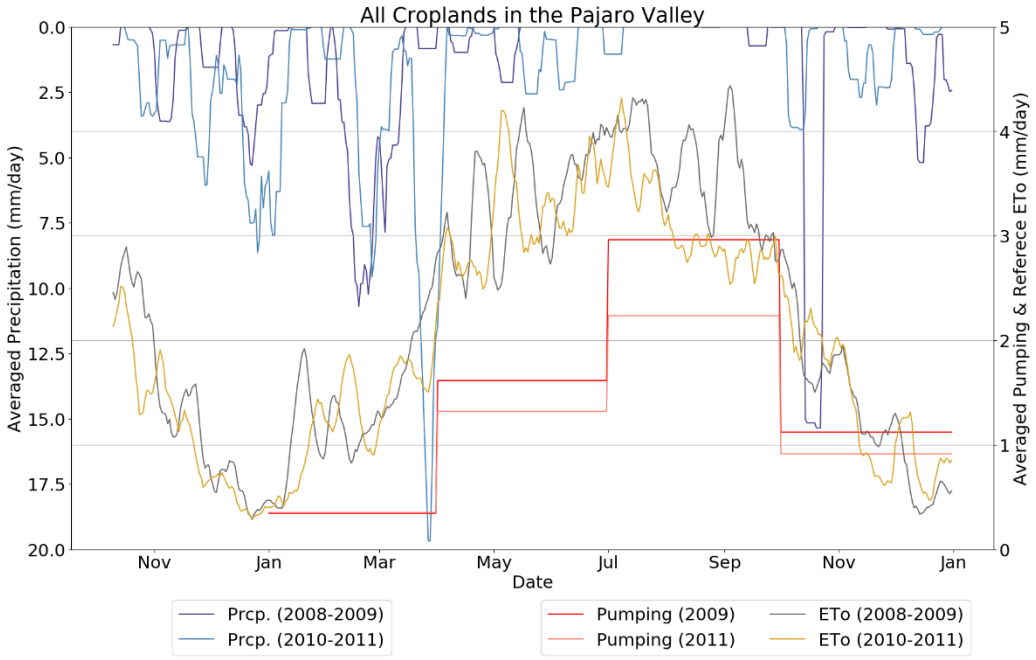

Figure 2. Time series of precipitation (Prcp), reference evapotranspiration (ETo), and Pumping averaged over all croplands in the Pajaro Valley in 2009 and 2011. Precipitation

from Daymet is smoothed with 10 days moving window. Regional total pumping is divided by days in the quarter.

2.2 Land use, parcels, pumping records, and field survey data

The agricultural land-use maps of the Pajaro Valley for 2009 and 2011 were provided by PVWMA. The field ID and land use information was extracted from the original shapefile dataset and rasterized to align with the 30m grid of remote sensing evapotranspiration data. A parcels map, generated by Macaulay & Butsic, (2017), was also used in this study. The map consolidated all land parcels that share an identical landowner name in each county of California. The interactive map is available online and was downloaded for local post-processing using a web-scraping technique.

A confidential field pumping record was provided by PVWMA, documenting quarterly aggregated flow measurements from 2003 to 2011 for every known groundwater pump and CDS outlet. While the majority of pumps are used for irrigation, some were used for residential and industrial purposes. To identify agricultural pumps, we overlaid the well locations on top of parcel maps (Macaulay & Butsic, 2017) and land use maps provided by PVWMA. If a well is not situated in a parcel that contains agricultural land use (including fallow fields), the well is excluded from the study. For validation purposes, the preprocessed agricultural pumping data in 2009 and 2011 were spatially aggregated by subregions as defined in figure 1.

Besides PVWMA's pumping data, Lin et al., (2013) conducted a field survey as part of the potential water savings through an improved irrigation efficiency study. For four crop classes in the valley, namely Vegetable Row Crops, Strawberries, Raspberries and Blackberries, and Deciduous (Apples), a total of 98 growers were surveyed from 2009 and 2011 (Appendix IV

Text S1). The survey documented the IDs of the pumps and the fields operated by the interviewed growers, enabling us to attribute an individual pump to the fields that water was delivered to.

By joining survey records from Lin et al., (2013) with PVWMA's pumping data, field-scale pumping measurements were compiled for the 98 sites. Four sites were omitted because PVWMA's land-use map shows that surveyed sites are either mixed with 'Ag. Unknown use' and 'Fallow' field or identified as 'Nurseries/Flowers/Tropical Plants'. The remaining 94 sites were used to derive field-scale application efficiency for the four major crop types.

For regional pumping estimation purposes, PVWMA's metered records were spatially aggregated according to the zoning definition (Hanson et al., 2014). The Pajaro Valley was divided into 24 water-balance-subregions (WBS) for groundwater modeling at 1km spatial resolution (Figure 1a). In this study, zone 4, 13-15, 24 were excluded, because these areas represent urban water use or the Harkins Slough Aquifer-Storage-and-Recovery System. These zoning schemes have two problems when used for validating pumping estimates. Firstly, WBS zones significantly vary in size, and secondly, the zone boundaries often split land parcels into fragments. A manually modified zone boundary was also used in this study to address the aforementioned issues (Figure 1c). Small WBSs from the original scheme were combined. For example, agricultural fields in WBS 2, 3, 8, 10, 16, 17, 22 were grouped into zone 22, WBS 11 and 12 were combined into zone 12, and WBS 9, 18-20 were aggregated into zone 9. Then, by overlaying the consolidated WBSs with topography and parcel maps, the zonal borders were modified to align along with rivers, watersheds boundaries, and land parcel clusters that have agricultural fields. The modified zone boundary helped better evaluate the uncertainty of zonal pumping estimates, because of the challenge of associating wells to agricultural fields.

2.3 Remote sensing evapotranspiration estimates

We estimated daily crop evapotranspiration at 30m resolution, following the generalized PT-UCD method in Wong et. al. (2021). The estimation requires gridded meteorological data, i.e., minimum and maximum air temperature at 1.5 m, and daily dew point, reference evapotranspiration, from California Irrigation Management Information System Spatial product (Spatial-CIMIS) at a 2 km resolution (Hart et al., 2009). All spatial meteorological data were resampled to the 30m grid of remote sensing evapotranspiration using the nearest neighbor method.

Besides meteorological data, imageries from the Landsat Analysis Ready Dataset (ARD) were used to estimate evapotranspiration on clear-sky satellite overpassing days. The ARD tile 002009 covers the Pajaro Valley watershed, and a total of 167 and 166 days of Landsat 5/7 operational land imager and thermal infrared imageries were compiled in 2009 (August 2008 to January 2010) and 2011 (August 2010 to January 2012), respectively. Although Landsat satellites only revisit the exact location every 16 days, ARD tile images are generated every several days when a satellite captures an image that partially overlaps with the extent of the ARD tile. When both Landsat 5 and 7 are operational during cloud-free seasons, the majority of the Pajaro Valley typically have a maximum of 3 satellite observations per month. However, some areas that are located at the image overlapping zones, may have more observations. After preprocessing the compiled images for quality assurance, evapotranspiration is estimated for all cloud-free pixels. The estimated evapotranspiration value is further divided by reference evapotranspiration to derive the fraction of reference evapotranspiration (EToF) on clear-sky Landsat days.

Daily EToF is estimated with a shape-preserving piecewise cubic interpolation, using all valid EToF values from adjacent clear sky Landsat days within ± 2 months search window. We set a requirement of a minimum of 2 valid observations within the search window for a robust interpolation. This temporal interpolation was needed mostly during the rainy season in winter and early spring in California, an off-season for some crops in Pajaro Valley. Finally, daily evapotranspiration was estimated as a product of the interpolated EToF and reference evapotranspiration. At last, the estimated daily evapotranspiration over the ARD tile was clipped by a boxed area encompassing the watershed for further analysis.

2.4 Soil Water Balance Model

The Soil water balance model was implemented in Python at a daily time step with a 30m grid. The model (Figure 3) resembles the Irrigation Demand Calculator (IDC) (California Department of Water Resources, 2020). IDC is an integrated component of the Integrated Water Flow Model, which is applied in the California Central Valley Groundwater-Surface Water Simulation Model (Sustainable Groundwater Management Office, 2020) and other basin-wide groundwater modeling (Harter & Morel-Seytoux, 2013). A key difference between IDC and our model is that IDC solves the soil water balance equations using an iterative solution, while our approach computes the equations in a specific sequence in daily time steps. Another difference is that IDC is more flexible and is suitable for non-agricultural land use, while our model is constrained to agricultural land use with specific assumptions. For example, IDC users may add parameters to account for drainage and a root zone that changes over time.

We built the model from scratch to minimize labor-intensive tasks of converting various gridded data into text files and extracting output files for data analysis. Our end-to-end

automated model enables modification of calculation and optimization approaches and rapidly testing of different assumptions, thus it is well suited for developing a proof of concept. For regional management purposes, our approach should be reimplemented in a well-evaluated model, such as IDC and the Farm Process Module (Schmid & Hanson, 2009), which could be directly integrated into a groundwater model.

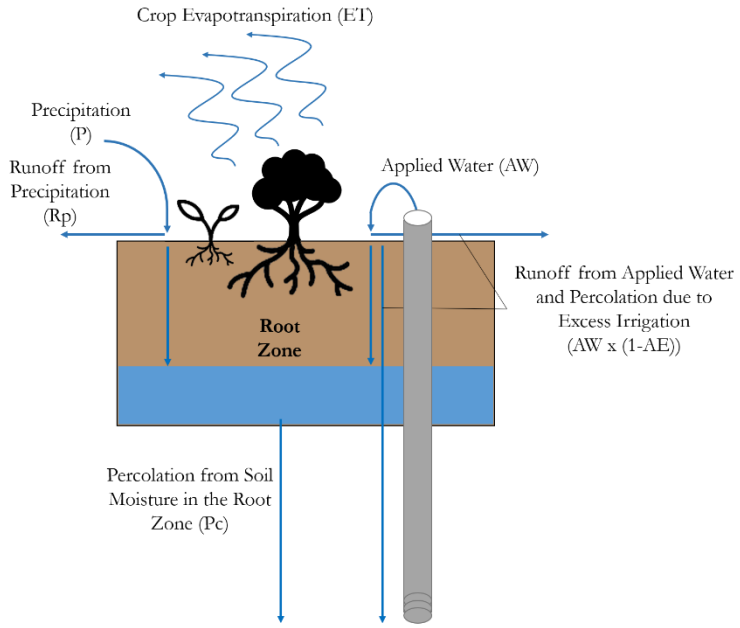

Figure 3. Conceptual Diagram of the Soil Water Balance Model.

2.4.1 Day-to-day Soil Moisture Accounting in the Root Zone

The proposed model is governed by the conservation of mass, in which the amount of soil water in the root zone at day *t* is a product of soil moisture (θ^t) and root depth (z^t). Assuming a constant root depth, available soil water on the present day (t) is the sum of the available soil water from the previous day (t-1) and the residual water balance on the present day (W_b^t), as shown in equation 3.1.

$$\theta^t z = \theta^{t-1} z + \Delta t W_b^t \quad (1)$$

The depth of the root zone is spatially defined by land-use type, based on values used in (Hanson et al., 2014) (Appendix IV Text S2). A constant root depth is assumed for implementing the water balance. Meanwhile, all soil-related parameters at the root zone are based on the soil property maps provided by California Soil Resources Laboratory (O'Geen, n.d.) (Appendix IV Text S3). The maps were originally derived from the USDA-NCSS soil survey data and aggregated into an 800m^2 grid cell. We resampled them to Landsat's 30m grid using bilinear interpolation and gap-filled the unknown value along the coast using nearest neighbors resampling technique.

2.4.2 Intraday Water Balance

The computation of W_b^t accounted for major water fluxes, including percolation (P_c), precipitation (P), direct runoff from precipitation (R_p), evapotranspiration (ET), applied water (A_W), and return flow of applied water (R_f). By approximating the return flow equation from IDC with application efficiency (AE), crop irrigation water demand (${A_W}^t - {R_f}^t$) can be rewritten as a product of application efficiency and applied water. With the model operating at daily time step ($\Delta t = 1$), equation 3.1 can be rewritten as:

$$\theta^t z = (\theta^{t-1} z - P_c^t) + (P^t - {R_p}^t) - ET^t + ({A_W}^t * AE) \quad (1.1)$$

Given soil moisture from the previous time step ($\theta^{t-1} z$), percolation (P_c) at the present time step is estimated with equation 2, using mean saturated hydraulic conductivity (K_s), total porosity (θ_T) (Appendix IV Text S3), and a parameter m, which is computed from the pore size distribution index (λ) (Appendix IV Text S4) with $m = \lambda/(\lambda + 1)$.

$$P_c^t = K_s(\frac{\theta^{t-1}}{\theta_T})^{0.5}(1-(1-(\frac{\theta^{t-1}}{\theta_T})^{1/m})^m)^2 \quad (2)$$

After accounting water loss at the root zone via percolation, precipitation (P^t) is added. Daily precipitation at a 1km grid was obtained from NASA's Daymet Version 3 product (Thornton et al., 2017) and resampled to the model's 30m grid. Part of precipitation leaves the field as runoff (${R_p}^t$), which is estimated with SCS curve number method, where ${R_p}^t = \frac{1}{\Delta t}\frac{P^t\Delta t-0.2S}{P^t\Delta t+0.8S}$. Details of computing the curve number and soil moisture-driven parameter, S, can be found in Appendix IV Text S5. The difference between $P^t$and ${R_p}^t$, also known as effective precipitation, is added to the present soil moisture.

The soil moisture, after accounting for outflows for percolation and evapotranspiration and inflow from effective precipitation, is used to determine the quantity and timing of irrigation. This intermediate simulated moisture (${\theta_{sim}}^t$), where ${\theta_{sim}}^t = \frac{(\theta^{t-1}z-P_c^t)+(P^t-{R_p}^t)-ET^t}{z^t}$, is compared with field capacity (θ_f) (Appendix IV Text S3). If ${\theta_{sim}}^t$depletes below or equal to 50% of field capacity, an irrigation event at the 30m cell is triggered. The amount of applied water is dictated by application efficiency, root depth, and the difference between field capacity and intermediate simulated moisture, such that ${A_W}^t = z(\theta_f - {\theta_{sim}}^t)/AE$.

2.5 Derivation and analysis of field-specific application efficiency

Application Efficiency is defined as the fraction of the volume of irrigation water stored in the root zone to the volume of irrigation water delivered to the field. In practice, application efficiency is often used interchangeably with irrigation efficiency by assuming other beneficial water use, such as removal of salts, microclimate control, seedbed preparation, and softening of a

soil crust for seedling emergence, did not occur in the field. Depending on model designs, application efficiency may or may not account for deep percolation. Our approach estimated deep percolation from soil moisture storage in the root zone. However, at a field scale, applied water entering the soil might exceed field capacity and this excess soil moisture, rather than stored at the root zone, typically percolates quickly across the root zone. Because the estimation of crop irrigation demand is constrained by $(\theta_f - {\theta_{sim}}^t)$, the application efficiency, derived from matching estimated applied water and actual pumping, accounts not only for runoff from irrigation but also for percolation due to applied water in excess of field capacity (Figure 3).

The application efficiency values were derived for 94 surveyed fields across four major crop types in the Pajaro Valley. To implement the derivation, water balance models were executed 99 times, each with a different application efficiency (ranging from 1% to 99% with 1% increment) applied uniformly across the Pajaro Valley. At each iteration, the 30m grid estimates of daily applied water were aggregated spatially for each surveyed field and temporally for the full calendar year. The applied water estimates from the iterations were recorded, and application efficiency is derived for each specific field by finding the best match (minimum absolute percentage error) between the estimates and the reported pumping. In some scenarios, the best match could not be derived. For example, if measured pumping is zeros and the amount of precipitation stored in the root zone is less than percolation and evapotranspiration, the derived application efficiency is invalid.

The derived field-specific application efficiency (n=94) was summarized by crop types with median, standard deviation, lower (25th percentiles), and upper (75th percentile) quantiles. The applicability of derived efficiency value is further evaluated at selected sites. Of the 94

surveyed fields, 52 fields were surveyed in 2009, among which 13 were re-visited in 2011. Nine of those revisited did not experience land-use changes in 2009 and 2011 according to PVWMA's land-use map. Despite some sites having changes in application areas, we assumed that the growers did not change irrigation practices and conducted an evaluation. Specifically, we used the derived application efficiency values from 2009 to estimate applied water in 2011 and quantified the errors by comparing them with pumping records. Besides the 13 re-visited fields, 68 fields were surveyed in only one of those two years; 16 of those had unchanged crop type and a non-zero pumping in quarter 3 for both years. For these 16 sites, we assumed that attribution between irrigation application areas and identified wells did not change between the two years and used the derived application efficiency value from the survey year to estimate applied water at the same field in a non-surveyed year. When comparing estimated applied water with field pumping measurements, our estimates are evaluated with four metrics, including R^2 which is also known as Nash-Sutcliffe model efficiency coefficient, root means squared error (RMSE), and mean absolute error (MAE), and weighted absolute percentage error (WAPE).

2.6 Validation of spatial applied water estimates from field to regional scales

For practical application of applied water estimates, field-scale pumping records for all croplands are rarely available for back-calculation of field-specific application efficiency. To spatially estimate applied water, we computed a median of all previously derived field-specific application efficiency values for each of the four major crop types and used it to generate a map of application efficiency in a 30m grid based on land use. Combining the application efficiency map, remote sensing evapotranspiration, and the soil water balance model, we computed spatial applied water estimates at the daily time step for 2009 and 2011.

The estimates were temporally summed to annual total, then spatially aggregated in four different ways for evaluations. First, the annual total applied water estimates over the 94 surveyed fields were extracted and compared with pumping estimates. Estimates over the 16 once surveyed fields during the non-surveyed year were extracted for comparison. Second, the spatial estimates over all croplands in the Pajaro Valley were aggregated and compared with the spatially aggregated field pumping measurements (section 2.2). Lastly, the spatial estimates were aggregated according to the original and modified zonal maps (Figure 1) and evaluated with the respective aggregated field pumping measurements.

2.7 Comparison of zonal water budget fluxes

The annual applied water estimate in 2009 was compared to PVHM's estimate at regional and unmodified zonal scale. To quantify the agreement at zonal scale between two models, RMSE and Pearson's correlation coefficient (r) with P-value were calculated. A best-fit line is also derived and the line's R^2 is computed. Although our study focuses on estimating applied water in croplands, the comparison between the two models was conducted by aggregating all pixels within subregions, instead of aggregating only cropland pixels. It is because the most recently published PVHM used an older version of the hydrological computation model that could not export intermediate products, such as evapotranspiration and runoffs, in a grid format. The model produces a detailed water budget by subregions but did not separate fluxes between croplands and other land uses. Thus, the model comparison was limited to a zonal scale with the original WBS definition.

To determine whether the proposed water balance could effectively estimate the hydrological fluxes in the valley, we compared precipitation, evapotranspiration, and non-

evapotranspiration outflows between our estimates and PVHM over 16 agricultural dominant zones. PVHM's water budget is expected to be a good representation of the actual hydrological process in the Pajaro Valley because it was calibrated and evaluated with the best available pumping, groundwater level, and river flow observations. Instead of comparing runoff and deep percolation separately, the two fluxes are combined into non-evapotranspiration water outflows for comparison. The reason is that the proposed model could not separate irrigation inefficiency into direct runoff and immediate deep percolation due to irrigation exceeding field capacity in the root zone. It is also important to note that the non-evapotranspiration water balance outflows of the proposed model are indirectly computed. We assumed that changes in soil moisture at the root zone are negligible at the annual time scale, so outflows could be quantified as the sum of precipitation and applied water, subtracting evapotranspiration.

In PVHM, evapotranspiration is estimated using the traditional monthly crop coefficient approach. The crop coefficient is adjusted with a scale factor that varies between dry and wet years. Unlike remote sensing evapotranspiration, the zonal variation of PVHM's evapotranspiration estimates is primarily driven by the difference in the proportion of major land uses and reference evapotranspiration. The remote sensing evapotranspiration estimation method in this study has not been tested on the natural landscape. To effectively compare zonal evapotranspiration between the models, remote sensing evapotranspiration over non-cropland-pixels was adjusted with the help of soil water balance. In specific, applied water was constrained as 0 over non-agricultural pixels. At these pixels, when soil moisture conditions at the root zone drop below 50% of field capacity, evapotranspiration estimates of the day were adjusted to 0.

Using evapotranspiration, PVHM employed a slightly different approach than IDC in computing agricultural applied water. Aside from differences in input data, e.g. precipitation and reference evapotranspiration, the most significant difference between PVHM and the proposed approach is that the on-farm application efficiency of PVHM is optimized by crop types, subregions, years, and months. For the same year and month, a large difference in application efficiency value, e.g. >=54% in August 2009, is observed among zones for vegetables and strawberries, which are the top two agricultural land use in the region. Relatively small (>=26%) or no variation across subregions were found for other crop types.

3. Results

3.1 Field Scale Application Efficiency

We found the derived application efficiency at the field scales varied among crop types (Figure 4). Apple orchards had the highest application efficiency, mostly at the maximum limit of 0.99 (σ = 0.17 in standard deviation) (n=22), while raspberries and blackberries had the lowest application efficiency with a median of 0.35 (σ = 0.19) (n=25). Application efficiency for vegetable row crops such as lettuce, broccoli, and cauliflower was slightly higher than that of strawberries, with a median of 0.55 (σ = 0.27) (n=22) versus 0.49 (σ = 0.21) (n=25) (Figure 4, Appendix 4 Table S1). Their interquartile range ranges from 0.23 to 0.45. Small clusters of application efficiency for these crops were observed in figure 4 and they may be associated with soil type, irrigation method, and field management practices.

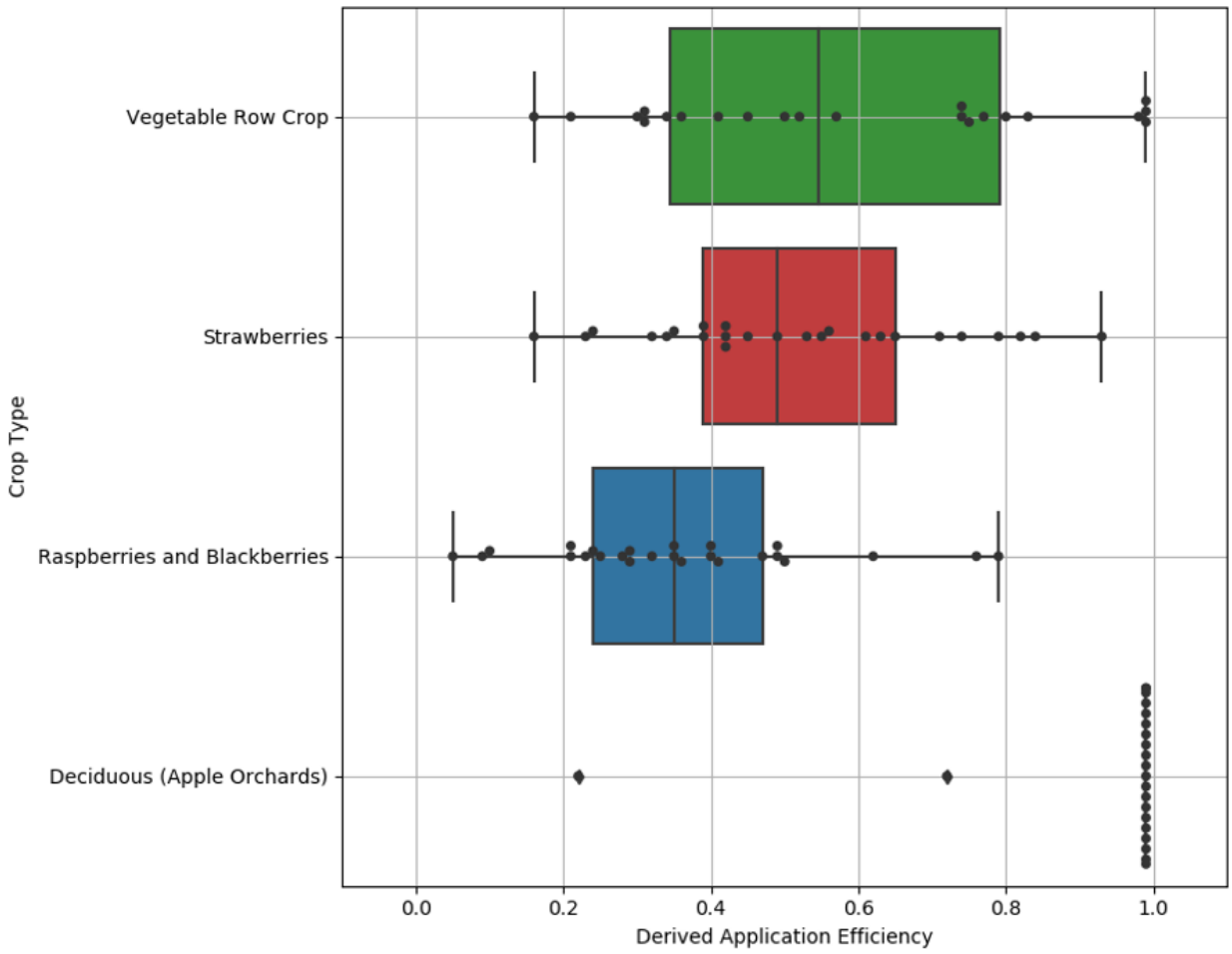

Figure 4. Box plot of derived field-specific application efficiency over the 94 surveyed fields four major crop types in the Pajaro Valley. The values are derived by iterating the application efficiency value in a soil water balance model and finding the value that best matches the estimated annual applied water use with pumping records at the field. The derived value from each field is represented by a dot. The box plot shows the quartiles of the dataset. The upper whisker is extended to the last datum less than the sum of the 1.5 times of interquartile range and the 3rd quartile. Similarly, the lower whisker is extended to the first datum greater than the first quartile subtracted by the 1.5 times of interquartile range.

3.2 Field Scale Applied Water Estimates

When using the field-specific application efficiency derived from one year, the estimated applied water, based on satellite-derived evapotranspiration and simple soil balance model, agreed well with the pumping records (Table 1, Figure 5), with an R^2 greater than 0.80, RMSE less than 23.84 million liters, and WAPE less than 32.9% among fields. When compared in a per-area unit, the estimates have an RMSE of 0.17 m/year and 0.16 m/year, respectively at the twice and once surveyed, unchanged land-use sites.

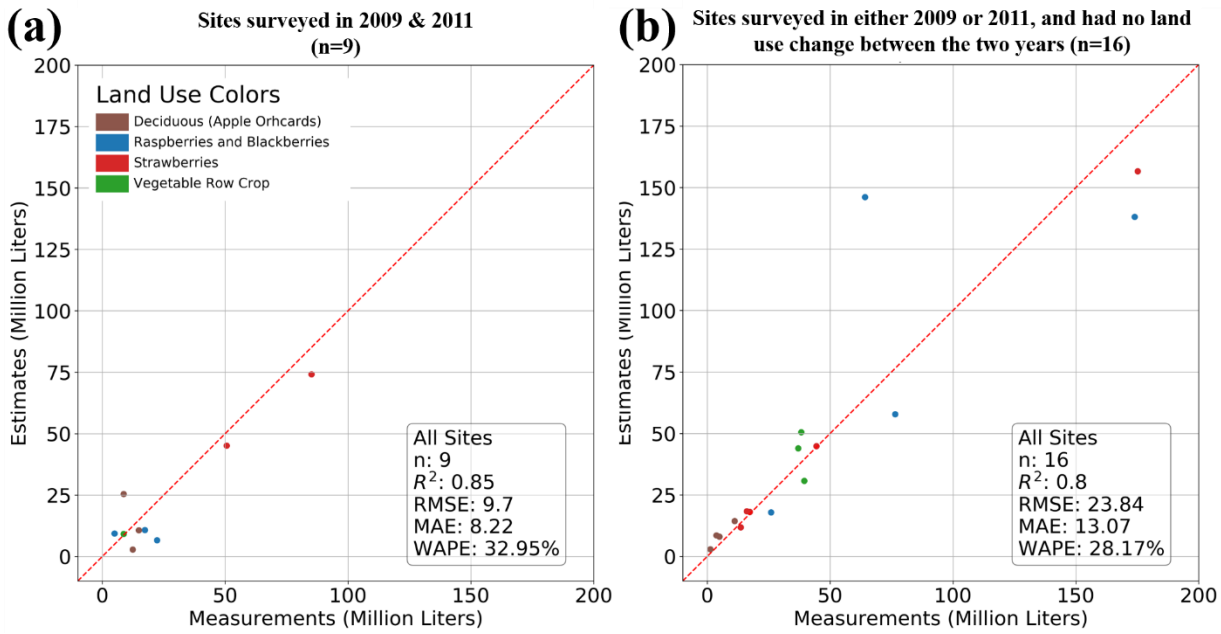

Figure 5. Evaluation of applied water estimates based on derived field-specific application efficiency vs. pumping records at selected sites from the 2009 and 2011 survey. The selected sites did not experience land-use change between the two years. Sites that were surveyed in both years were shown in (a), where the application efficiency values were derived from 2009 and used for applied water estimates in 2011. Sites that were surveyed once in either 2009 or 2011 were shown in (b), where the application

efficiency values were derived from the surveyed year and used for applied water estimates in the non-surveyed year.

Table 1. Model uncertainties of applied water estimate using field-specific or crop-specific applied efficiency.

Application Efficiency	All Surveyed Sites (n = 94)				Sites Surveyed in both 2009 & 2011 (Evaluated with 2011 records) (n = 9)				Sites Surveyed in either 2009 & 2011, with no land-use change (Evaluated with non-surveyed year records) (n = 16)			
	R^2	RMSE	MAE	WAPE	R^2	RMSE	MAE	WAPE	R^2	RMSE	MAE	WAPE
Field Specific	N/A				0.85	9.70	8.22	33.0 %	0.80	23.84	13.07	28.2 %
Median	0.86	39.58	24.70	34.7 %	0.86	9.22	7.71	30.9 %	0.72	27.98	18.70	40.3 %

For spatial applied water estimates, we used the crop-specific median application efficiency values from Appendix IV Table S1 to define application efficiency at a field scale. The performance only reduced slightly, especially over the 9 fields where exact well attributions to the fields were known, with a WAPE of 35.4% and 30.9% in 2009 and 2011, respectively. At sites that were surveyed once or twice and with identical land use in both years, the performance of applied water estimates for median-based spatial estimates is worse than that for field-specific derived value, with an R^2 greater than 0.72, RMSE less than 27.98 million liters, and WAPE of less than 40.3% (Table 1 and Figure 6). The increase in uncertainty is primarily contributed by a nearly 100% overestimation of water use at a raspberries and blackberries site. This site is possibly an outlier, as the attribution between well to irrigation areas is uncertain. When compared in a per-area unit, the estimates have an RMSE of 0.17 m/year and 0.21 m/year, respectively for the twice and once surveyed sites. Although the estimates based on field-specific and median application efficient values were similar at the evaluation and simulation sites, it is

uncertain whether the median-based estimate is suitable for field-scale applied water estimates. Compared to pumping records overall surveyed sites, the median-based estimate had an R^2 of 0.86, WAPE of 34.7%, and RMSE of 39.58 million liters, which is equivalent to an RMSE of 0.29 m/year.

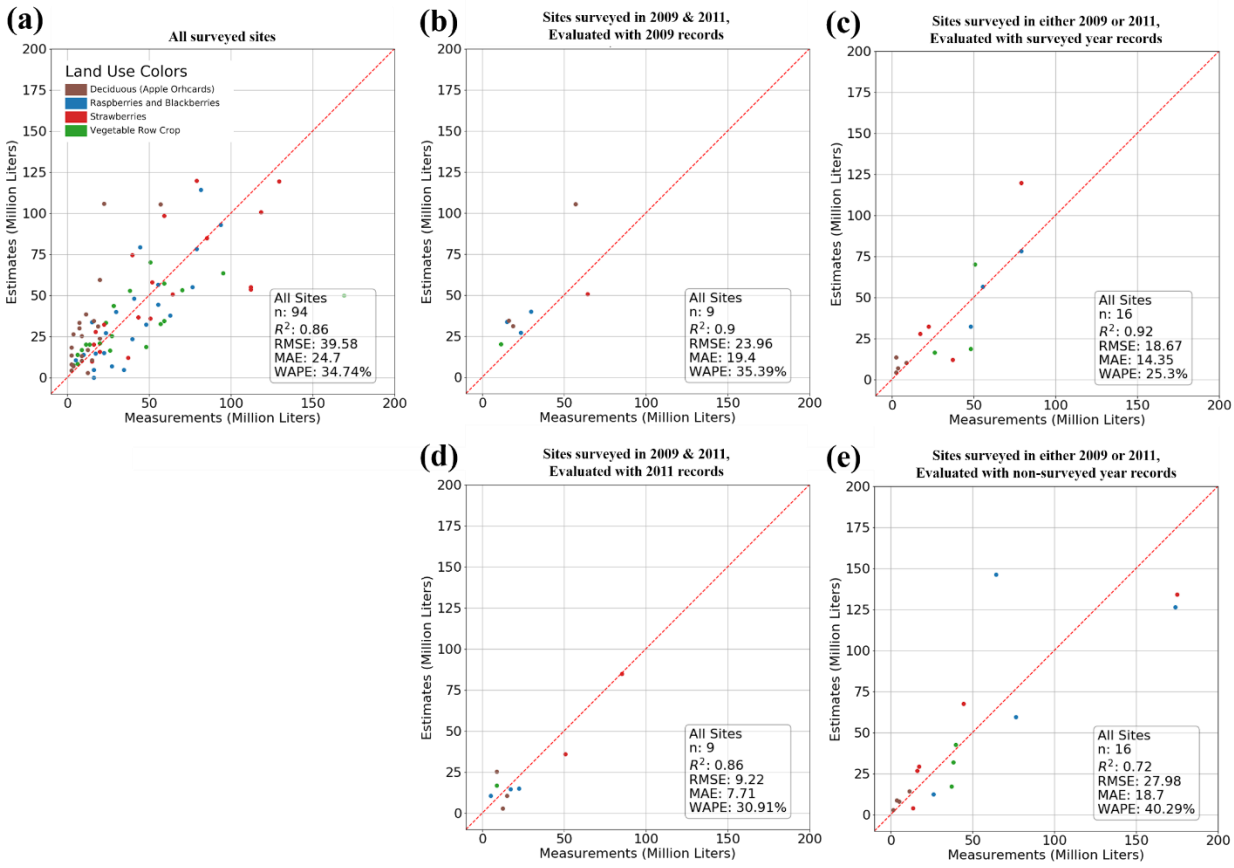

Figure 6. Evaluation of spatial applied water estimates (based on the crop-specific median of derived application efficiency values) vs. pumping records at selected sites from the 2009 and 2011 survey. The selected sites, in b through d, did not experience land-use change between the two years. The estimates are computed with a soil water balance using the median application efficiency values for the four major crop types. The comparison with all surveyed sites is shown in (a). Sites that were surveyed in both years

are shown in (b & d), with pumping records from 2009 compared in (b) and 2011 in (d). Sites that were surveyed once in either year are shown in (c & e), with pumping records from the surveyed year shown in (c) and non-surveyed in (e).

3.3 Regional and Zonal Applied Water Estimates

The 30m spatial estimates of field scale applied water (Figure 7b) were aggregated spatially to estimate regional and zonal total agricultural applied water use. Our estimates of the regional total of agricultural applied water, based on the median of derived application efficiency, agree well with aggregated measurements. The agreement is comparable to that by Hanson et al., (2014). At the regional scale, we estimated that the agricultural applied water was 53.9 and 42.6 billion liters in 2009 and 2011, respectively. Compared to regionally aggregated pumping measurements (pumping from wells and water delivered via CDS), our estimates deviate by -2.9% in 2009 and 4.6% in 2011. On the other hand, Hanson et al., (2014) estimated that 57.8 billion liters of groundwater were pumped in the valley in 2009, which is 4.2% higher than the measurement.

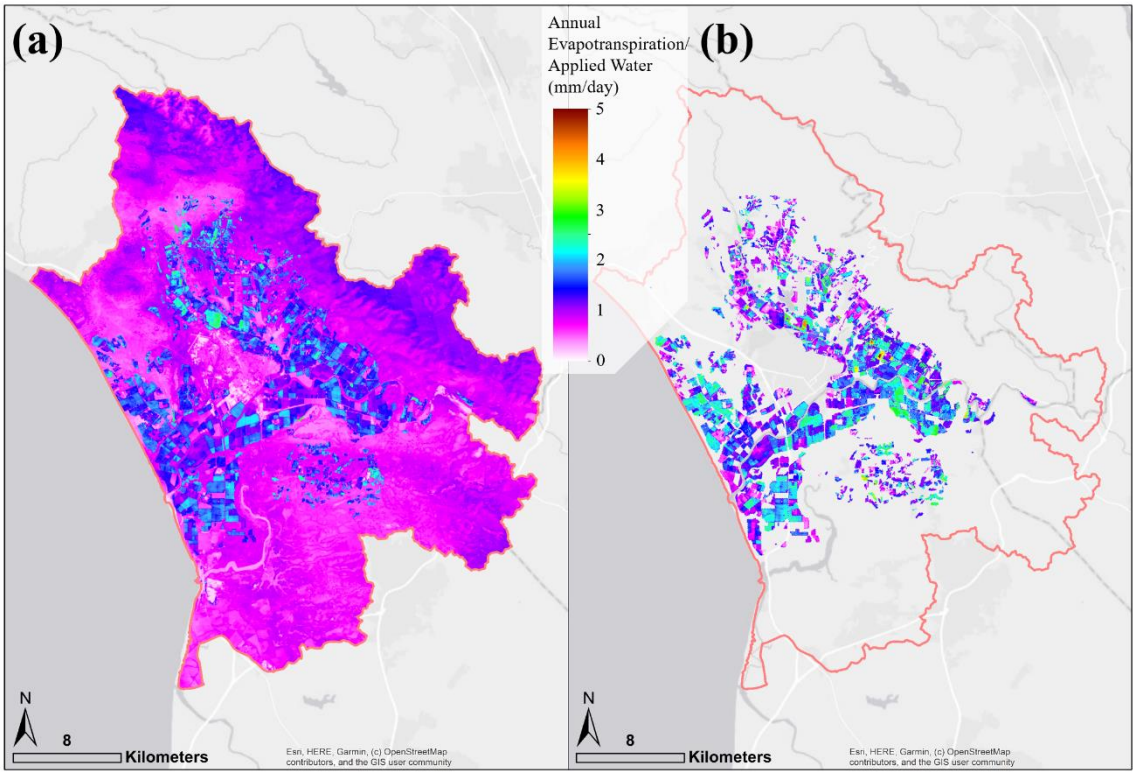

Figure 7. Visualization of spatial estimates of evapotranspiration (a) and applied water (b) in 2009. The evapotranspiration shown here was adjusted over non-cropland-pixels during the soil water balance computation; At non-cropland pixels, if soil moisture conditions at the root zone drop below 50% of field capacity, evapotranspiration estimates of the day were adjusted to 0.

At zonal scale with the PVHM's original boundaries, a reasonable agreement was found between aggregated pumping records and applied water estimates in 2009 and 2011 (Figure 8, Appendix IV Figure S1), with R^2 of 0.89, MAE of 810 million liters, RMSE of 1215 million liters, and WAPE of 26.36%. In 2009, PVHM's estimates had an R^2 of 0.97, MAE of 548 million liters, RMSE of 704 million liters, and WAPE of 16.09%. Our estimates in 2009 have

much greater uncertainty than PVHM's, with an R^2 of 0.89, MAE of 900 million liters, RMSE of 1264 million liters, and WAPE of 26.42%.

The performance of our estimates in 2009 and 2011 worsened when zonal boundaries were modified, with an overall R^2 of 0.84, MAE of 1318 million liters, and RMSE of 1633 million liters. However, the overall WAPE decreased from 26.36% to 15.8%. Modification on the subregions, e.g. aggregating small subregions and modifying borders according to natural boundaries, such as watersheds, rivers, and clusters of fields, helped reduce the total percent errors. For example, the seven small subregions near WBS 22 under the original boundaries had percent errors ranging from -43 to 41% in 2009 (Appendix IV Figure S1a). Through grouping subregions, the percent errors reduced to -11% in 2009 (Appendix IV Figure S1d).

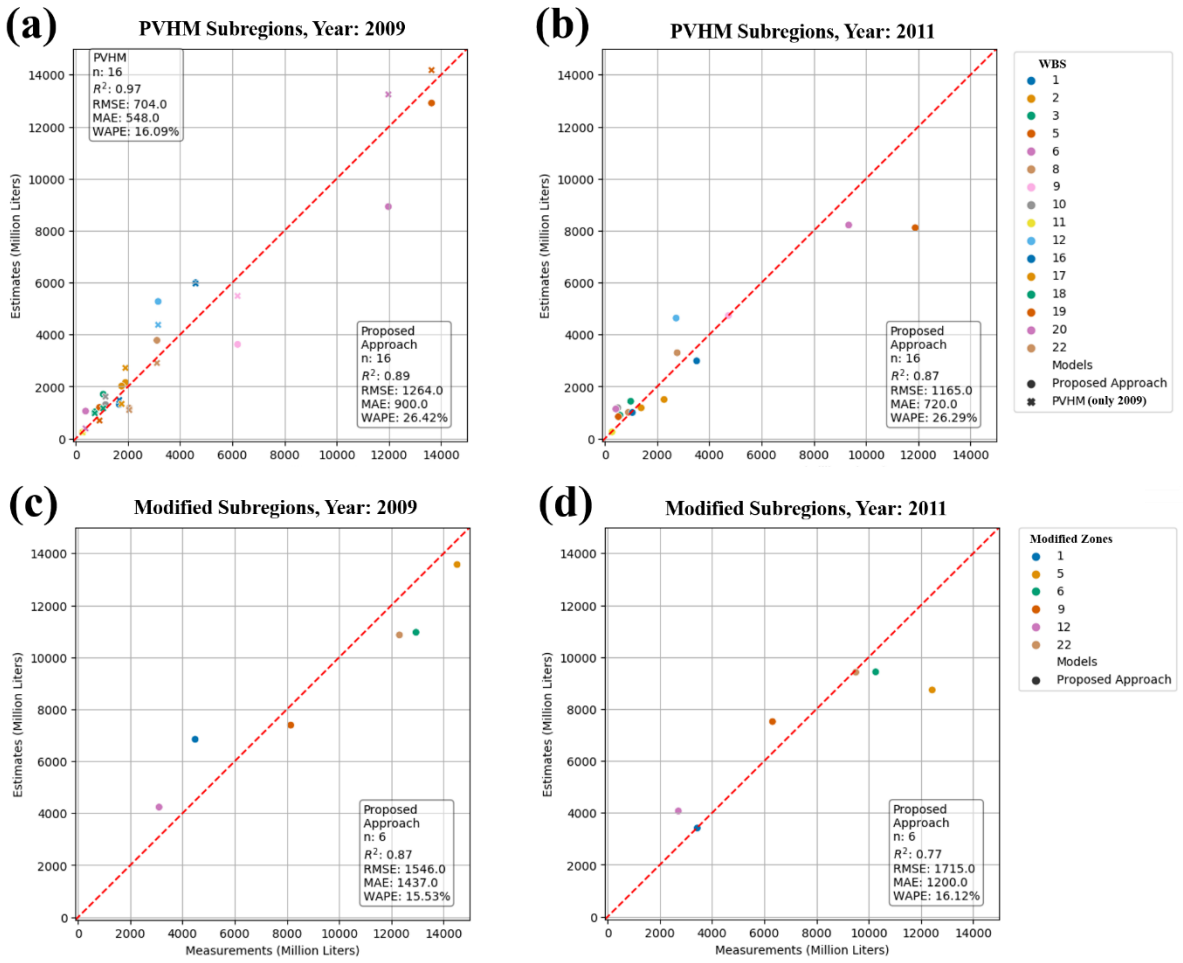

Figure 8. Comparison of annual zonal agricultural pumping estimates with measurements. Estimates for 2009 (left) and 2011 (right) were shown above. Results are based on PVHM's zones (top) and the modified zones (bottom). PVHM's 2009 estimates are also shown (a).

Our estimates have higher uncertainty than PVHM when compared to aggregated pumping records, but our estimates agree well with PVHM's. Comparing our estimates with PVHM's yielded the best fit line, where our estimates are equal to 90% of PVHM's estimates subtracted by 38.8 million liters. The two estimates are highly correlated, with an r-value of 0.98, and an RMSE of 926 million liters (Figure 9). Among the major fluxes in a water balance, the

two models agree best, in terms of RMSE, for applied water, followed by evapotranspiration, precipitation, and then non-evapotranspiration water balance outflows.

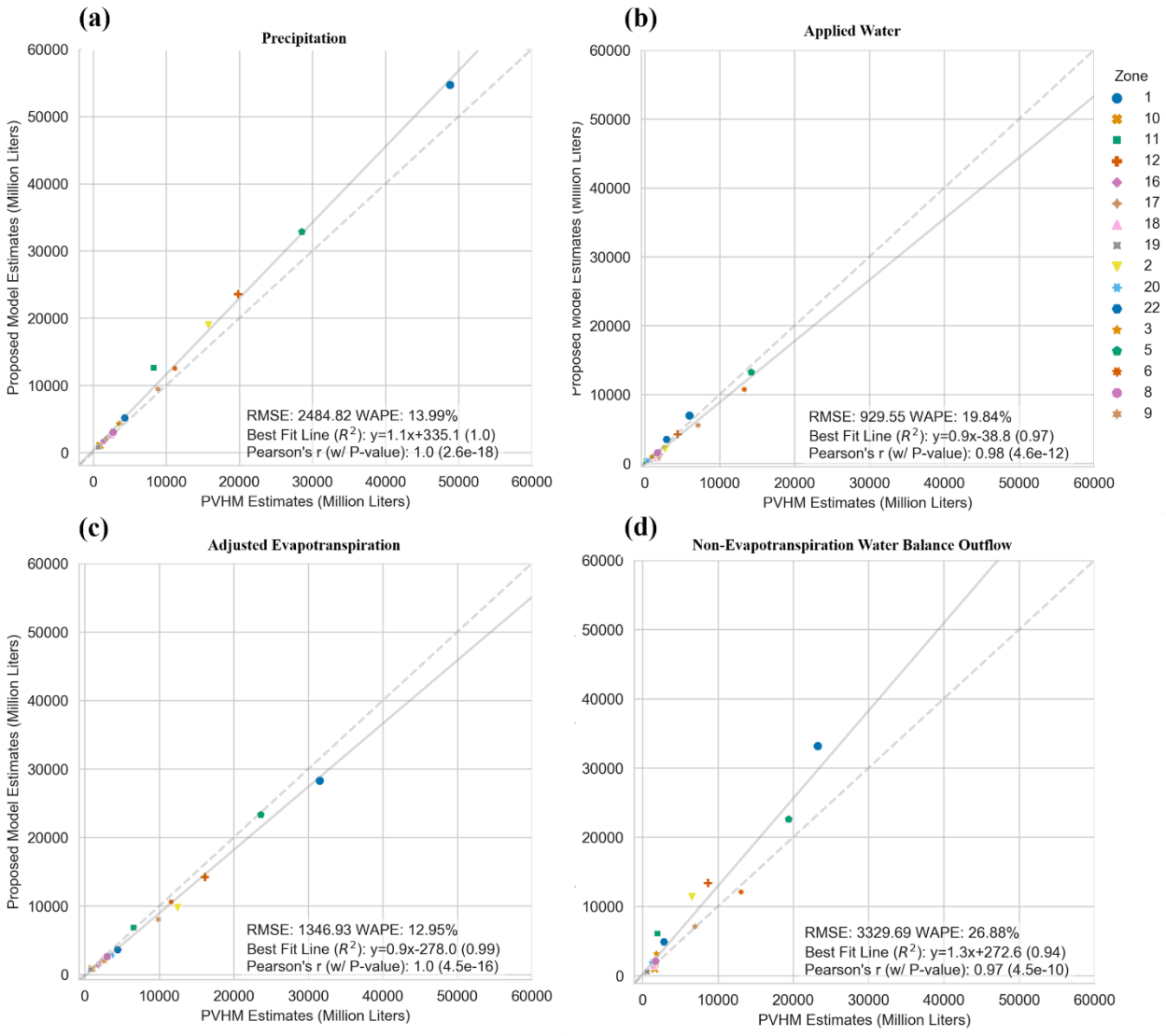

Figure 9. Comparison of annual zonal water budget fluxes between PVHM and the proposed model in 2009. Estimates of precipitation (a), applied water (b), evapotranspiration (c), and non-evapotranspiration water balance outflow (d) were shown above. Remote sensing evapotranspiration estimates for the proposed model are adjusted

over non-irrigated and non-agricultural pixels, where daily evapotranspiration becomes zero when soil moisture in the root zone reaches below 50% of field capacity.

4. Discussion

Our study demonstrated that remote sensing evapotranspiration estimates could be used in a soil water balance for estimating applied water from field to regional scales. In previous studies, an accurate regional applied water estimation requires regional pumping measurement data and complex calibration. Here, we showed that a comparable estimate can be achieved by coupling remote sensing evapotranspiration and a relatively simple soil water balance and by using a limited quantity of annual pumping records (n=94).

4.1 Field-scale applied water estimates

With traditional approaches that use crop coefficient-based evapotranspiration, field-scale applied water estimates are unfeasible. It is because two nearby fields growing the same crop, would have an identical evapotranspiration rate; If the two fields share the same soil conditions, their crop irrigation demand would also be identical. Remote sensing based evapotranspiration, on the other hand, could capture the spatial variability due to management practices and rapid water stresses, thus enabling the possibility of field or local scale water balance.

Our study confirms that field-scale estimates of applied water are feasible. However, several challenges require further research and investigation. Firstly, our approach is constrained by data availability of local field scale pumping, as well as the ability to estimate application efficiency when the pumping measurement is not available. With derived application efficiency data at the Pajaro Valley, a model could be developed to map field-specific application

efficiency values based on spatial maps and ancillary data. The current data and model also support seasonal derivation of application efficiency, but more study is needed to understand the variability and season-to-season changes of the efficiency value. In addition, fulfilling crop water needs is only of many agricultural uses of water; Other uses, such as salt flushing and frost control, are not explicitly modeled in the soil water balance. Therefore, when application efficiency value is derived by equating crop water demand and percolation with pumping at annual timescale, the derived application efficiency value may seem low if the groundwater were used for other purposes and may introduce uncertainty when the value is used in estimating applied water.

Secondly, the accuracy of the applied water estimate is subject to the uncertainty of evapotranspiration estimates and other input variables. We found that our annual evapotranspiration rate is higher than the crop coefficients based estimates at many apple orchards sites. As the derived application efficiency value is constrained with a maximum of 0.99, an overestimation of evapotranspiration is likely responsible for the overestimation of pumping at apple orchard fields (figure 6a). Future studies should consider employing a crop specifically calibrated version of PT-UCD to reduce the uncertainty of crop evapotranspiration estimates, and further investigate whether remote sensing approaches could accurately estimate the variability of daily evapotranspiration due to microclimates, irrigations, and fogs. Besides the uncertainty of evapotranspiration, additional information of individual fields, such as irrigation method and orchard age, could further reduce the uncertainty of field-scale water balance.

At last, the quantity and quality of survey data, specifically the place of use areas for individual wells, is a major bottleneck of this study. Lin et al., (2013) rely on verbal interviews to identify the place of use areas for individual growers. Instead of drawing the specific place of

use, the survey only recorded the field IDs from PVWMA's land use map. The land use maps were manually produced and the field boundaries are subject to errors. For example, the place of use area information could be incomplete or inaccurate, because wells are sometimes co-operated among growers and some field polygons on the land use map should be further subdivided to reflect different land ownership and management practices. To support future field-scale water use studies, water agencies could consider adopting an online groundwater extraction platform similar to the one developed by the State Water Resources Control Board (SWRCB) (Vanderburgh, 2018). The platform enables growers to digitally report pumping and to map the corresponding place of use, and their database could potentially be used for future field-scale water use research.

4.2 Regional applied water estimates

While the proposed field-scale water accounting method requires more data, research, and evaluation, our regional pumping estimate is comparable to PVHM. PVHM requires calibration of crop and subregion specific application efficiency parameters using subregional total pumping data, and our estimates only used field pumping measurements from 94 fields and calibrated a single parameter. At the annual time scale for zonal estimates, we found a good agreement between the two water balances in terms of precipitation, applied water, evapotranspiration, and other combined outflows. However, further investigation is needed for comparisons in a longer time period (e.g. 2003 to present) and at quarterly and monthly intervals.

Our results showed that the zonal estimates of PVHM are more accurate than our estimates, but PVHM's success at the zonal scale is largely contributed by zonal specific calibration of application efficiency using zonal total pumping measurements. This makes the

approach difficult to replicate in other agricultural regions of California. Therefore, our approach (not the implemented model on python, but the general approach which can implemented any groundwater model), although having much room for improvement, is a promising alternative for estimating zonal and GSA scale agricultural water use in areas with limited pumping data.

4.3 Implications for water resource management

Our relatively simple soil water balance approach could not explain some variability in pumping at a field and zonal scale. An RMSE of 40 million liters (figure 6a) is equivalent to 32 acre-feet, which could worth $46,000 of surface water during droughts in some parts of California. Therefore, we agree with SWRCB's decision that remote sensing evapotranspiration should not be used directly to infer total groundwater extraction of individual fields unless significant additional information relating to agricultural practices and field conditions is provided (California State Water Resources Control Board, 2020). At Rosedale-Rio Bravo Water Storage District, a pilot field-scale water accounting framework is being conducted. Their approach of charging fees on groundwater pumping, which is solely based on remote sensing evapotranspiration estimation, could be problematic.

Our research suggests that accurate regional applied water could be estimated by coupling field-scale, daily, remote sensing evapotranspiration estimates with a soil water balance model. However, water managers may hesitate to adopt remote sensing techniques. It is because using remote sensing techniques in regional water budgets also made the evaluation of the model at a field scale possible, but the field-scale estimates, which may be accurate when spatial-temporally aggregated at local GSA scale, may not agree with field measurements. This scaling

issue is common among remote sensing applications (Wu & Li, 2009), but understanding and addressing the issue will require extensive research.

4.4 Other Potential improvements

The research here could serve as a cornerstone for future research. Besides gathering more data and test cases from farms and agencies across the western United States, as well as implementing this approach using other well-established remote sensing evapotranspiration estimates, we seek to further improve the design and accuracy of modeling agricultural applied water. In this study, we implemented a soil water balance model from scratch and conducted the study as a proof of concept. The modeling approach - deriving crop-specific field-scale application efficiency using remote sensing evapotranspiration and pumping data, and using the summarized application efficiency values for regional spatial applied water estimates - can be implemented in many other well-established soil water balance models, such as the IDC. IDC has been integrated with groundwater model, enabling enables calibration of the hydrological model with fluctuations of groundwater level and streamflow observations. The coupled hydrological model may also enable the possibility for deriving local application water use efficiency with fewer field pumping data.

5 Conclusions

Our approach showed great promises of using remote sensing evapotranspiration for consistent and accurate field-scale water accounting. It demonstrated the capability for estimating regional applied water within 4.6% in 2009 and 2011 over the Pajaro Valley using a limited quantity of field pumping measurements (from 94 fields across four major crop classes). We also identified challenges and problems of using remote sensing evapotranspiration for water

budget from field to regional scales. Before the development of remote sensing evapotranspiration techniques, outflow fluxes of a zonal water balance, namely evapotranspiration, runoff, and percolation, were nearly impossible to verify. Our modeling approach allows researchers to utilize field data, such as soil moisture, evapotranspiration, and soil type, to validate the water balance at a field scale, which could be further aggregated to a subregional scale for resource management purposes. This approach unifies field-scale and regional-scale water accounting, enabling local groundwater agencies to bill growers for pumping groundwater, to develop local water budgets and sustainability plans, and to work with nearby agencies to co-manage a groundwater basin by using a single model. With future research, our proposed model could be an all-in-one integrated solution to many problems that local agencies are facing today.

Acknowledgments

Support for this project was provided by NASA AmericaView and California's Space Grant. We especially thank Pajaro Valley Water Management Agency and Samuel Sandoval Solis for sharing the field survey records, land use and pumping data, and insights and recommendations.

References

Anderson, M. C., Allen, R. G., Morse, A., & Kustas, W. P. (2012). Use of Landsat thermal imagery in monitoring evapotranspiration and managing water resources. *Remote Sensing of Environment, 122*, 50–65. https://doi.org/10.1016/j.rse.2011.08.025

Anderson, M. C., Gao, F., Knipper, K., Hain, C., Dulaney, W., Baldocchi, D., et al. (2018). Field-Scale Assessment of Land and Water Use Change over the California Delta Using Remote Sensing. *Remote Sensing, 10*(6), 889. https://doi.org/10.3390/rs10060889

Brady, N. C., & Weil, R. R. (1999). The nature and properties of soil 12th ed. *Mac. Pub. Com. New York*, 625–640.

California Department of Water Resources. (2014). *California Water Plan Update 2013 Vol. 1*. California Department of Water Resources.

California Department of Water Resources. (2017). Frequently Asked Questions on Integrated Hydrologic Modeling and Water Budgets pertaining to the Sustainable Groundwater Management Act and Groundwater Sustainability Plan Regulations.

California Department of Water Resources. (2019). SGMA Groundwater Management. Retrieved May 20, 2019, from http://water.ca.gov/Programs/Groundwater-Management/SGMA-Groundwater-Management

California Department of Water Resources. (2020). IDC: Integrated Water Flow Model Demand Calculator. Retrieved February 26, 2021, from http://water.ca.gov/Library/Modeling-and-Analysis/Modeling-Platforms/Integrated-Water-Flow-Model-Demand-Calculator

California State Water Resources Control Board. (2020, October 8). Options for Measuring Extraction Volumes. Retrieved from https://www.waterboards.ca.gov/water_issues/programs/sgma/docs/reporting/measure20.pdf

California Strawberry Commission. (2021, December). 2021 Acreage Survey. Retrieved February 24, 2021, from https://www.calstrawberry.com/en-us/Market-Data/Acreage-Survey

City of Watsonville. (2009). Economic Profile | Watsonville. Retrieved February 26, 2021, from https://www.cityofwatsonville.org/932/Economic-Profile

Cuenca, R. H., Ciotti, S. P., & Hagimoto, Y. (2013). Application of Landsat to Evaluate Effects of Irrigation Forbearance. *Remote Sensing*, *5*(8), 3776–3802. https://doi.org/10.3390/rs5083776

Devine, S., & O'Geen, A. T. (2019). Climate-smart management of soil water storage: statewide analysis of California perennial crops. *Environmental Research Letters*, *14*(4), 044021.

Escriva-Bou, A., McCann, H., Hanak, E., Lund, J., & Gray, B. (2016). *Accounting for California's Water* (p. 30). Public Policy Institute of California. Retrieved from https://www.ppic.org/content/pubs/report/R_716EHR.pdf

Faunt, C. C., Sneed, M., Traum, J., & Brandt, J. T. (2016). Water availability and land subsidence in the Central Valley, California, USA. *Hydrogeology Journal*, *24*(3), 675–684. https://doi.org/10.1007/s10040-015-1339-x

Fisher, J. B. (2008). *Evapotranspiration Model (PT-JPL): MATLAB for spatial arrays*. Retrieved from http://josh.yosh.org/

Garza-Díaz, L. E., DeVincentis, A. J., Sandoval-Solis, S., Azizipour, M., Ortiz-Partida, J. P., Mahlknecht, J., et al. (2019). Land-Use Optimization for Sustainable Agricultural Water Management in Pajaro Valley, California. *Journal of Water Resources Planning and Management*, *145*(12), 05019018. https://doi.org/10.1061/(ASCE)WR.1943-5452.0001117

Hanak, E., Lund, J., Arnold, B., Escriva-Bou, A., Gray, B., Green, S., et al. (2017). Water stress and a changing San Joaquin Valley. *Public Policy Institute of California*, *1*, 5–48.

Hanson, R. T., Schmid, W., Faunt, C. C., Lear, J., & Lockwood, B. (2014). *Integrated hydrologic model of Pajaro Valley, Santa Cruz and Monterey Counties, California* (USGS Numbered Series No. 2014–5111). *Integrated hydrologic model of Pajaro Valley, Santa Cruz and Monterey Counties, California* (Vol. 2014–5111, p. 180). Reston, VA: U.S. Geological Survey. https://doi.org/10.3133/sir20145111

Hart, Q. J., Brugnach, M., Temesgen, B., Rueda, C., Ustin, S. L., & Frame, K. (2009). Daily reference evapotranspiration for California using satellite imagery and weather station measurement interpolation. *Civil Engineering and Environmental Systems*, *26*(1), 19–33. https://doi.org/10.1080/10286600802003500

Harter, T., & Morel-Seytoux, H. (2013). Peer Review of the IWFM, MODFLOW and HGS Model Codes: Potential for Water Management Applications in California's Central Valley and Other Irrigated Groundwater Basins, 121.

He, R., Jin, Y., Kandelous, M., Zaccaria, D., Sanden, B., Snyder, R., et al. (2017). Evapotranspiration estimate over an almond orchard using landsat satellite observations. *Remote Sensing*, *9*(5), 436.

Macaulay, L., & Butsic, V. (2017). Ownership characteristics and crop selection in California cropland. *California Agriculture*, *71*(4), 221–230.

Maples, S. R. (2019). *Simulating Recharge Processes and Evaluating Groundwater Budget Estimates in California's Central Valley Aquifer System* (Ph.D.). University of California, Davis, United States -- California. Retrieved from https://search.proquest.com/docview/2384870238/abstract/F0DF6B580BF84987PQ/1

Martínez-Santos, P., & Martínez-Alfaro, P. E. (2010). Estimating groundwater withdrawals in areas of intensive agricultural pumping in central Spain. *Agricultural Water Management*, *98*(1), 172–181. https://doi.org/10.1016/j.agwat.2010.08.011

McCauley, A., Jones, C., & Jacobsen, J. (2005). Basic soil properties. *Soil and Water Management Module*, *1*(1), 1–12.

O'Geen, A. T. (2012). Soil water dynamics. *Nature Education Knowledge*, *3*(6), 12.

O'Geen, T. (n.d.). Soil Properties. Retrieved February 26, 2021, from https://casoilresource.lawr.ucdavis.edu/soil-properties/

Schmid, W., & Hanson, R. T. (2009). *The Farm Process version 2 (FMP2) for MODFLOW-2005: modifications and upgrades to FMP1*. US Geological Survey California Water Science Center.

Schmid, W., Dogrul, E., Hanson, R., Kadir, T., & Chung, F. (2011). *Comparison of Simulations of Land-use Specific Water Demand and Irrigation Water Supply by MF-FMP and IWFM*.

Sinclair Knight Merz & National Centre for Groundwater Research and Training. (2012). Australian groundwater modelling guidelines. Canberra, ACT.: National Water Commission.

Smith, S. (2015, December 28). Damage From Sinking Land Costing California Billions in Infrastructure Repairs. *NBC Bay Area*. Retrieved from https://www.nbcbayarea.com/news/local/damage-from-sinking-land-costing-california-billions-in-infrastructure-repairs/122810/

Snyder, R. L., Geng, S., Orang, M., & Sarreshteh, S. (2012). Calculation and Simulation of Evapotranspiration of Applied Water. *Journal of Integrative Agriculture*, *11*(3), 489–501. https://doi.org/10.1016/S2095-3119(12)60035-5

Sustainable Groundwater Management Office. (2020). *C2VSimFG Version 1.0*. Retrieved from https://data.cnra.ca.gov/dataset/c2vsimfg-version-1-0

Thornton, P. E., Thornton, M. M., Mayer, B. W., Wei, Y., Devarakonda, R. S., Vose, R. S., & Cook, R. B. (2017). *Daymet: Daily Surface Weather Data on a 1-km Grid for North America, Version 3 ORNL DAAC Oak Ridge Tenn*. USA.

Vanderburgh, B. (2018, March). *Groundwater Extraction Annual Reporting System (GEARS)*. Retrieved from https://www.waterboards.ca.gov/resources/data_databases/data_fair/docs/gears_df.pdf

Wu, H., & Li, Z.-L. (2009). Scale Issues in Remote Sensing: A Review on Analysis, Processing and Modeling. *Sensors*, *9*(3), 1768–1793. https://doi.org/10.3390/s90301768

Chapter 4: Concluding Remarks

California is one of the world's most productive agricultural regions. However, agricultural activities are sustained by over-drafting 1.2-2.5 trillion liters of groundwater per year (California Department of Water Resources, 2014). A key challenge to the sustainable management of groundwater is that the majority of groundwater pumping activities are not metered or reported to the Groundwater Sustainability Agencies (GSAs). This creates difficulties in establishing a billing structure for deterring excessive use and gathering funding for management operations and infrastructure investments. Without field measurements of agricultural groundwater use, agencies are uncertain about their estimates of local water demand. Their best estimate, based on various assumptions and modelings of the hydrological process, and calibrated with the best available data, could be inaccurate, thus potentially misinforming management decisions. Maples (2019) found that the subregional pumping estimates in the Central Valley, between USGS's and California Department of Water Resources' (DWR) groundwater models, have an average discrepancy of 63% or 271 billion liters per year. This discrepancy creates opportunities for self-organized local GSAs to pick whichever estimates that best fit their agenda. As a result, DWR had to devote enormous effort to review and approve GSAs' water plans. All these problems in implementing sustainable groundwater management begin with a lack of field-scale water use records. While requiring metering of all pumping activities is expensive and politically challenging to implement, remote sensing of evapotranspiration could provide spatial estimates of agricultural water use at a field scale.

Broadly, this dissertation demonstrates that remote sensing evapotranspiration is well suited for water resource management in California. Chapter 1 presented an improved model for estimating daily crop evapotranspiration at 30m resolution. The refined semi-empirical Priestley-

Taylor approach, after optimizing the actual Priestley Taylor coefficient as a function of LAI and moisture index with recently compiled ground measurements of evapotranspiration for California's major crops, can accurately capture the temporal and spatial variability of crop water consumptive uses. The daily evapotranspiration, directly estimated during satellite overpassing days under clear-sky and interpolated for other days, agreed well with the field measurements, with an R^2 of 0.78 and an RMSE of 0.95 mm day^{-1}.

After evaluating the uncertainty of a remote sensing evapotranspiration estimate in Chapter 1, the dissertation further provided two specific applications of spatial evapotranspiration estimates in water resources management. The first application, as exemplified by Chapter 2, is to assess the pattern of evapotranspiration estimates to understand the what, when, where, and how crops are consuming water from field to regional scales. Based on the analysis of our estimates over the Central Valley, we found that the crop evapotranspiration rate averaged at 820 mm yr^{-1} and had a large spatial variability with a standard deviation of 290 mm yr^{-1} over all agricultural pixels in 2014. Compared to 2014, total water use in 2016 increased by 9.6%, mostly as a result of land-use conversion (2370 km^2) from fallow/idle land in 2014 to cropland in 2016. When aggregated by the GSA boundaries, the annual evapotranspiration rate showed large variation among GSAs, i.e., $\overline{x}$ = 803, σ = 154 mm $yr^{-1,}$ and a CV of 19% in 2014. This variability was mostly associated with variation in net radiation and actual Priestley Taylor coefficient or fraction of reference evapotranspiration, driven by crop type diversity and conditions. Perennial crops such as pistachios and almonds typically had much higher variability within and among GSAs than annual crops. Many other insights regarding crop water use in the Central Valley are provided in Chapter 2. Overall, we provided more realistic estimates of crop coefficient and evapotranspiration for local water

budget accounting, evaluation of crop water use variation within and among GSAs, and highlighted the importance of crop planning, orchard age structure, and other physiological stressors such as salinity on the trajectory of local orchard water use and demand.

The second application of spatial evapotranspiration estimates in water resources management, as demonstrated in Chapter 3, is coupling evapotranspiration estimates with a soil water model to estimate agricultural water use from the field to regional scales. The study demonstrated the capability for estimating regional applied water within 4.6% in 2009 and 2011 over the Pajaro Valley using a limited quantity of field pumping measurements (from 94 fields across four major crop classes). Before the development of remote sensing evapotranspiration techniques, outflow fluxes of a zonal water balance, namely evapotranspiration, runoff, and percolation, were nearly impossible to verify. Our modeling approach allows researchers to utilize field data, such as soil moisture, evapotranspiration, and soil type, to verify the water fluxes at a field scale, which could be further aggregated to subregional scale for resource management purposes. The proposed approach unifies field-scale and regional-scale water accounting, enabling local groundwater agencies to bill growers for pumping groundwater, to develop local water budgets and sustainability plans, and to work with nearby agencies to co-manage a groundwater basin by using a single model.

While the dissertation research was implemented in the Central Valley and Pajaro Valley of California, the presented tools and methods are broadly applicable to other semi-arid, agriculturally-dominated regions. With future research and collaboration, the application of remote sensing evapotranspiration could provide solutions to many problems that water resources management agencies are facing today.

Appendices

Supporting tables and figures, and additional analysis for the dissertation research are included here. The additional analysis includes a sensitivity analysis of equations in PT-UCD, a proposed modification of PT-UCD using Penman-Monteith, an investigation of orchard age and salinity on PT-UCD's remote sensing input variables and estimates, and a study comparing evapotranspiration estimates between PVHM and PT-UCD.

Appendix I: Supporting Materials of Chapter I

Text S1.

PT-JPL was implemented in our study to estimate evapotranspiration at all measurement sites. It serves as a baseline for quantifying the accuracy of PT-UCD. Unlike PT-UCD, PT-JPL is a dual-source energy balance model. Latent heat flux from canopy and soil were estimated separately.

$$LE = \alpha_s \frac{\Delta}{\Delta+\gamma} R_{ns} + \alpha_c \frac{\Delta}{\Delta+\gamma} R_{nc} \quad \text{(S1)}$$

The subscript s and c represent soil and canopy, respectively. R_n were partitioned into soil net radiation with a ratio of $exp\ exp\ (-0.6 * LAI)$. PT-coefficient for soil and canopy is estimated with the following equations,

$$\alpha_s = \left((1 - RH^4) * (RH^{VPD}) + RH^4\right)1.26 \quad \text{(S2)}$$

$$\alpha_c = (1 - RH^4) * \frac{1.14}{1+e^{2\left(T_{opt}-Ta-10\right)}} * \frac{fApar}{NDVI-0.05} * \frac{fApar}{fApar_{max}} + RH^4)1.26 \quad \text{(S3)}$$

$$fApar = 1.2 * 1.136 * SAVI + (1.2 * -0.04) \quad \text{(S4)}$$

, where RH is relative humidity and VPD is vapor pressure deficit. Both RH and VPD are computed from CIMIS Spatial's dew point temperature and T_a. Soil adjusted vegetation indices,

SAVI, are 0.45(NDVI)+0.132. T_{opt} is T_a on clear-sky Landsat overpassing date that has the maximum value of $Rn * T_a * \frac{SAVI}{VPD}$. To determine T_{opt} and $fApar_{max}$ of each Landsat pixel, a full calendar year of remote sensing and meteorological input data time series were used. To compare PT-JPL with PT-UCD, we estimated PT-JPL daily evapotranspiration and then back-calculated the equivalent PT coefficient with the single source latent heat flux equation (Equation 1 from Chapter 1).

Table S1. Statistics of Priestley Taylor Coefficient Parameters for the three cross-validation approach as outlined in section 2.4. Holdout cross-validation result is based on one-time random partitioning of training and testing data, with sites 2, 14, 25, and 26 reserved for independent validation.

$$PT_a = (A - C * e^{-B*LAI}) * (D * (NDMI + 1) + E) * f(T_a)$$

Cross-Validation Versions	**Parameters**	**A**			**B**			**C**		
	Crop	median	mean	Standard Deviation	median	mean	Standard Deviation	median	mean	Standard Deviation
Holdout	Generalized	N/A	1.300	N/A	N/A	0.900	N/A	N/A	1.200	N/A
Repeated		1.300	1.300	0.000	0.900	0.900	0.000	1.200	1.200	0.000
Leave-2-out		1.300	1.299	0.011	0.900	0.900	0.004	1.200	1.201	0.009
Holdout	Alfalfa	N/A	1.200	N/A	N/A	0.800	N/A	N/A	1.300	N/A
Repeated		1.265	1.270	0.052	0.800	0.807	0.024	1.191	1.204	0.061
Leave-2-out		1.265	1.261	0.042	0.800	0.811	0.027	1.192	1.201	0.051
Holdout	Almond	N/A	1.400	N/A	N/A	0.941	N/A	N/A	1.100	N/A
Repeated		1.400	1.350	0.073	0.800	0.870	0.089	1.100	1.150	0.078
Holdout	Citrus	N/A	1.400	N/A	N/A	1.000	N/A	N/A	1.100	N/A

Repeated		1.400	1.400	0.000	1.000	1.000	0.000	1.100	1.100	0.000
Holdout	Corn	N/A	1.400	N/A	N/A	0.800	N/A	N/A	1.100	N/A
Repeated		1.400	1.399	0.006	0.800	0.850	0.086	1.100	1.101	0.006
Leave-2-out		1.400	1.397	0.008	0.800	0.867	0.096	1.100	1.117	0.034
Holdout	Pasture	N/A	1.400	N/A	N/A	1.000	N/A	N/A	1.100	N/A
Repeated		1.400	1.395	0.024	1.000	1.000	0.000	1.100	1.104	0.024
Holdout	Rice	N/A	1.400	N/A	N/A	1.000	N/A	N/A	1.100	N/A
Repeated		1.400	1.400	0.000	1.000	1.000	0.002	1.100	1.100	0.000

Versions	**Parameters**	**D**			**E**		
	Crop	median	mean	Standard Deviation	median	mean	Standard Deviation
Holdout	Generalized	N/A	0.352	N/A	N/A	0.511	N/A
Repeated		0.335	0.335	0.063	0.535	0.535	0.080
Leave-2-out		0.327	0.331	0.064	0.541	0.539	0.083
Holdout	Alfalfa	N/A	0.124	N/A	N/A	0.853	N/A
Repeated		0.227	0.224	0.051	0.637	0.641	0.093
Leave-2-out		0.241	0.232	0.063	0.616	0.639	0.107
Holdout	Almond	N/A	0.665	N/A	N/A	0.049	N/A
Repeated		0.569	0.559	0.128	0.212	0.250	0.225
Holdout	Citrus	N/A	0.111	N/A	N/A	0.706	N/A
Repeated		0.060	0.064	0.056	0.768	0.762	0.068
Holdout	Corn	N/A	0.509	N/A	N/A	0.096	N/A
Repeated		0.378	0.379	0.042	0.263	0.258	0.059
Leave-2-out		0.372	0.417	0.108	0.267	0.206	0.135
Holdout	Pasture	N/A	0.000	N/A	N/A	0.888	N/A
Repeated		0.000	0.036	0.054	0.872	0.843	0.070
Holdout	Rice	N/A	0.335	N/A	N/A	0.573	N/A
Repeated		0.314	0.312	0.072	0.611	0.613	0.097

Table S2. R2, RMSE, and MAE, and best-fit-line coefficients of net radiation and evapotranspiration estimates for training and testing data during holdout cross-validation.

Crop types	**Net Radiation**									
	Training					Testing				
	R2	RMSE	MAE	Slope	y-Intercept	R2	RMSE	MAE	Slope	y-Intercept
Alfalfa	0.78	21.10	15.77	0.94	7.92	0.84	20.54	15.68	0.89	12.32
Almond	0.82	23.83	16.39	0.94	7.71	0.80	26.54	18.23	1.00	1.68
Citrus	0.56	24.64	20.39	0.72	52.94	0.74	18.85	15.05	1.02	4.02

Corn	0.37	29.88	23.94	0.81	39.49	0.67	27.25	22.26	0.93	3.12
Others	N/A	N/A	N/A	N/A	N/A	0.48	24.50	21.84	1.10	-9.59
Pasture	0.81	17.35	12.77	1.04	2.83	0.81	17.34	15.00	1.03	10.53
Rice	0.53	37.71	32.60	0.95	35.82	0.39	39.70	35.63	1.03	22.37
Crop types	**Generalized Estimates of Evapotranspiration**									
	Training					Testing				
	R2	RMSE	MAE	Slope	y-Intercept	R2	RMSE	MAE	Slope	y-Intercept
Alfalfa	0.80	0.69	0.53	0.89	0.48	0.75	0.79	0.61	0.99	0.42
Almond	0.82	1.03	0.74	0.86	0.26	0.84	1.01	0.72	0.90	0.09
Citrus	0.70	0.65	0.53	1.05	-0.25	0.36	0.99	0.72	1.05	-0.23
Corn	0.55	1.24	0.99	0.97	0.96	0.58	1.15	0.91	1.02	0.45
Others	N/A	N/A	N/A	N/A	N/A	0.71	1.11	0.95	1.13	0.72
Pasture	0.63	1.00	0.77	0.69	1.18	0.74	0.75	0.58	0.76	1.07
Rice	0.85	0.87	0.69	0.99	0.14	0.77	1.12	0.90	0.92	0.28
Crop types	**Crop-Specific Estimates of Evapotranspiration**									
	Training					Testing				
	R2	RMSE	MAE	Slope	y-Intercept	R2	RMSE	MAE	Slope	y-Intercept
Alfalfa	0.83	0.65	0.51	0.85	0.45	0.82	0.68	0.53	0.92	0.42
Almond	0.84	0.95	0.67	0.92	0.14	0.86	0.94	0.66	0.96	-0.04
Citrus	0.74	0.62	0.51	0.98	0.03	0.56	0.83	0.65	1.02	-0.10
Corn	0.80	0.83	0.69	0.91	0.51	0.71	0.96	0.76	0.91	0.17
Others	N/A	N/A	N/A	N/A	N/A	N/A	N/A	N/A	N/A	N/A
Pasture	0.69	0.91	0.69	0.70	1.31	0.72	0.77	0.64	0.75	1.29
Rice	0.71	1.20	1.04	1.09	0.43	0.67	1.34	1.10	1.01	0.57

Table S3. Comparison of annual evapotranspiration estimates averaged over different footprint window sizes.

Site ID	**Year**	**Pixel Window**								
		1x1	3x3				11x11			
		Mean	Mean	Std	CV	% Difference	Mean	Std	CV	% Difference
1	2014	2.45	2.50	0.06	2.5%	2.2%	2.52	0.12	4.8%	3.1%
24	2014	3.38	3.38	0.02	0.7%	0.0%	3.26	0.21	6.5%	-3.6%
1	2016	2.36	2.35	0.03	1.1%	-0.5%	2.32	0.09	3.8%	-1.7%
2	2016	2.61	2.60	0.02	0.9%	-0.5%	2.54	0.06	2.5%	-2.8%
3	2016	2.62	2.60	0.03	1.1%	-0.8%	2.54	0.31	12.3%	-2.7%
4	2016	2.97	2.97	0.03	1.0%	0.1%	2.71	0.31	11.4%	-8.5%
5	2016	2.53	2.51	0.04	1.5%	-0.8%	2.46	0.07	2.9%	-2.6%
6	2016	2.43	2.37	0.08	3.5%	-2.2%	2.23	0.25	11.0%	-8.3%
7	2016	2.38	2.38	0.04	1.8%	-0.1%	2.38	0.10	4.3%	0.0%
15	2016	1.76	1.76	0.02	1.1%	0.0%	1.77	0.06	3.4%	0.6%
16	2016	2.10	2.06	0.10	4.8%	-2.3%	1.89	0.19	10.0%	-10.1%
17	2016	1.74	1.73	0.03	1.5%	-0.4%	1.75	0.10	5.7%	0.6%
18	2016	1.95	1.89	0.06	3.2%	-3.2%	1.89	0.18	9.3%	-3.2%
19	2016	1.83	1.79	0.11	6.1%	-2.0%	1.88	0.15	8.0%	2.4%
20	2016	3.03	3.04	0.02	0.6%	0.1%	2.96	0.32	10.7%	-2.4%

21	2016	2.99	3.03	0.03	1.1%	1.2%	3.04	0.11	3.5%	1.6%
22	2016	3.02	3.03	0.07	2.4%	0.3%	2.97	0.41	13.6%	-1.6%
23	2016	2.48	2.44	0.04	1.6%	-1.8%	2.34	0.15	6.6%	-6.0%
24	2016	2.99	2.90	0.14	4.8%	-3.0%	2.90	0.19	6.4%	-3.2%
25	2016	1.88	1.89	0.04	1.9%	0.9%	1.89	0.06	3.3%	0.9%
26	2016	1.44	1.44	0.01	0.7%	-0.2%	1.46	0.03	2.1%	0.9%

Site ID	**Year**	**Pixel Window**								
		1x1	17x17				33x33			
		Mean	Mean	Std	CV	% Difference	Mean	Std	CV	% Difference
1	2014	2.45	2.51	0.16	6.2%	2.8%	2.34	0.31	13.4%	-4.3%
24	2014	3.38	3.13	0.37	11.7 %	-7.4%	2.95	0.45	15.3%	-12.9%
1	2016	2.36	2.39	0.13	5.3%	1.4%	2.47	0.34	13.8%	4.4%
2	2016	2.61	2.51	0.19	7.6%	-3.8%	2.38	0.44	18.4%	-8.8%
3	2016	2.62	2.43	0.32	13.3 %	-7.0%	2.33	0.37	15.9%	-11.0%
4	2016	2.97	2.67	0.28	10.4 %	-10.1%	2.61	0.25	9.5%	-12.0%
5	2016	2.53	2.31	0.31	13.3 %	-8.6%	1.92	0.76	39.6%	-23.9%
6	2016	2.43	2.23	0.25	11.1 %	-8.4%	2.11	0.36	17.0%	-13.2%
7	2016	2.38	2.43	0.15	6.4%	2.1%	2.53	0.35	13.7%	6.5%
15	2016	1.76	1.76	0.08	4.6%	-0.3%	1.89	0.29	15.5%	7.3%
16	2016	2.10	1.89	0.25	13.5 %	-10.3%	1.58	0.58	36.9%	-24.9%
17	2016	1.74	1.81	0.23	12.6 %	4.0%	1.89	0.46	24.1%	8.8%
18	2016	1.95	1.90	0.18	9.5%	-2.7%	1.87	0.49	26.5%	-4.4%
19	2016	1.83	1.88	0.17	9.0%	2.7%	1.89	0.16	8.6%	3.2%
20	2016	3.03	2.78	0.50	18.0 %	-8.4%	2.52	0.61	24.1%	-16.8%
21	2016	2.99	2.99	0.24	8.0%	-0.2%	2.45	0.90	36.8%	-18.0%
22	2016	3.02	2.80	0.55	19.7 %	-7.3%	2.44	0.52	21.3%	-19.2%
23	2016	2.48	2.35	0.23	9.7%	-5.5%	2.42	0.37	15.3%	-2.7%
24	2016	2.99	2.85	0.23	8.0%	-4.8%	2.90	0.36	12.5%	-3.2%
25	2016	1.88	1.89	0.07	3.5%	0.5%	1.86	0.23	12.2%	-0.8%
26	2016	1.44	1.50	0.10	6.8%	4.0%	1.75	0.43	24.8%	21.0%

Table S5. Comparison of daily evapotranspiration estimates from three PT approaches with field measurements during days with clear-sky Landsat observations and other days (from temporal interpolation). Results from generalized PT-UCD were not shown for individual crop types.

Crop types	n				
	Clear Sky Overpassing Days			Interpolated	All Days
	Testing	Independent	All		
Alfalfa	159	111	370	3500	3870
Almond	27	N/A	102	1303	1405
Citrus	13	N/A	41	445	486
Corn	104	82	165	1492	1657
Others	21	21	21	193	214
Pasture	19	N/A	86	611	697
Rice	46	N/A	212	2697	2909
All (Generalized)	389	214	997	10241	11238
All (Crop Specific)	368	193	976	10048	11024

Crop types	R^2										
	Clear Sky Overpassing Days									Interpolated	All Days
	Testing			Independent			All				
	PT-0	JPL	UCD	PT-0	JPL	UCD	PT-0	JPL	UCD		
Alfalfa	0.57	0.71	0.82	0.55	0.71	0.81	0.64	0.69	0.83	0.76	0.76
Almond	0.78	0.53	0.86	N/A	N/A	N/A	0.78	0.48	0.85	0.89	0.88
Citrus	0.24	< 0	0.56	N/A	N/A	N/A	0.39	-0.21	0.70	0.70	0.70
Corn	0.11	0.70	0.71	< 0	0.70	0.65	0.18	0.72	0.75	0.68	0.69
Others	< 0	0.70	N/A	- -	- -	N/A	- -	- -	N/A	N/A	N/A
Pasture	0.66	0.36	0.72	N/A	N/A	N/A	0.75	0.42	0.77	0.69	0.71
Rice	0.77	0.71	0.67	N/A	N/A	N/A	0.80	0.80	0.75	0.77	0.77
All (Generalized)	0.57	0.71	0.76	0.30	0.72	0.68	0.68	0.70	0.80	0.78	0.79
All (Crop Specific)	N/A	N/A	0.79	N/A	N/A	0.75	N/A	N/A	0.81	0.80	0.80

Crop types	RMSE (mm day^{-1})										
	Clear Sky Overpassing Days									Interpolated	All Days
	Testing			Independent			All				
	PT-0	JPL	UCD	PT-0	JPL	UCD	PT-0	JPL	UCD		
Alfalfa	1.05	0.86	0.68	1.10	0.88	0.72	0.94	1.11	0.65	0.77	0.76
Almond	1.18	1.72	0.94	N/A	N/A	N/A	1.13	0.87	0.95	0.86	0.86
Citrus	1.08	1.48	0.83	N/A	N/A	N/A	0.99	1.73	0.69	0.86	0.84
Corn	1.66	0.97	0.96	1.55	0.85	0.91	1.65	1.39	0.91	1.01	1.00
Others	2.12	1.14	N/A	- -	- -	N/A	- -	- -	N/A	N/A	N/A
Pasture	0.86	1.18	0.77	N/A	N/A	N/A	0.86	1.31	0.82	0.94	0.93
Rice	1.11	1.25	1.34	N/A	N/A	N/A	1.03	1.03	1.16	1.09	1.09
All (Generalized)	1.32	1.08	0.98	1.41	0.90	0.95	1.15	1.11	0.91	0.95	0.95
All (Crop Specific)	N/A	N/A	0.90	N/A	N/A	0.80	N/A	N/A	0.87	0.93	0.92

Table S6. Evaluation of outgoing longwave radiation estimates over sites 2, 14, 25, and 26, which were exclusively used for testing.

Validation Data	n	R^2	Bias (W/m^2)	MAE (W/m^2)	RMSE (W/m^2)	MAPE (%)	RMAD (%)
Everything	244	0.73	6.68	17.14	21.19	4.19	4.16
Alfalfa	111	0.73	8.82	14.09	17.28	3.56	3.53
Corn	82	0.46	11.2	19.27	24.05	4.81	4.73
Others	51	0.72	-5.22	20.36	23.84	4.57	4.55

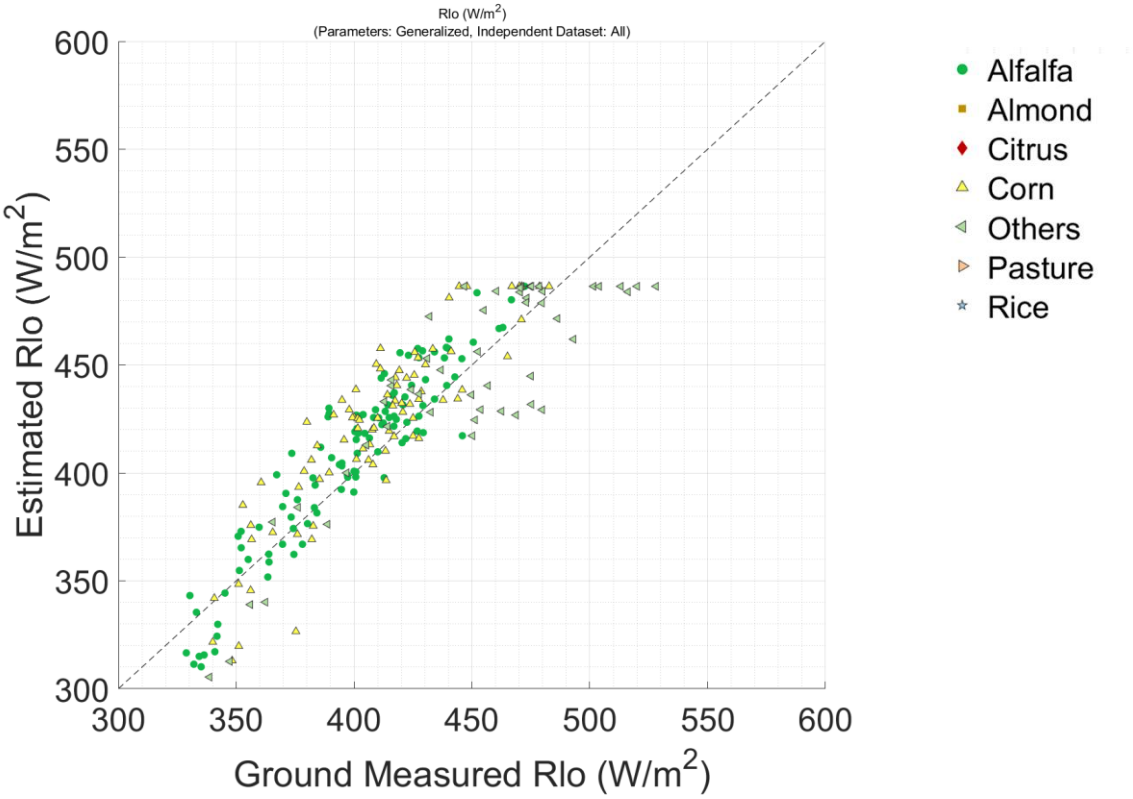

Figure S1. Evaluation of outgoing longwave radiation estimates over sites 2, 14, 25, and 26, which were exclusively used for testing.

Appendix II: Improving PT-UCD

The author has no plan on publishing this research at the moment. However, the ideas and works presented here have tremendous value for developing a more sophisticated Priestley-Taylor-driven evapotranspiration model. For example, a neural network could be trained to predict the actual Priestley Taylor coefficient, using net radiation, vapor pressure deficit, and aerodynamic (r_a) and canopy surface (r_c) resistances. And trained model could be compared with the partial derivative of the Priestley Taylor coefficient equation presented here. Finally, the model can be extended to using satellite observations instead of resistances values as model inputs.

The Priestley Taylor equation (Eq. 1) has been adapted by remote sensing scientists to estimate actual evapotranspiration (Fisher et al., 2008; Jin et al., 2011). With remote sensing, the Priestley Taylor coefficients are often estimated with vegetation and moisture-related indices. Despite their accuracy in estimating evapotranspiration, the remote sensing driven Priestley Taylor models lack a theoretical basis in relating remote sensing indices with the Priestley Taylor coefficient (PT_a). Here, we propose that the Priestley Taylor coefficient could be expressed in terms of aerodynamic (r_a) and canopy surface (r_c) resistances by equating the Penman Monteith equation (Eq. 2) with the Priestley Taylor equation.

$$LE = PT_a * \frac{\Delta}{\Delta+\gamma} * (R_n - G) \quad (1)$$

$$LE = (\Delta * (R_n - G) + (\rho * C_p * \delta e / r_a))/(\Delta + \gamma * (1 + r_c/r_a)) \quad (2)$$

The Priestley Taylor equation can be interpreted as a simplified form of Penman-Monteith, first by assuming an equilibrium condition, where vapor pressure deficit (δe) and canopy surface resistance (r_c) are zero, then by scaling the equilibrium evapotranspiration with a

Priestley Taylor coefficient (PT_a), to estimate evapotranspiration of an extensive wet surface in the absence of advection (Eichinger et al., 1996).

Besides the empirical approach of estimating the Priestley Taylor coefficient, few have explored the derivation of the coefficient by equating the Priestley Taylor equation with other evapotranspiration estimation equations. Eichinger et al., (1996) equated the Bowen ratio equivalent of Priestley Taylor equation with that of the Penman equation, by assuming sufficient upwind fetch and a uniform, saturated surface, as well as linearly approximating the slope of saturation vapor pressure. They derived that $PT_a = \frac{1+\frac{\gamma C}{\Delta+\gamma}}{1-\left(\frac{\gamma C}{\Delta+\gamma}\right)^2}$ where $C = \frac{e_a^* - e_a}{e_s^* - e_a}$ when the surface is saturated. '$*$' and ' ' represent the saturated and actual vapor pressure, and 'a' and 's' denote air and surface respectively. When a surface is not saturated, $C = \frac{(1-RH_a)e_a^* - (1-RH_s)e_s}{RH_s e_s^* - e_a}$.

A similar approach is proposed here, by equating the Penman-Monteith and Priestley Taylor equations. We derived that:

$$PT_a * \frac{\Delta}{\Delta+\gamma} * (R_n - G) = (\Delta * (R_n - G) + (\rho * C_p * \delta e / r_a))/(* (1 + r_c/r_a))$$

$$PT_a * \frac{\Delta}{\Delta+\gamma} * (R_n - G) = \frac{\Delta * (R_n - G)}{\Delta + \gamma * (1 + r_c/r_a)} + \frac{\frac{\rho * C_p * \delta e}{r_a}}{\Delta + \gamma * (1 + r_c/r_a)}$$

$$PT_a = (\frac{\Delta * (R_n - G)}{\Delta + \gamma * (1 + r_c/r_a)} + \frac{\frac{\rho * C_p * \delta e}{r_a}}{\Delta + \gamma * (1 + r_c/r_a)})/(\frac{\Delta}{\Delta+\gamma} * (R_n - G))$$

$$PT_a = \frac{\Delta * (R_n - G)}{\Delta + \gamma * (1 + r_c/r_a)} * (\frac{\Delta+\gamma}{\Delta(R_n - G))}) + \frac{\frac{\rho * C_p * \delta e}{r_a}}{\Delta + \gamma * (1 + r_c/r_a)} * (\frac{\Delta+\gamma}{\Delta(R_n - G))})$$

$$PT_a = \frac{\Delta+\gamma}{\Delta + \gamma * (1 + r_c/r_a)} + \frac{\Delta+\gamma \frac{\rho * C_p * \delta e}{r_a \Delta(R_n - G))}}{\Delta + \gamma * (1 + r_c/r_a)}$$

$$PT_a = \frac{\Delta + \gamma}{\Delta + \gamma * (1 + r_c/r_a)} * (1 + \frac{\rho * C_p * \delta e}{r_a \Delta (R_n - G))})$$

This Priestley Taylor coefficient formula has most likely been studied in the 1970s and 1980s.

A partial derivative of the presented Priestley Taylor coefficient equation was taken with respect to each key input of the equation. The partial derivatives were initially manually calculated and later verified with an online derivative calculator (Scherfgen, 2021).

$$\frac{d(PT_a)}{d(R_n - G)} = -\frac{(\Delta+\gamma)\rho C_p \delta e}{\Delta(R_n-G)^2((r_a+r_c)\gamma+\Delta r_a)}; \quad \frac{d(PT_a)}{d(r_a)} = \frac{(\Delta+\gamma)((r_c\Delta(R_n-G)-\rho C_p \delta e)\gamma-\Delta\rho C_p \delta e)}{\Delta(R_n-G)(r_a(\Delta+\gamma)+\gamma r_c)^2}$$

$$\frac{d(PT_a)}{d(r_c)} = -\frac{(\gamma+\Delta)(\rho C_p \delta e/(r_a\Delta(R_n-G))+1)\gamma}{r_a(\gamma(r_c/r_a+1)+\Delta)^2}; \qquad \frac{d(PT_a)}{d(\delta e)} = \frac{(\Delta+\gamma)(\rho C_p \delta e/(r_a\Delta(R_n-G))+1)}{(r_c/r_a+1)\gamma+\Delta}$$

A few behaviors of the Priestley Taylor coefficient can be observed. First, when $\delta e = 0$, changes in $R_n - G$ do not affect the coefficient. Second, given the four key inputs are positive, increasing in $R_n - G$and r_c and decreasing $r_a$and δewill decrease the coefficient. With respective to $R_n - G$, the decrease in the coefficient will is nearly negligible when $R_n - G$ is large.

Additional study is needed to better understand the sensitivity of the proposed equation of the Priestley Taylor coefficient. First, different typical scenarios should be defined, e.g. summer peak growing season and cloudy bare soil conditions, and tested with partial derivatives and evapotranspiration estimation. Next, $r_c$and r_a should be derived from field measurements and determine if the proposed model could effectively estimate measured evapotranspiration. Finally, a literature review is necessary to develop methods to estimate spatial $r_c$and r_a. Various existing wind speeds and vegetation indices products should be tested against field measurements.

References

Eichinger, W. E., Parlange, M. B., & Stricker, H. (1996). On the Concept of Equilibrium Evaporation and the Value of the Priestley-Taylor Coefficient. *Water Resources Research*, *32*(1), 161–164. https://doi.org/10.1029/95WR02920

Fisher, J. B., Tu, K. P., & Baldocchi, D. D. (2008). Global estimates of the land–atmosphere water flux based on monthly AVHRR and ISLSCP-II data, validated at 16 FLUXNET sites. *Remote Sensing of Environment*, *112*(3), 901–919. https://doi.org/10.1016/j.rse.2007.06.025

Jin, Y., Randerson, J. T., & Goulden, M. L. (2011). Continental-scale net radiation and evapotranspiration estimated using MODIS satellite observations. *Remote Sensing of Environment*, *115*(9), 2302–2319. https://doi.org/10.1016/j.rse.2011.04.031

Scherfgen, D. (2021). Derivative Calculator • With Steps! Retrieved February 23, 2021, from https://www.derivative-calculator.net/?fbclid=IwAR0HQWRXaAaI0grUnlYEE65gXKShUTrZAdHY8j646-1k1qd4iJuf7KHqA94

Appendix III: Influence of orchard age and salinity on almond evapotranspiration estimates during peak crop water demand.

This analysis presented here will be revised and included as a supporting document for publishing chapter 2.

It is commonly believed that salinity and orchard age were expected to influence crop evapotranspiration. However, the degree of influence of the two factors is uncertain. It is also unclear whether PT-UCD, a satellite data-driven, semi-empirical Priestley Taylor based model, could account for variability in evapotranspiration due to the two factors. In this study, we evaluated the relationship between evapotranspiration, and salinity, and orchard age, based on PT-UCD evapotranspiration estimates and ancillary data. If a relationship could be observed, how did remote sensing input data change, which in turn affects the estimates of the PT-UCD model? The analysis was conducted using clear-sky evapotranspiration estimates on Landsat overpassing days, during peak evapotranspiration month (July) of 2014 and 2016. The spatial estimates were compiled across all almond farms in the Central Valley. Then for each field (Figure 1), median evapotranspiration was extracted. The preprocessed data were then analyzed with salinity, orchard age, and model input and intermediate output data.

Based on spatial estimates from PT-UCD, we found that almond evapotranspiration generally increases as young orchard matures (Figure 2). After 9 years old, evapotranspiration stays around 5.5 mm per day. Older orchards (greater than 22 years old) appear to have a slightly lower evapotranspiration rate, but the difference was small and was not consistently observed

across the three Central Valley basins (Figure 3). Orchard age has the same effect on net radiation and Priestley Taylor coefficient estimates as on evapotranspiration (Figure 4).

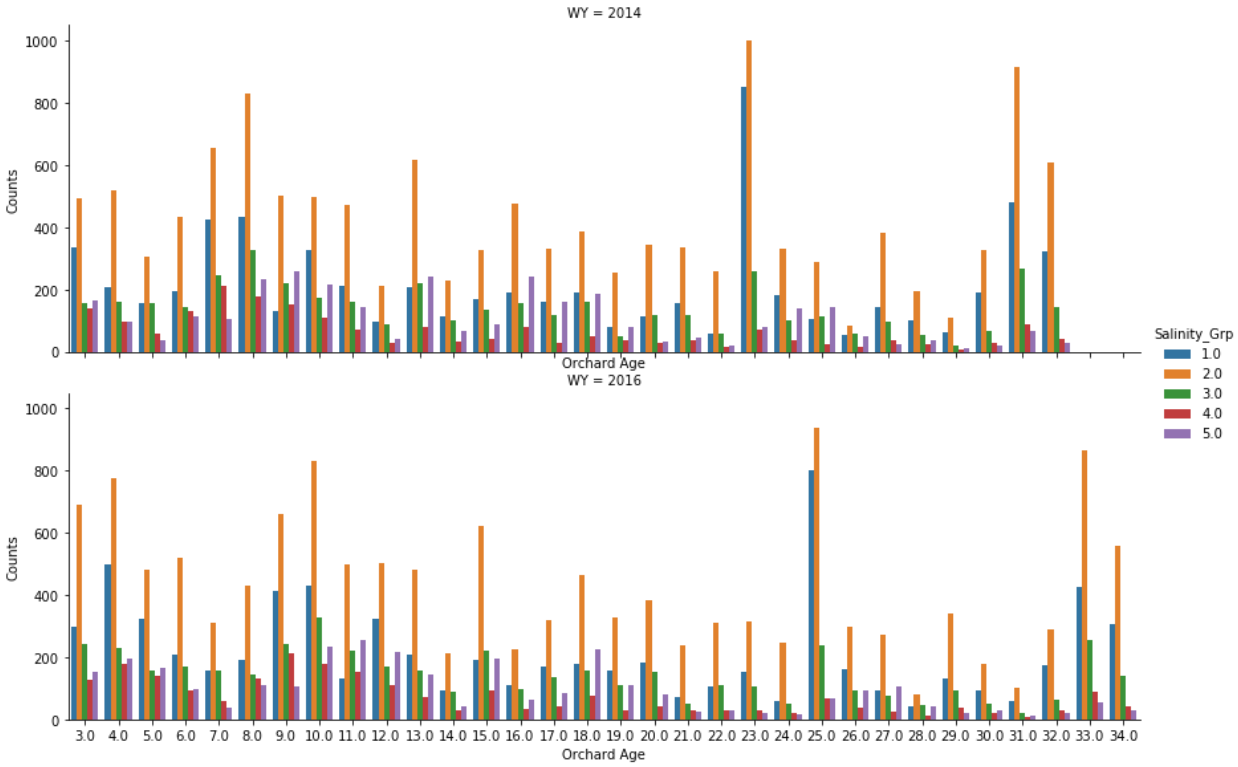

Figure 1. The number of almond fields evaluated in the Central Valley in July 2014 (Top) and 2016 (Bottom). The bar chart is colored by salinity level (group 1-5), where total dissolved solids (mg/L) at the production zone are between 1-250, 251-500, 501-750, 751-1000, >1000, respectively for group 1 through 5.

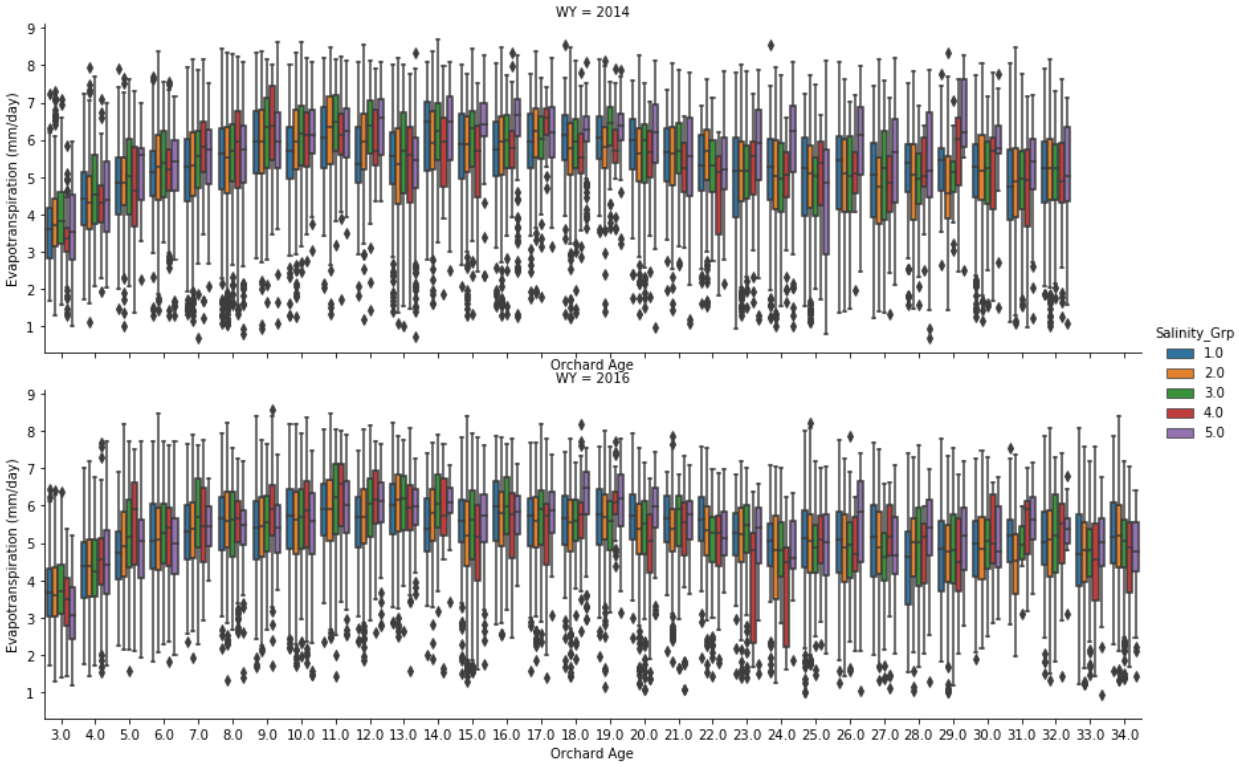

Figure 2. Boxplot of median evapotranspiration across all almond fields in the Central Valley in July 2014 (Top) and 2016 (Bottom). The bar chart is colored by salinity level (group 1-5), where total dissolved solids (mg/L) at the production zone are between 1-250, 251-500, 501-750, 751-1000, >1000, respectively for group 1 through 5. The box plot shows the quartiles of the dataset. The upper whisker is extended to the last datum less than the sum of the 1.5 times of interquartile range and the 3rd quartile. Similarly, the lower whisker is extended to the first datum greater than the first quartile subtracted by the 1.5 times of interquartile range.

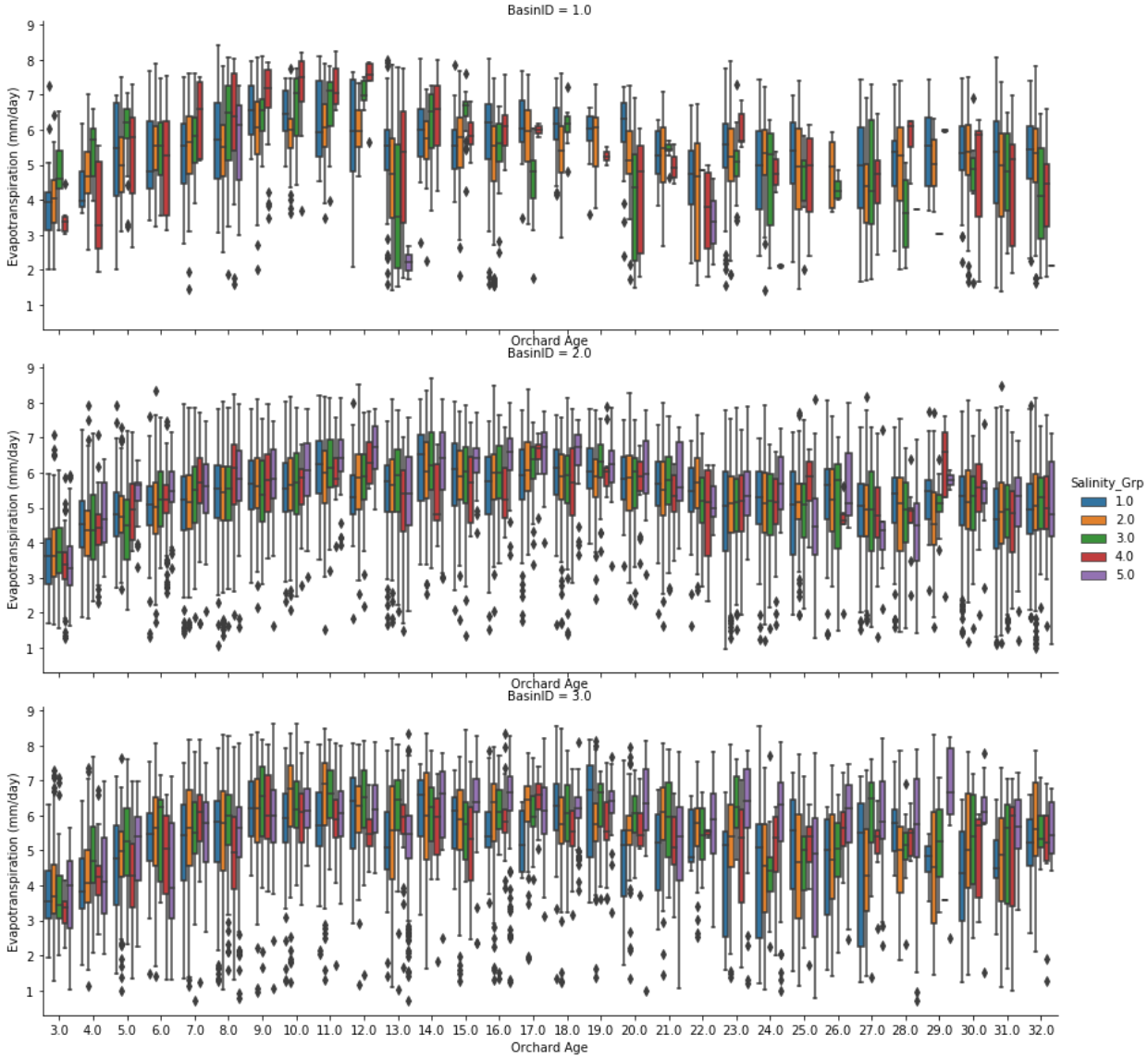

Figure 3. Boxplot of median evapotranspiration across all almond fields in three basins of the Central Valley in July 2014. The three basins are the San Joaquin River (BasinID=1), Sacramento River (BasinID=2), and Tulare Lake (BasinID=3). The bar chart is colored by salinity level (group 1-5), where total dissolved solids (mg/L) at the production zone are between 1-250, 251-500, 501-750, 751-1000, >1000, respectively for group 1 through 5. The box plot shows the quartiles of the dataset. The upper whisker is extended to the last datum less than the sum of the 1.5 times of interquartile range and the

3rd quartile. Similarly, the lower whisker is extended to the first datum greater than the first quartile subtracted by the 1.5 times of interquartile range.

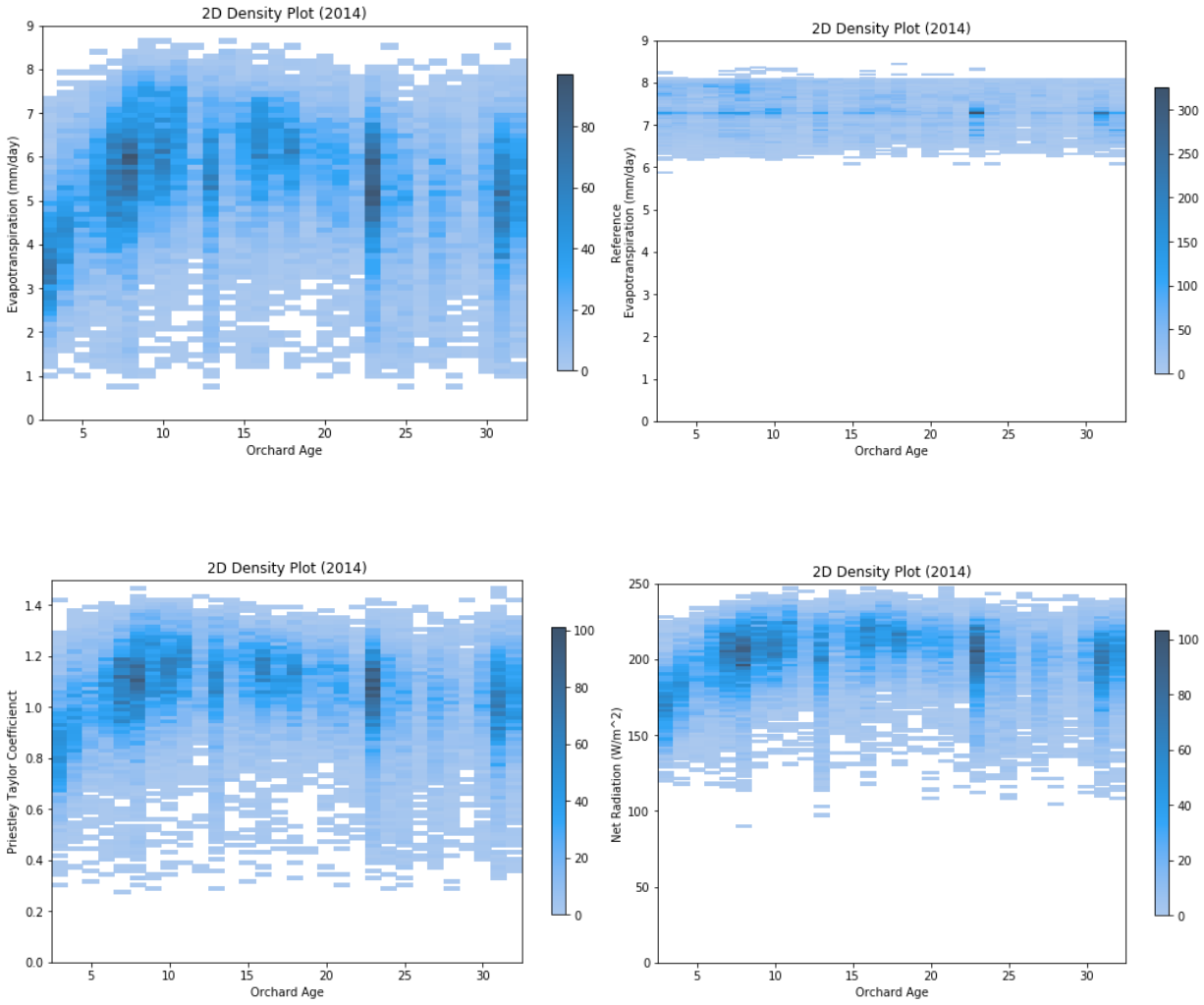

Figure 4. Density Plot of orchard age vs. a median of model estimates across all almond fields in the Central Valley in July 2014. The estimates are evapotranspiration (top, left), reference evapotranspiration (top, right), Priestley Taylor coefficient (bottom, left), and net radiation (bottom, right). The color bar indicates the number of orchard fields, given age and range of estimates.

Further examination on relationships between orchard age and remote sensing data helped identify several possible pathways, of which orchard age may affect biophysical properties, which is observed indirectly via satellite and ultimately affecting the estimation. In all visible wavelengths (red, green, and blue), surface reflectance was found to decrease as young orchards mature. This aligns with the common knowledge that the fraction of vegetation to the total land area increases as the orchard matures. While plants absorb electromagnetic radiation in the visible wavelengths to fuel photosynthesis, the soil has higher surface reflectance than plants in the visible wavelength. Therefore, the surface reflectance of immature orchards is typically higher than mature orchards. To our surprise, the surface reflectance in the near-infrared band appears constant across age classes. It differs from our initial expectation because reflectance in the near-infrared band typically increases with the fraction of vegetation to total land area. Surface reflectance in the shortwave reflectance and land surface temperature follow a similar pattern to visible wavelengths. Reflectance in the shortwave infrared band is negatively correlated with moisture availability in plant leaves and on land surfaces, suggesting that younger orchards in combination with surrounding open soils have less moisture than mature orchards. On the other hand, transpiration during photosynthesis helped to cool the leaf surface. This explains why younger orchards, with a lower fractional cover of vegetation, tend to have a higher land surface temperature. The response of surface reflectance and temperature to orchard age at 30m pixel resolution, influences the computation of albedo, outgoing longwave radiation, NDVI, and NDMI, which affects the estimation of net radiation and Priestley Taylor coefficient, and ultimately almond evapotranspiration. In summary, we observed that as young orchard matures, albedo, NDVI, and NDMI increase and outgoing longwave radiation decreases. This in

turn increases available energy to the plant (Net Radiation) and increases partitioning of energy to evapotranspiration (Priestley Taylor coefficient).

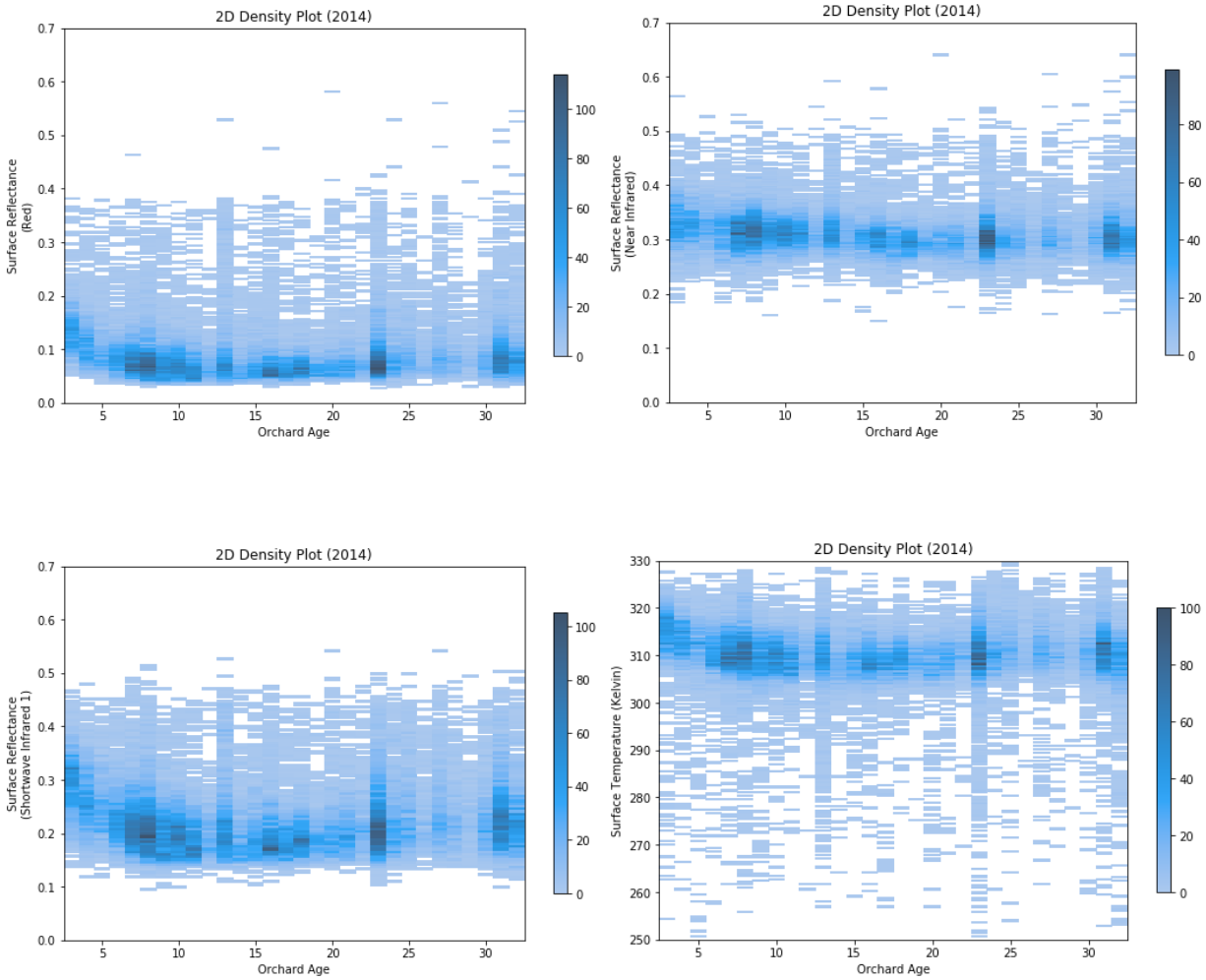

Figure 5. Density Plot of orchard age vs. median values of selected remote sensing input across all almond fields in the Central Valley in July 2014. The selected inputs are surface reflectance in the red band (top, left), surface reflectance in the near-infrared band (top, right), surface reflectance in the shortwave infrared band 1 (bottom, left), and land surface temperature (bottom, right). The color bar indicates the number of orchard fields, given age and range of estimates.

Contrary to expectations, we did not observe a consistent difference in evapotranspiration orchards at different age groups and salinity levels (Figure 2). The remote sensing input data, e.g. land surface reflectance and temperature, were not significantly different among the four salinity levels (Figure 6, 7). A possible explanation is that the salinity map used in this study does not reflect the actual soil condition on the ground. The salinity map in this study was developed with a groundwater model, and it estimates the salinity of groundwater at the production zone (Luhdorff and Scalmanini Consulting Engineers, 2016). While the map may be correct regarding the salinity of water in the aquifer, it might not reflect the salinity of the soil moisture in the root zone. As an alternative salinity map covering the Central Valley is not available, a compilation of field-measured salinity records will be needed to further investigate the relationship between salinity and evapotranspiration.

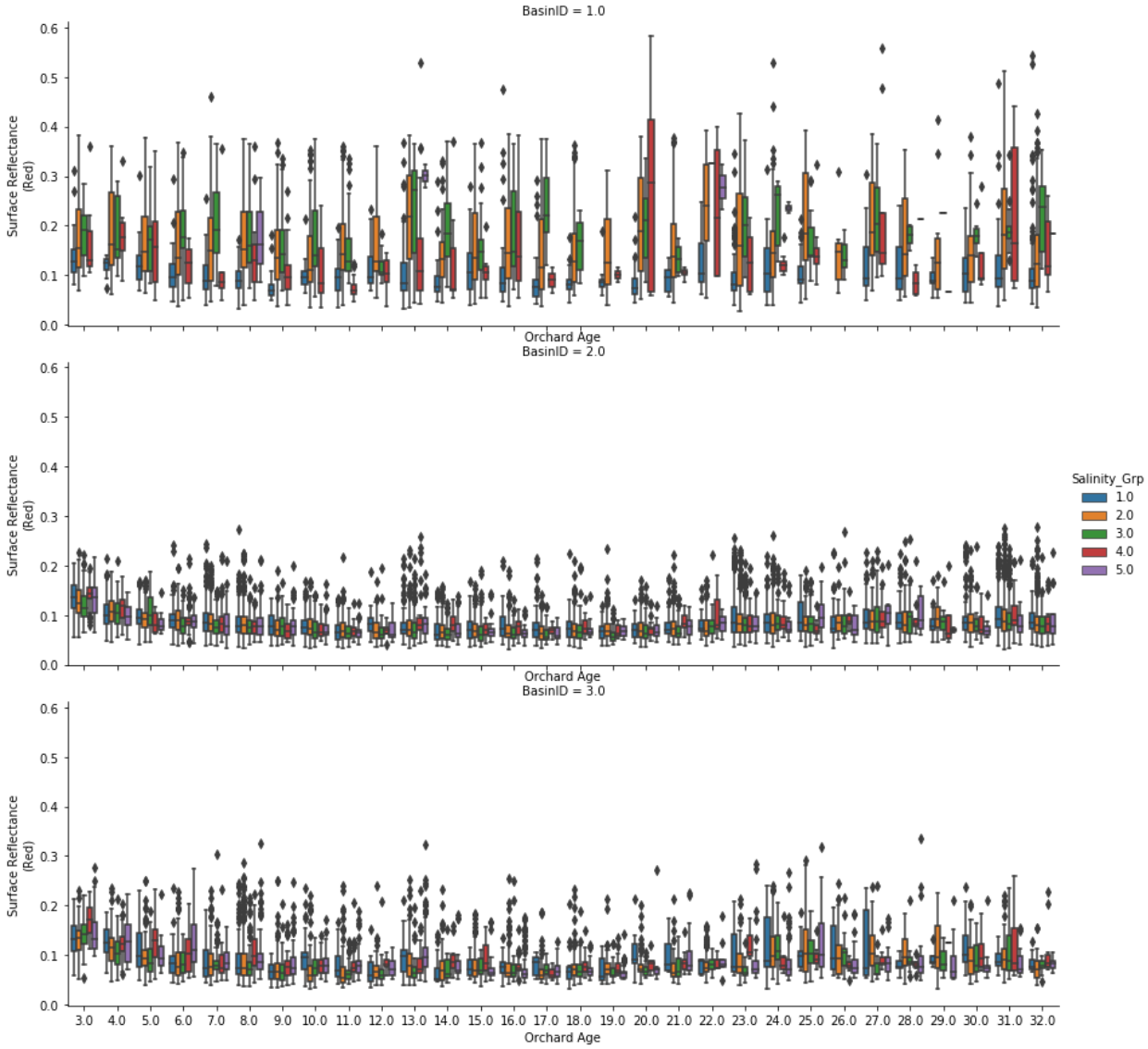

Figure 6. Boxplot of median surface reflectance in the red band across all almond fields in three basins of the Central Valley in July 2014. The three basins are the San Joaquin River (BasinID=1), Sacramento River (BasinID=2), and Tulare Lake (BasinID=3). The bar chart is colored by salinity level (group 1-5), where total dissolved solids (mg/L) at the production zone are between 1-250, 251-500, 501-750, 751-1000, >1000, respectively for group 1 through 5. The box plot shows the quartiles of the dataset. The upper whisker is extended to the last datum less than the sum of the 1.5 times of interquartile range and

the 3rd quartile. Similarly, the lower whisker is extended to the first datum greater than the first quartile subtracted by the 1.5 times of interquartile range.

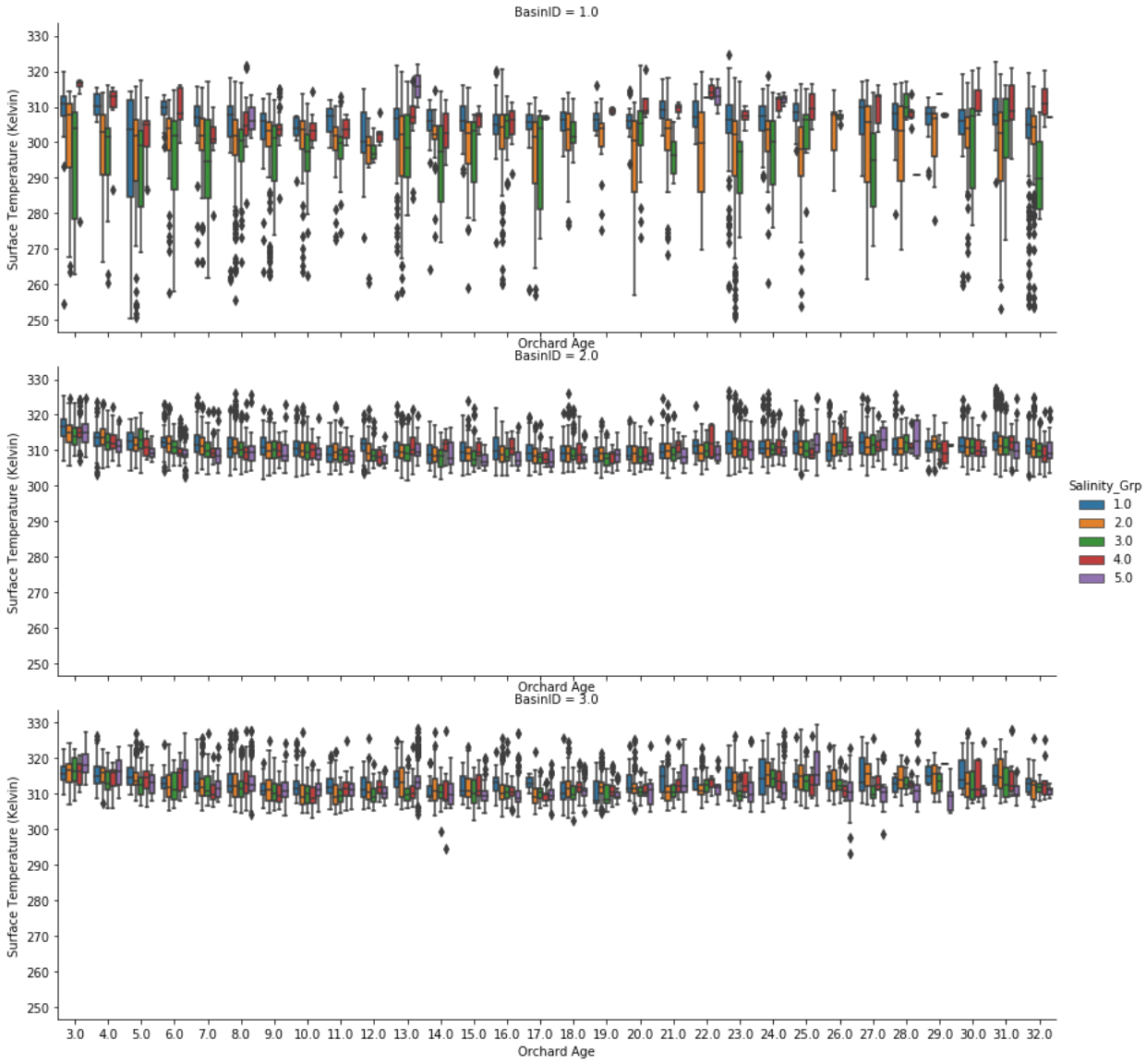

Figure 7. Boxplot of median land surface temperature across all almond fields in three basins of the Central Valley in July 2014. The three basins are the San Joaquin River

(BasinID=1), Sacramento River (BasinID=2), and Tulare Lake (BasinID=3). The bar chart is colored by salinity level (group 1-5), where total dissolved solids (mg/L) at the production zone are between 1-250, 251-500, 501-750, 751-1000, >1000, respectively for group 1 through 5. The box plot shows the quartiles of the dataset. The upper whisker is extended to the last datum less than the sum of the 1.5 times of interquartile range and the 3rd quartile. Similarly, the lower whisker is extended to the first datum greater than the first quartile subtracted by the 1.5 times of interquartile range.

References

Luhdorff and Scalmanini Consulting Engineers. (2016). *Region 5: Updated Groundwater Quality Analysis and High Resolution Mapping for Central Valley Salt and Nitrate Management Plan*. Central Valley Salinity Alternatives For Long Term Sustainability. Retrieved from https://www.cvsalinity.org/docs/committee-document/technical-advisory-docs/conceptual-model-development/3306-updated-groundwater-quality-analysis-and-high-resolution-mapping-for-central-valley-salt-and-nitrate-management-plan/file.html

Appendix IV: Supporting Materials of Chapter III

Text S1.

Of the four major crop classes in the Pajaro Valley, a total of 102 data entries were recorded. Among the available survey entries, four records in 2011 were removed in this study, because the pump IDs were missing in three entries and one entry was accidentally duplicated from another. In addition, three entries were amended, because, in two entries, typos were found, and in one entry, the documented well was discounted after 2009, and the well's replacement was identified. The changes made to the survey data for this study were reviewed and approved by the principal investigator of the survey team.

Text S2.

Root depth for different crop types was identical to PVHM's (Hanson et al., 2014), as shown below: Strawberries, Artichokes, and Nurseries (91.4cm), Vegetables (46.0cm), Raspberries (191.1cm), Vinegrapes (152.1cm), Deciduous (Apples) (182.9cm), and Others (60.96cm).

Text S3.

Soil property maps used in the soil water balance include the mean of saturated hydraulic conductivity, bulk density, hydrologic group, water holding capacity (0-50cm soil depth), and % clay and % sand by weight (0-25 cm and 25-50cm). From soil property data, total porosity (θ_T) and field capacity (θ_f) are computed as follows,

$\theta_T = 1 - \frac{Bulk\ Density}{2.65\frac{g}{cm^3}}$ and $\theta_f = \frac{Total\ Water\ Holding\ Capacity_{@\ 50\ cm}}{50cm}$.

Text S4.

The approximation of λ is identical to that in Soil Data Builder, an IWFM's support tool (California Department of Water Resources, 2020), where $\lambda = e^P$ and $P = -0.7842831 + 0.0177544S - 1.062498\theta_T$

$$-0.00005304S^2 - 0.00273493C^2 + 1.111340{46\theta_T}^2$$

$$-0.03088295S\theta_T + 0.00026587S^2{\theta_T}^2 - 0.00610522C^2{\theta_T}^2$$

$$-0.00000235S^2C + 0.00798746C^2\theta_T - 0.006744{91\theta_T}^2C. \quad (7)$$

In equation 7, S and C are the percentages of sand and clay, respectively. To calculate the percentage of sand and clay in the 50cm soil column, an average was taken between the soil property rasters at 0-25 cm and 25-50cm.

Text S5.

The estimation of the parameter, S, in computing runoff from precipitation, is modified for a non-iterative solution and is determined by intermediate soil moisture (${\theta_{int}}^t$), where ${\theta_{int}}^t = \frac{(\theta^{t-1}z - P_c^t)}{z}$. When ${\theta_{int}}^t \leq \frac{\theta_f}{2}$, $S = S_{max}$, such that $S_{max} = \frac{1000}{CN} - 10$; When ${\theta_{int}}^t > \frac{\theta_f}{2}$, $S = \{S_{max}(1 - \frac{{\theta_{int}}^t - \frac{\theta_f}{2}}{\theta_T - \frac{\theta_f}{2}})$. The curve number (CN) is assigned according to hydrologic groups classification, as follows: Group A (64), Group B (75), Group C (82), Group D (85). Areas where the hydrologic group classification was uncertain, including groups A/D, B/D, and C/D, were all assigned as class D.

Table S1. Summary table of derived application efficiency. The symbol '--' indicates that application efficiency was not derived, and the uncalibrated value from Garza-Díaz et al., 2019 was used in computing regional applied water.

Variant	Year	Strawberries	Vegetables	Raspberries	Vinegrapes
Derived Value (Median)	2009 & 2011	0.490	0.545	0.350	--
Derived Value (25th - 75th Percentile)	2009 & 2011	0.390 - 0.650	0.345 - 0.793	0.240 - 0.470	--
Garza-Díaz et al., 2019	2009	0.805	0.805	0.805	0.851
	2011	0.811	0.811	0.811	0.852
Hanson et al., 2014	2009	0.42 - 0.96	0.32 - 0.96	0.85	0.88

Variant	Year	Artichokes	Deciduous (Apple)	Nurseries	Others
Derived Value (Median)	2009 & 2011	--	0.99	--	--
Derived Value (25th - 75th Percentile)	2009 & 2011	--	0.99 - 0.99	--	--
Garza-Díaz et al., 2019	2009	0.805	0.822	0.805	0.805
	2011	0.811	0.825	0.811	0.811
Hanson et al., 2014	2009	0.57 - 0.83	0.80-0.95	0.73 -0.83	0.64 - 0.85

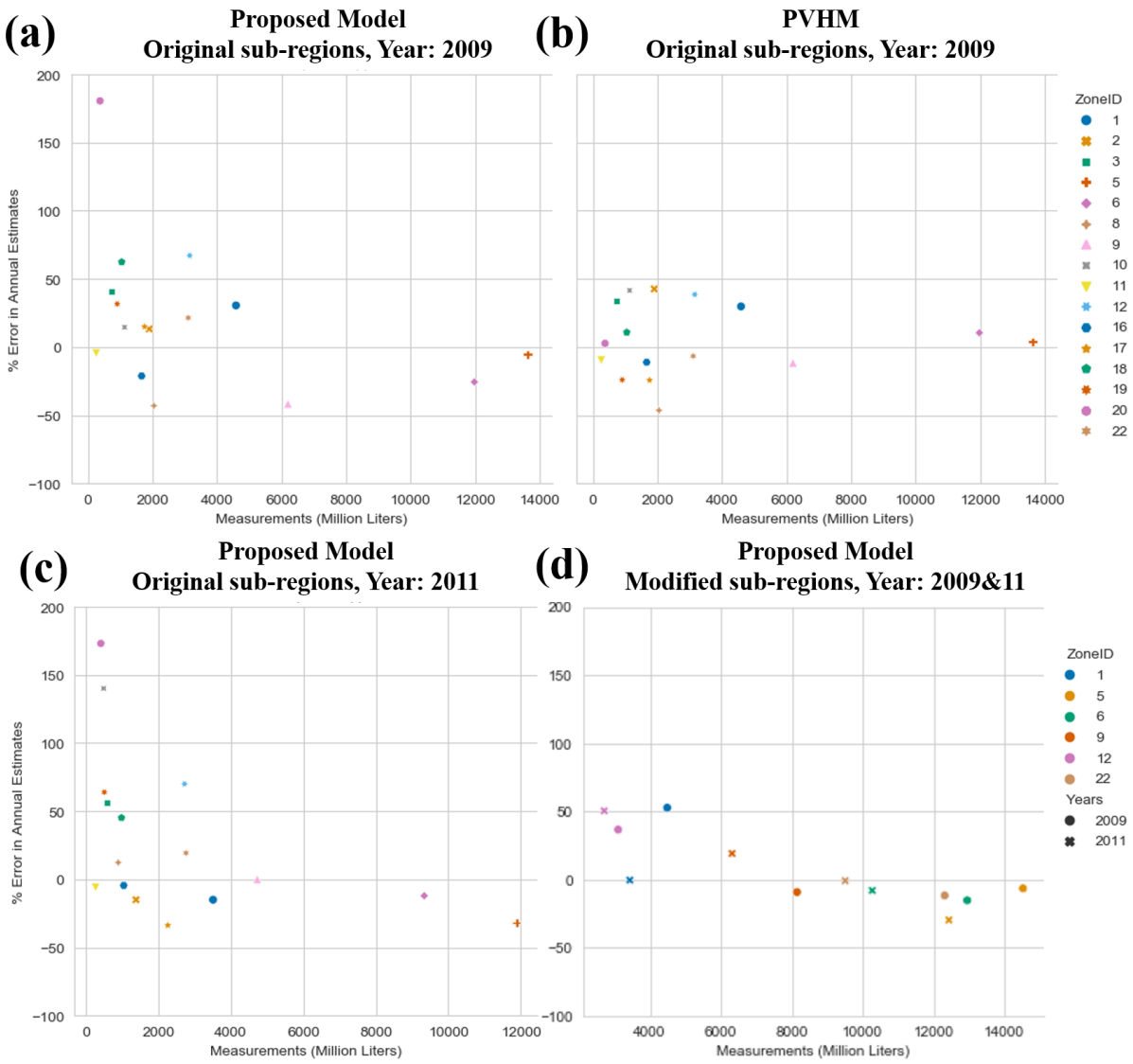

Figure S1. Percent error in annual sub-regional agricultural applied water estimates. Results are based on PVHM's zone boundaries (a, b, c) and the modified zone boundaries (d). While the estimates from the proposed model are shown on (a, c, and d), PVHM's estimates are shown on (b).

Appendix V: Comparing evapotranspiration estimates between PVHM and PT-UCD0

The research presented here will be continued when an update on PVHM is published. The updated PVHM will enable the export of gridded evapotranspiration estimates, which allow us to compare evapotranspiration estimates only on agricultural cells.

The Pajaro Valley of California is one of the most productive agricultural regions in the world, and managing its groundwater resources is becoming increasingly challenging as a result of population growth, agricultural development, climate variability, and seawater intrusion. In 2014, the Pajaro Valley Hydrological Model (PVHM) was developed to produce accurate groundwater simulation results at scales relevant to water management decisions that were being considered in the revision and updates to the Basin Management Plan. Major components (evapotranspiration, applied water, runoff, and percolation) water budget of PVHM were considered reliable because the model parameters have been calibrated with the best available pumping, groundwater level, and river flow observations. We attempted to test this assumption by comparing the PVHM's evapotranspiration estimates with that of remote sensing estimates. On one hand, a significant discrepancy opens up opportunities for further investigation. On the other hand, similar evapotranspiration may suggest that PVHM, although requires a significant amount of data and sophisticated calibration, was successful in accurately modeling the water budget. When comparing the sub-regional evapotranspiration average from PVHM's estimates against the remote sensing estimates, a significant discrepancy was found (R^2 = 0.90, RMSE = 13560 million liters). However, when remote sensing estimates were adjusted with a soil water balance over non-irrigated pixels, a significantly better agreement was found (R^2 = 0.99, RMSE = 1347 million liters). The discrepancy was investigated, and several potential issues and limitations were identified. The current results were inconclusive, but they provide an invaluable

foundation and guidance for research in the near future when USGS publishes the latest, updated PVHM.

The original remote sensing evapotranspiration was generated from 2004 to 2009 and was spatially aggregated by PVHM's WBS zone boundaries and temporally aggregated to monthly, quarterly, and annual time scales (Figures 1-3). For all time scales, remote sensing estimates are found to be significantly higher than PVHM's estimates.

The disagreement of total evapotranspiration appears to coincide with lack of rainfall (Figure 4). From figure 3, an increase of the slope of best fit could be observed, starting from 0.7 in January to the peak of 5.2 in September after several consecutive months of no precipitation. In October, remote sensing estimates in most zones and years remained significantly higher than PVHM's estimates, with an exception where the zones experienced precipitation around 4 mm day^{-1}.

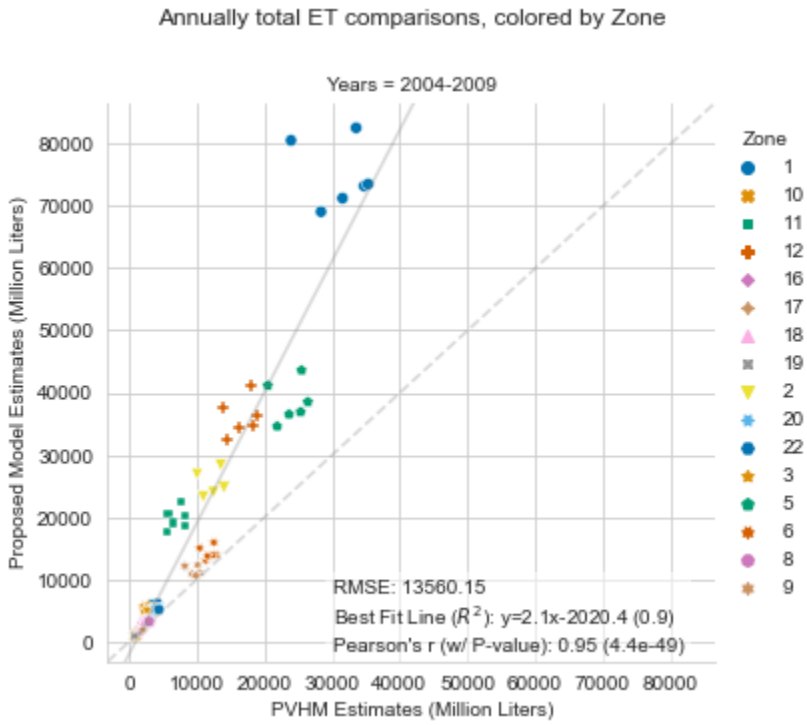

Figure 1. Comparison of zonal and annual sum evapotranspiration estimates.

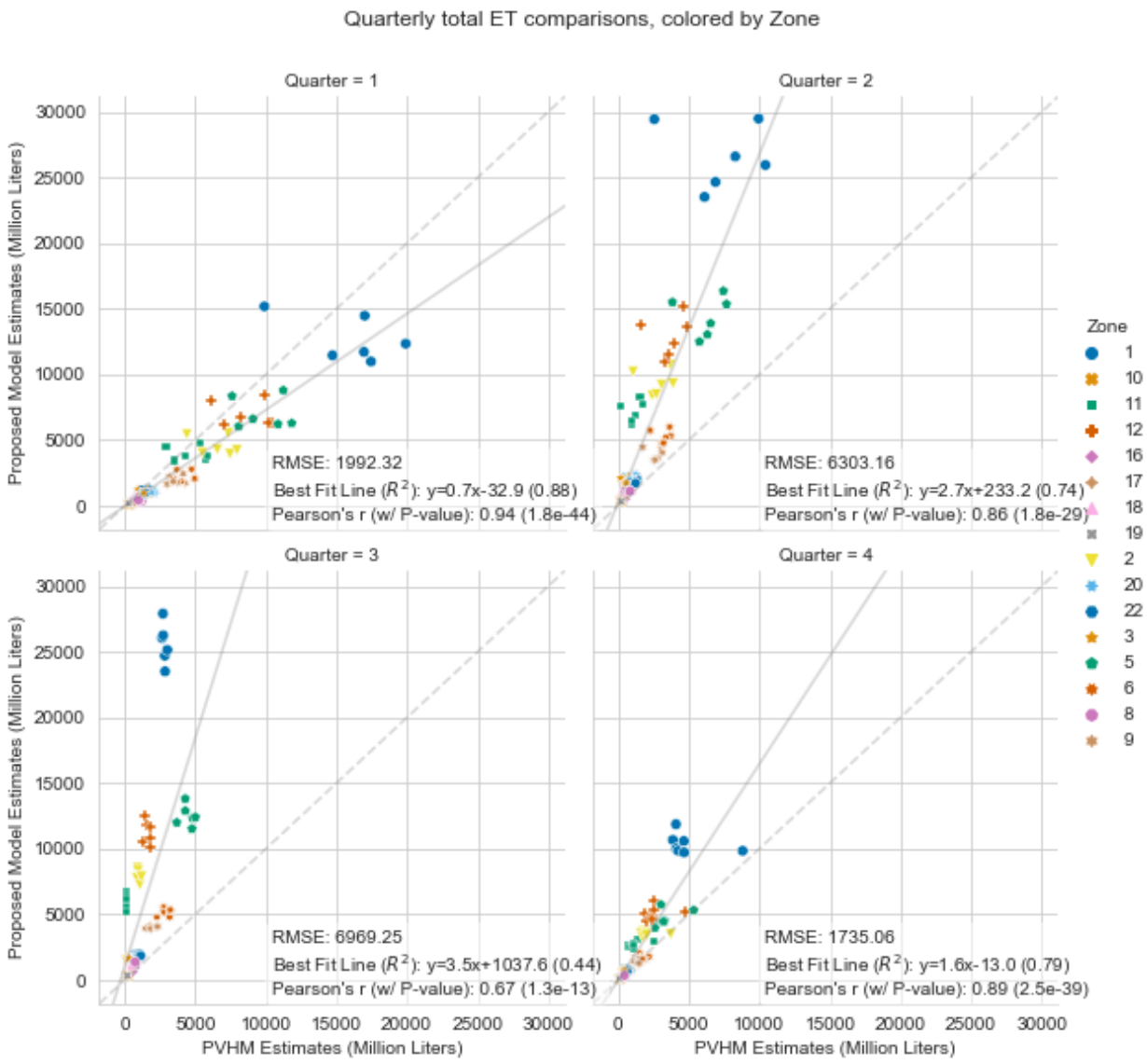

Figure 2. Comparison of zonal and quarterly sum evapotranspiration estimates.

Figure 3. Comparison of zonal and monthly sum evapotranspiration estimates.

Figure 4. Comparison of zonal and monthly sum evapotranspiration estimates. Symbols are colored by monthly spatial averaged precipitation from the NASA Daymet 1km dataset.

Besides precipitation, the discrepancy of evapotranspiration between the two models may be related to the percentage of irrigated area in each zone (Figure 5). For example, zones 10 and

2 are adjacent to each other, but 60.7% of area zone 10 in 2009 were irrigated crops while zone 2 only has 17.5%. Comparing the time series of the two zones (Figure 6), we found that estimates between the two models were more agreeable at zone 10 than at zone 2. Besides, we observed that the pattern of PVHM's evapotranspiration estimate did not conform to our expectations for crops (Figure 6). We did not expect evapotranspiration to be low during the peak summer growing season. The February and March evapotranspiration is also higher than expected.

Several possible explanations for the evapotranspiration discrepancies were identified. First, remote sensing evapotranspiration estimates have not been evaluated in natural landscapes. The remote sensing approach likely overestimated evapotranspiration over the natural landscape. Therefore, we expected a zonal average of evapotranspiration to behave similarly to our estimates at zone 10, where the summer evapotranspiration is much lower than the expected value for the crop (6+ mm/day) due to averaging of evapotranspiration between dried up natural vegetation and irrigated crops. The remote sensing techniques are also limited by data availability. The revisit frequency of a Landsat satellite is once every 16 days, but fortunately, the Landsat satellites (5, 7, 8) have long overlapping operation periods, such that a satellite image is generally available every 8 days. Weather conditions also affect the accuracy of evapotranspiration estimates. When a satellite image is obscured by clouds, it could not be used to estimate evapotranspiration, introducing uncertainty in monthly estimates when estimates on clear-sky satellite overpassing dates were interpolated. The coastal region of the Pajaro Valley is also prone to mists that some persist till noon. The quality assurance product may sometimes fail to identify mist, causing errors in the land surface reflectance and temperature products, which are key inputs of the remote sensing evapotranspiration estimation model.

Figure 5. Comparison of zonal and annual sum evapotranspiration estimates. Symbols are colored by percent irrigated agriculture in 2009 calculated from PVHM's land use map.

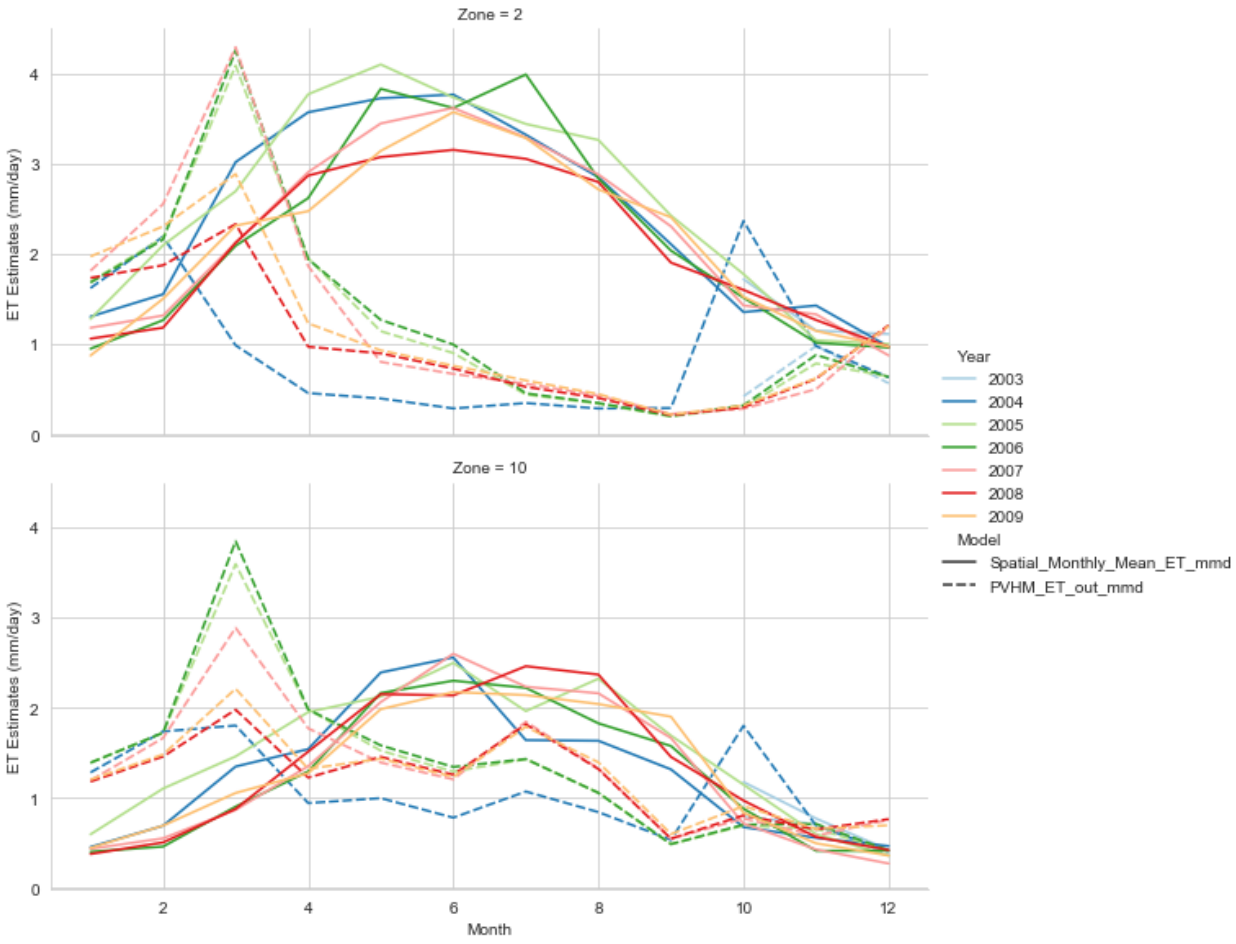

Figure 6. Comparison of monthly averaged evapotranspiration estimates for agriculture-dominated zone 2 and nature-landscape-dominated zone 10. Lines colored by year, and solid and dash lines represent remote sensing and PVHM's estimates, respectively.

Besides the uncertainty of remote sensing estimates, PVHM's estimate may also be problematic, due to its inability to capture the spatial and temporal variation of evapotranspiration for identical land use. First, the crop coefficient-based estimates could not capture field to field variation in evapotranspiration that is caused by management practice. For example, year-to-year variability in weather may affect the plantation and harvest time of crops by up to several weeks. Similarly, rapid water stress and the effect of irrigation practices on a

field's evapotranspiration are also not captured by crop coefficient based estimates. Second, PVHM attempted to address the year-to-year variability of evapotranspiration by adding a calibrated scale factor that differs between wet and dry years. Further evaluation of the calibrated values is needed. It is unclear how the wet and dry years are defined and whether the scaling factor, in combination with reference evapotranspiration, is sufficient to explain interannual variability. At last, PVHM's evapotranspiration estimates are subject to human error, which could introduce uncertainties in optimized parameters. We found that the reference evapotranspiration file for 2005 was repeatedly used for 2006. A similar mistake was also identified in precipitation, where the 2005 data were used from 2005 through 2009.

After remote sensing estimates over non-agricultural pixels are adjusted in a soil water balance, we found a significant improvement in agreement between PVHM and remote sensing estimates, with an RMSE in 2009 decreasing from 24 trillion to 1.3 billion liters or from 1026 mm day^{-1} to 0.2 mm day^{-1}. An improvement in the agreement was also found in time series comparison (Figure 8).

The results of the evapotranspiration estimates comparison are not conclusive, as additional data and analysis are needed. Currently, adjusted evapotranspiration is only available for 2009, because the water balance model in Chapter 3 has not been implemented for other years. The comparison should also be conducted over only agricultural cells, but the current PVHM model does not support the export of water fluxes in a grid format. As an update on PVHM will soon be released by USGS, we expect a more fruitful comparison is possible in near future.

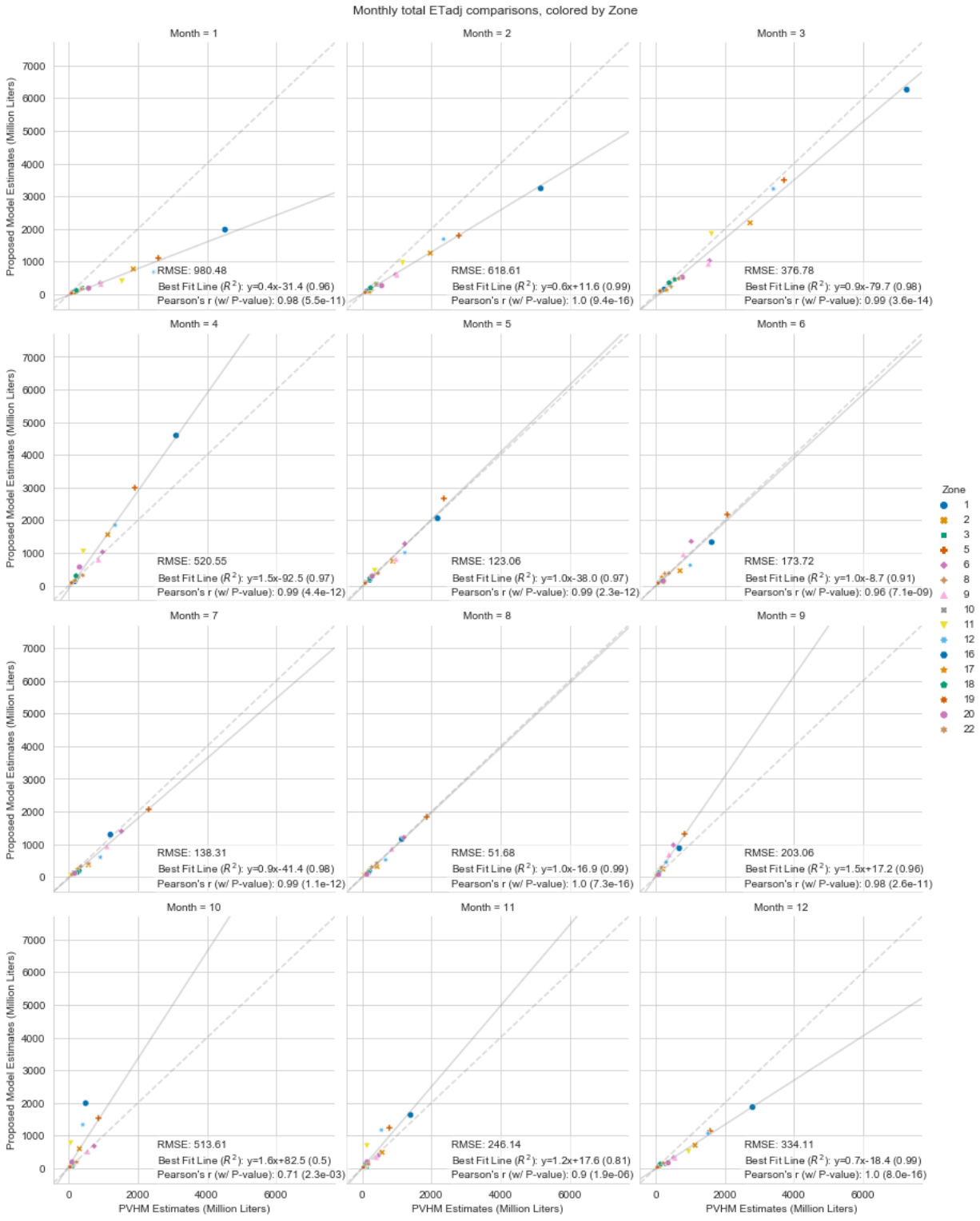

Figure 7. Comparison of zonal and monthly sum evapotranspiration estimates, where remote sensing estimates over the natural landscape are adjusted.

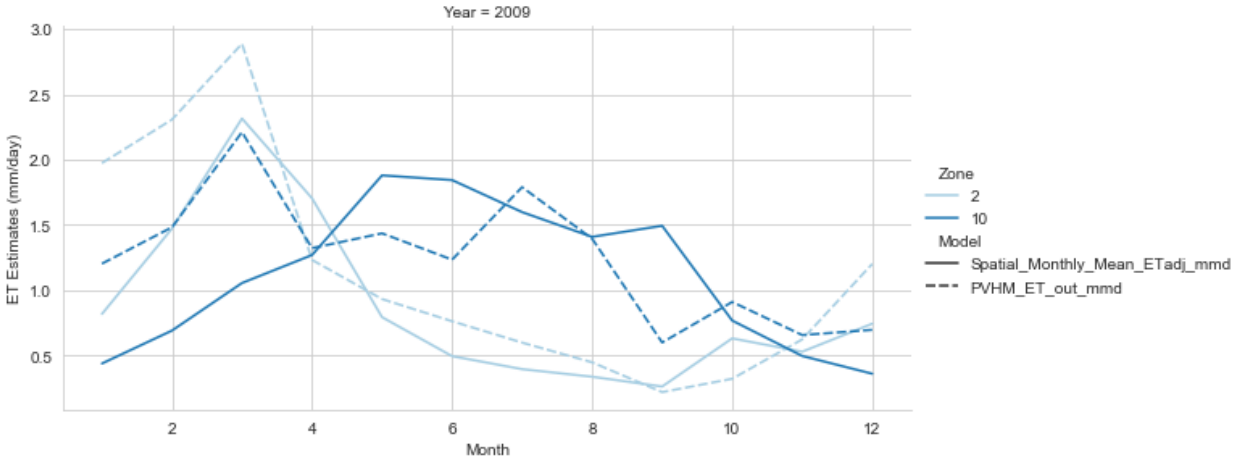

Figure 8. Comparison of monthly averaged evapotranspiration estimates for agriculture-dominated zone 2 and nature-landscape-dominated zone 10. Remote sensing estimates over natural landscapes are adjusted. Lines colored by year, and solid and dash lines represent remote sensing and PVHM's estimates, respectively.